Field Theoretical Approach to the Phases of QCD

A Dissertation Presented to

the Faculty of the Department of Physics

UNIVERSITY OF HOUSTON

In Partial fulfillment

of the requirements for the degree of

Doctor of Philosophy

By

Israel Portillo Vázquez

May, 2019

Field Theoretical Approach to the Phases of QCD

Israel Portillo Vázquez

APPROVED:

Dr. Claudia Ratti, Chairman

Dr. Rene Bellwied, Co-Chairman

Dr. Carlos Ordóñez

Dr. Ricardo Vilalta,
Department of Computer Science

Dr. Dan E. Wells, Dean
College of Natural Sciences and Mathematics

Field Theoretical Approach to the Phases of QCD

An Abstract of a Dissertation Presented to

the Faculty of the Department of Physics

UNIVERSITY OF HOUSTON

In Partial fulfillment

of the requirements for the degree of

Doctor of Philosophy

By

Israel Portillo Vázquez

May, 2019

Abstract

The study of the phases of Quantum Chromodynamics (QCD), at finite temperature (T) and baryon chemical potential (μ_B), is one of the biggest challenges in theoretical physics and represents a significant step towards understanding the collective behavior of the strong force. The non-perturbative region of QCD, where atomic matter dissolves into a Quark-Gluon-Plasma state, can only be studied from first principles by numerical lattice simulations. These studies have established that the transition is a smooth crossover. It is expected that, as μ_B increases, the crossover sharpens into a critical-end-point (CEP) where a first order phase transition begins. However, due to the fermion sign problem, calculations on the lattice cannot be performed at real μ_B. On the experimental side, efforts are being made at heavy-ion colliders (HICs) to probe high regions of μ_B in search for the CEP. To support these efforts, alternative theoretical frameworks are required to relate those experiments to the phases of QCD.

This dissertation is devoted to exploring the high μ_B-region of QCD. First, I will analyze the lower order baryonic susceptibilities simulated on the lattice at imaginary-μ_B to calculate the higher order ones at $\mu_B = 0$. Those susceptibilities allow one to have access to a finite μ_B, by Taylor expanding the QCD thermodynamical potential around $\mu_B = 0$, and to make a direct connection with the distribution of conserved charges measured in HICs. The second part of this thesis uses a model based on the gauge/string duality to engineer holographic black holes that mimic the equation of state of QCD obtained on the lattice at $\mu_B = 0$ and predicts its behavior at finite μ_B. Our black hole model provides a realistic prediction of the existence of a CEP in the phase diagram of QCD, located at $\mu_B^{\text{CEP}} = 724$ MeV and $T_{\text{CEP}} = 89$ MeV. It reproduces the baryon susceptibilities calculated on the lattice at $\mu_B = 0$ and predicts them at arbitrary μ_B. Finally, the

analysis made with the holographic model leads to predict the collision energy needed to hit the CEP in HICs, which is within the range of the next generation of colliders.

Contents

Chapter 1

Introduction to the Phases of QCD

1.1 Introduction

Over the last century, the interplay between experiments and theoretical models has brought about a radically new understanding of the constituents of matter and their interactions. The fundamental particles that make up all matter in the universe are quarks and leptons, and their interactions are governed by the principle of local gauge invariance. These ideas are summarized in the Standard Model of Particles, whose essential components are the Electroweak Theory, which unifies Quantum Electrodynamics (QED) with the weak nuclear force, and the theory of strong interactions, Quantum Chromodynamics (QCD) [1].

QCD governs the quark sector of the Standard Model. Its interaction is defined by the non-Abelian SU(3) gauge group with gluons as the mediators of the force. Consequently, the fundamental degrees of freedom of QCD are the quarks and the gluons, which posses three color charges. The strength of the strong force under ordinary circumstances is large. However, as with other non-abelian theories, QCD exhibits an

effective interaction strength that decreases at short distances, or high energies, leading to interesting phenomena such as asymptotic freedom and color superconductivity, and confinement and dynamical chiral symmetry breaking at low energies. These features are expected to generate complex subatomic structures and phases commonly sketched on the "QCD phase diagram". The aim of the QCD phase diagram is mapping out the state of strongly interacting matter as a function of two relevant thermodynamic variables: the temperature (T) and the baryonic chemical potential (μ_B).

The study of the QCD phase diagram is a topic of great interest and active investigation both in experiment and in theory, and it covers a wide range of disciplines from cosmology and astrophysics, to nuclear and particle physics. Due to the dependence of the coupling constant on the energy scale, there are two prominent phases of strongly interacting matter. Under ordinary conditions, quarks and gluons are confined into color-neutral hadrons, such as protons and neutrons that make up the nuclei of the atoms. At densities about a trillion times larger than ordinary nuclear matter, hadrons give way to a deconfined phase of quarks and gluons known as the quark gluon plasma (QGP).

In nature, the hot QGP filled the early universe just a few microseconds after the Big Bang and gave rise to the primordial baryonic matter. At present, compact stars are expected to contain cold and baryon rich quark matter, which makes them the natural candidate to contain deconfined quark matter. Nowadays, the extreme conditions needed to create the QGP can be recreated in the laboratory in heavy ion colliders (HIC) such as the Relativistic-Heavy-Ion Collider (RHIC) at Brookhaven National Laboratory (BNL), and Large Hadron Collider (LHC) at the European Organization for Nuclear Research (CERN).

There are several theoretical tools to study strongly interacting matter. Theoretical

frameworks are required to relate observables measured in HICs, or any astrophysical observation, to the properties of the QGP and to the QCD phase diagram. At high energies, where the QCD coupling is small, perturbation theory describes the asymptotic behavior of the QGP with weakly interacting quarks and gluons as degrees of freedom [2, 3]. In the non-perturbative region of QCD, at finite T and zero μ_B, the equilibrium properties of strongly interacting matter can only be obtained by means of lattice simulations. Those calculations have established that the transition from hadronic matter to the QPG is a smooth crossover, taking place over a $20 - 30\,\mathrm{MeV}$ range of temperatures, centered around $T_c \simeq 155\,\mathrm{MeV}$. [4–9]. While lattice QCD is unable to perform full calculations at finite real μ_B due to the fermion sign problem, a small finite region of μ_B can be reached employing different techniques. One of them is to Taylor expand the thermodynamical observables calculated on the lattice at zero μ_B [10–14]. Another possibility is to calculate those observables at imaginary-μ_B and perform an analytical continuation to the real plane [15–19]. At present, the first three terms of the Taylor expansion of the equation of state (EoS) from the lattice are known. They allow one to extrapolate the QCD thermodynamic potential up to $\mu_B/T \leq 2$ [20, 21]. In this region of the QCD phase diagram, the crossover extends with a negative curvature. It is believed that, with increasing μ_B, this crossover sharpens and terminates in a critical end point (CEP) where a first order phase transition begins. The question of both the existence and location of the CEP is fundamental to understand QCD matter, but it is hard to determine theoretically due to the non-perturbative nature of QCD in the vicinity of the phase transition.

The CEP is characterized by the divergence of the baryonic susceptibilities. The susceptibilities of conserved charges are proportional to the corresponding Taylor expansion coefficients of the EoS calculated on the lattice. They also can be related to experimental measurement in HICs, and can be used to probe the effect of the CEP [22].

Among the experiments designed to explore higher density regions of the QCD phase diagram in search for the CEP are the second Beam Energy Scan (BES-II) at RHIC scheduled for 2019-2020, and the next fixed-target Compressed Baryonic Matter (CBM) project at the Facility for Antiproton and Ion Research (FAIR), which is presently under construction at the Society for Heavy Ion Research (GSI) in Germany as well as the National Interscholastic Cycling Association (NICA) in Russia.

This dissertation is dedicated to the study of the QCD phase diagram using two field-theoretical approaches focused on the moderate-to-high region of μ_B where the CEP is expected to emerge. In the first approach [23], the low order baryon susceptibilities calculated on the lattice at imaginary μ_B are analyzed for different T. The purpose of the analysis was to perform a combined fit of these susceptibilities, to compute the higher order ones at zero μ_B. The susceptibilities at $\mu_B = 0$ allow one to have access to a finite region of the QCD phase diagram, by performing a Taylor expansion of the EoS around $\mu_B = 0$ in powers of μ_B/T. In the second part of this work [24], an approach based on the gauge/string duality is used to construct holographic black holes to mimic the EoS from the lattice at finite T and zero μ_B. Once the parameters of the black holes are fixed at $\mu_B = 0$, the model is able to compute the QCD EoS in the whole QCD phase diagram making a prediction for the existence and location of the CEP. This model could be used as the main theoretical tool to probe a signature of the CEP in HICs.

1.1.1 Dissertation Outline

This dissertation is organized as follows: the rest of this chapter is dedicated to give an introduction to the main aspects of QCD, including its global symmetries that give rise to the phases emerging in the QCD phase diagram. The lattice formulation of QCD is briefly introduced, and a connection between experiments in HICs and the QCD

phase diagram is mentioned. At the end of this chapter, a brief introduction to the gauge/string duality is given.

In Chapter 2, the imaginary chemical potential formalism is introduced and the simulations of the lower order baryonic susceptibilities calculated on the lattice are presented. Then, Chapter 3 summarizes the findings obtained by the combined fit of the low order baryonic susceptibilities, and shows the calculated higher order baryon susceptibilities at $\mu_B = 0$. In Chapter 4, the holographic Black Hole Model used to mimic the EoS in the QCD phase diagram is described. The main results of the investigation done with the black hole model are shown in Chapter 5. Finally, in Chapter 6 the findings of this dissertation are discussed.

1.2 Quantum Chromodynamics

QCD is the theory of strong interactions, with six different quarks as fundamental degrees of freedom. Table 1.1 summarizes several properties relating to each of the quark flavors. The significant difference between the masses of light and heavy quarks leads to a clear separation of scales: the u, d, and s quarks are the light flavor quarks, while the heavy flavor quarks correspond to the c, b, and t.

The QCD Lagrangian is obtained from the Lagrangian of free spin-$\frac{1}{2}$ quarks by applying the gauge principle with respect to the non-Abelian SU(3) color group. The symmetry of this group produces three distinct values of color charge commonly denoted as red, green, and blue, together with their corresponding anti-colors. The field quanta that carry the strong force are the gluons fields, which themself carry one of the eight possible non-singlet color–anti-color charge combinations. The Lagrangian for N_f

Quark	Symbol	Charge [e]	Mass [MeV]
up	u	+2/3	$2.2^{+0.5}_{-0.4}$
down	d	-1/3	$4.7^{+0.5}_{-0.3}$
strange	s	+2/3	95^{+9}_{-3}
charm	c	-1/3	$1,275^{+25}_{-35}$
bottom	b	+2/3	$4,180^{+40}_{-30}$
top	t	-1/3	$173,000^{+400}_{-400}$

TABLE 1.1: Symbol, mass and electric charge of the different flavors of quark [25].

quark flavors reads explicitly

$$L_{QCD} = \bar{\psi}_f \left(\mathrm{i} \not{D} - m_f \right) \psi_f - \frac{1}{4} G^a_{\mu\nu} G^{\mu\nu}_a \tag{1.1}$$

with field strength tensor $G^a_{\mu\nu} = \partial_\mu A^a_\nu - \partial_\nu A^a_\mu - g f^{abc} A^b_\mu A^c_\nu$, and covariant derivative $D^a_{\mu\nu} = \partial_\mu \delta^{ab} + \mathrm{i} g A^c_\mu T^{ab}_c$, where m_f is the current quark mass of the flavor f, g is the gauge coupling, T_c the generators of the fundamental representation of the SU(3) gauge group, and f^{abc} its structure constants. Contrary to Abelian theories like QED, the gauge-gluon fields couple to themselves, producing gluon–gluon vertices in addition to the quark–gluon ones. This feature makes QCD more challenging to deal with theoretically.

1.2.1 Symmetries of QCD

QCD, as a relativistic theory, is invariant under Lorenz Transformations of spacetime: rotations in space and boosts. However, the symmetry that defines its interaction is the

gauge symmetry. The quark and gluon fields transform under the local gauge transformations of the SU(3) color group

$$\psi(x) \to \Omega(x)\psi(x), \qquad A_\mu(x) \to \Omega(x)\left(A_\mu - \frac{\mathrm{i}}{g}\partial_\mu\right)\Omega^\dagger(x) \tag{1.2}$$

expanded by the generators of the group T^a as

$$\Omega(x) = \exp(-\mathrm{i}\theta^a(x)T^a) \tag{1.3}$$

for any field $\theta^a(x)$ with $a = \{1, 2, ..., 8\}$. This transformation generates the three color charges: blue, red and green.

The rest of the QCD symmetries are global. For instance, chiral symmetry is one of the most important approximate symmetries of QCD. It is realized by ignoring the quark masses; therefore, it is a good symmetry for the light quark sector. In this approximation, the QCD Lagrangian becomes invariant under the global U(N_f) transformation of the left and right-handed Weyl spinors

$$\psi_{L/R} = \frac{1}{2}\left(1 \pm \gamma^5\right)\psi, \qquad \psi_{L/R} \to U_{L/R}\psi_{L/R} \tag{1.4}$$

where $U_{L/R}$ is expanded by the generators T^a of the group U(N_f), as in Eq. (1.3). This transformation gives rise to the symmetry group $\mathrm{U}(N_f)_L \times \mathrm{U}(N_f)_R$ or given in terms of the vector/axial transformations,

$$\psi \to \exp(-\mathrm{i}\theta^a T^a)\psi \qquad \psi \to \exp(-\mathrm{i}\gamma^5\theta^a T^a)\psi\,, \tag{1.5}$$

the symmetry is represented by the group $\mathrm{U}(N_f)_V \times \mathrm{U}(N_f)_A \times \mathrm{U}(1)_B \times \mathrm{U}(1)_A$. The

$\mathrm{U}(1)_B$ symmetry is associated with baryon number conservation, while the anomalous axial $\mathrm{U}(1)_A$ symmetry is broken at the quantum level. The remaining symmetry $\mathrm{U}(N_f)_V \times \mathrm{U}(N_f)_A$ is spontaneously broken in the ground-state by effects of gluonic interactions and reduced to $\mathrm{SU}(N_f)_V$ giving rise to $N_f^2 - 1$ Goldstone Bosons.

Chiral symmetry is explicitly broken by the quark masses. In the vacuum, this symmetry is realized only by the u and d quarks because their masses are much smaller compared with the other quarks. The resulting Chiral symmetry $\mathrm{U}(2)_L \times \mathrm{U}(2)_R$ is spontaneously broken to the $\mathrm{SU}(2)$ isospin symmetry. The signal of the breaking of this symmetry is that the vacuum contains a chiral condensate $\langle\, \bar{\psi}\psi \,\rangle$, e.g., the pion, that in the chiral limit should be massless. In general, chiral symmetry will contribute to the dynamical generation of the chiral condensate. This condensate is responsible for the constituent mass of the quarks inside hadrons, that are about an order of magnitude more significant than their current masses listed in Table 1.1.

QCD has another approximate symmetry when considering the limit of infinitely heavy quarks. In this limit, which corresponds to the pure gauge sector of QCD, gluons are invariant under transformations of the $\mathrm{Z}(N)_c$ group. This symmetry is known as centre symmetry and can distinguish between the confinement and deconfinement of quarks. Gluons are neutral with respect to the centre symmetry charge while quarks carry a unit of this charge. To explain how this symmetry is related to confinement, let us write the operator that describes a static quark, the Polyakov Loop $P(\vec{x})$, defined as a Wilson loop closed around the periodic Euclidean time direction x_4

$$P(\vec{x}) = \frac{1}{N_c} \mathcal{P}\, \mathrm{Tr}_c \exp\left(\int_0^\beta \mathrm{d}x_4 A_0(\vec{x}, x_4) \right) \tag{1.6}$$

where $\mathcal{P}$ denotes path ordering, and $\beta = 1/T$. The Polyakov loop measures the free energy of the infinitely heavy quarks and is an order parameter for the spontaneous

breaking of the center symmetry. Then, the deconfined phase is associated with the breaking of the centre symmetry. A confined phase will have $\langle P \rangle = 0$ and the theory will be invariant under center transformations. On the other hand, in the deconfined phase, $\langle P \rangle \neq 0$ and the center symmetry will be broken.

1.2.2 Asymptotic Freedom and Confinement

One of the striking properties of QCD is its behavior at short distances. In quantum field theories, the physical quantities can be expanded through a perturbation series in power of a small parameter such as the coupling constant. In QCD, the strength of the coupling becomes small at shorter distances, or at large momentum transfer, leading to the phenomenon of asymptotic freedom.

The dependence of the coupling α_s on an energy scale Q can be determined by the renormalized group equation

$$Q^2 \frac{\partial \alpha_s(Q^2)}{\partial Q^2} = \beta\left(\alpha_s(Q^2)\right) , \tag{1.7}$$

where the scale Q should be larger than any other relevant parameter for this expansion to be valid.

The solution of Eq. (1.7) in 1-loop approximation is

$$\alpha_s(Q^2) = \frac{1}{\beta_0 \ln \frac{Q^2}{\Lambda^2_{QCD}}}, \qquad \text{with} \qquad \beta_0 = \frac{33 - 2N_f}{12\pi} \tag{1.8}$$

This equation introduces the scale Λ_{QCD} that signals the breakdown of the perturbation expansion. Eq. (1.8) demonstrates that for positive β_0, namely for $N_f < 17$, the coupling α_s runs to zero as the energy scale Q become much larger than the scale Λ_{QCD}. This means that quarks and gluons behave as almost free particles at these high energies.

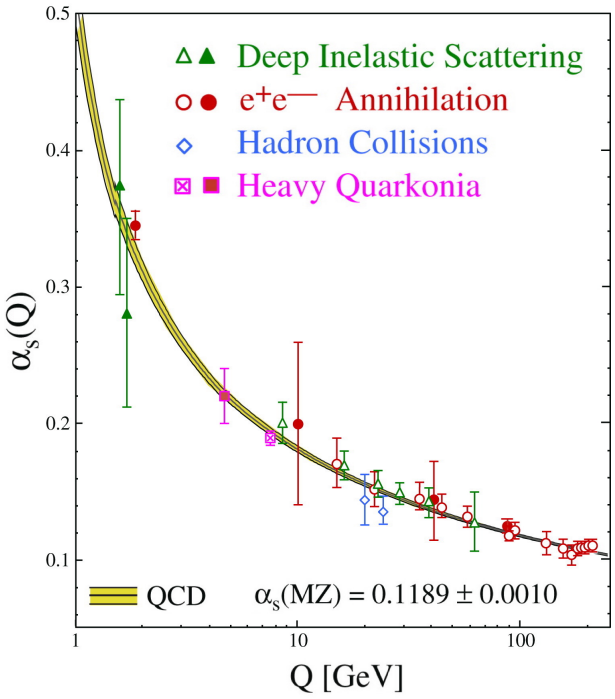

FIGURE 1.1: Summary of measurements of $\alpha_s(Q)$ as a function of the energy scale Q [26].

This effect is shown in Figure 1.1, which presents a summary of measurements of $\alpha_s(Q)$ taken by different experimental groups [26]. The solid lines in Figure 1.1 represent the QCD predictions made at 3 and 4 loops matched to reproduce the heavy quark pole masses $M_c = 1.5\,\mathrm{GeV}$ and $M_b = 4.7\,\mathrm{GeV}$ ($\Lambda_{QCD} \sim 200\,\mathrm{MeV}$).

The non-perturbative regime of QCD begins when asymptotic freedom breaks down at energies close to the Λ_{QCD} scale. The two mechanisms that govern the low energy region of QCD are spontaneous chiral symmetry breaking and confinement. In the last section, it was mentioned that the breaking of chiral symmetry produces a chiral condensate that contributes to the dynamical mass of the quarks, while confinement is a mechanism related to the breaking of the center symmetry in the pure gauge sector. However, the mechanism of confinement is not yet understood. It is supported by

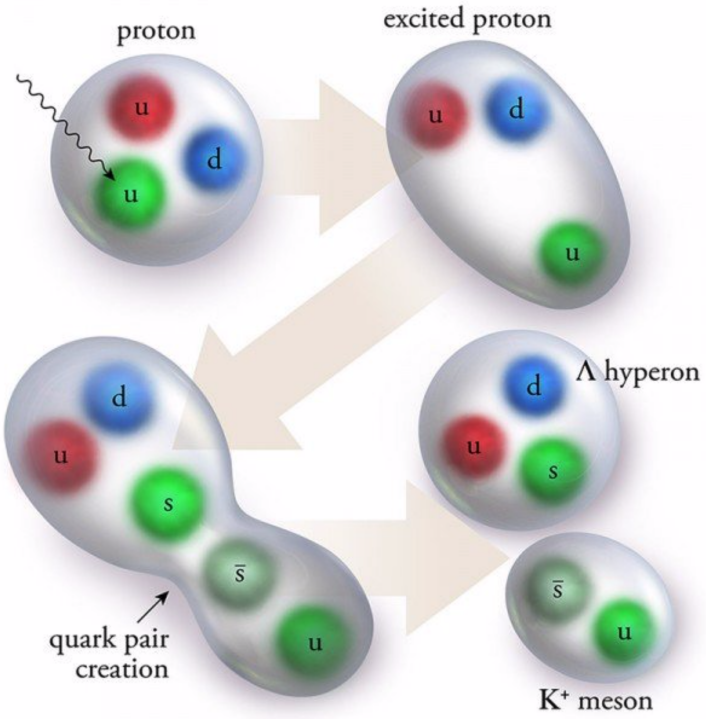

FIGURE 1.2: Confinement of Quarks inside a proton (upper left panel). When energy is added to the proton it jumps into an excited state (upper right panel). The tension in the string produces a pair of quarks (lower left panel). The process results into a hyperon and a K^+ meson (lower right panel).

the center symmetry and by the fact that the degrees of freedom directly observed in experiments are hadrons and not isolated quarks and gluons.

The confinement process is related to the fact that gluons themselves carry the color charge and interact among each other. In QED, a charge is screened by a cloud of virtual electron-positron pairs that align themselves to shield the bare charge. On the other hand, an isolated quark will be surrounded by virtual quarks and gluons of the same color. To avoid the infinite increase of the color charge, quarks always form combinations in such a way that the total color becomes neutral. They form hadrons: mesons made of quark–anti-quark pairs (carrying the same color and anti-color), or baryons

made of three quarks (carrying three different colors). The potential energy between a pair of quarks can be described as a function of the distance r as

$$V(r) = -\frac{4}{3}\frac{\alpha_s}{r} + kr\,. \tag{1.9}$$

When a pair of quarks is close together, the observed charge decreases until only the bare charge is seen. The second term vanishes and quarks feel the $\sim 1/r$ repulsive interaction. On the other hand, as one probes larger separations between quarks, the potential energy grows linearly with the separation of charges kr until it is high enough to create a new quark-antiquark pair. These again form two pairs of color neutral combinations such as the one illustrated in Figure 1.2.

What makes solving the theory of QCD so difficult when asymptotic freedom breaks down is precisely the change of dynamics from quarks and gluons to hadrons. The confined region of QCD, given by hadronic degrees of freedom, has been successfully described by the Hadron Resonance Model (HRG). The HRG is an effective model that assumes that a gas of interacting hadrons in thermal equilibrium can be approximated by a non-interacting gas of hadrons and their heavier resonances. The main input to the model is a list of hadrons usually provided by experimentally measured states (listed in the PDG), or calculated within the quark model framework. The pressure from this model is defined as the sum of the individual pressures of all baryons and mesons on the list. The explicit expression of the pressure at finite T and μ_B is

$$p_{HRG} = \sum_i \delta_i \frac{d_i T}{(2\pi)^3} \int \mathrm{d}^3\vec{p}\ \ln\left[1 + \delta_i \exp(-\beta(\sqrt{\vec{p}^{\,2} + m_i^2} - B_i\mu_B))\right] \tag{1.10}$$

where B_i is the conserved baryon number of particle i in the list, d_i is the individual degeneracy, m_i its mass, and $\delta_i = (-1)^{B_i+1}$. The HRG has shown a remarkable agreement with experimental observables such as particle yields/particle ratios, and is the main

theoretical tool to calculate the thermodynamics of confined hadrons near T_c.

1.2.3 Statistical Mechanics

Statistical mechanics plays an essential role in the description of the bulk properties of the QGP. These powerful techniques are used in the approaches that explore the QCD phase diagram such as the HRG model, lattice QCD and the holographic models. This section is dedicated to review some essential aspects of statistical mechanics and thermodynamics with a chemical potential μ_B.

A thermodynamical system is characterized by the extensive quantities entropy S, volume V, and number of particles N, and their conjugate intensive variables temperature T, pressure p, and chemical potential μ_B. The grand canonical ensemble is chosen considering that in quantum field theory the number of particles is not fixed. The partition function is obtained from the density operator ρ as follows

$$Z = \mathrm{Tr}\,\rho\,, \tag{1.11}$$

where $\mathrm{Tr}(..) = \sum_n \langle\, n|(..)|n\,\rangle$ and $\rho = \exp\left[-\beta(H - \mu_B N)\right]$.

The internal energy U, free energy F, and all other thermodynamic equilibrium quantities are obtained from the partition function as

$$F = -T\ln Z \qquad p = \frac{\partial(T\ln Z)}{\partial V} \qquad U = TS - pV + \mu_B N \tag{1.12}$$

$$S = \frac{\partial(T\ln Z)}{\partial T} \qquad N = \frac{\partial(T\ln Z)}{\partial \mu_B} \qquad F = U - ST - \mu_B N\,. \tag{1.13}$$

For a system with a fixed volume like the QGP, in the thermodynamic limit one usually defines the corresponding densities

$$f = \frac{F}{V} \qquad \epsilon = \frac{U}{V} \qquad s = \frac{S}{V} \qquad n = \frac{N}{V} \tag{1.14}$$

form where the trace anomaly I, the speed of sound c_s^2, and other thermodynamic relations can be given as

$$p = -f \qquad I = \epsilon - 3p \qquad c_s^2 = \frac{\mathrm{d}p}{\mathrm{d}\epsilon} \qquad \epsilon + p = sT \tag{1.15}$$

The specific heat at constant chemical potential, and the specific heat at constant volume, are defined as the second derivatives of the free energy

$$C_\mu = T\left(\frac{\partial s}{\partial T}\right)_\mu = -T\left(\frac{\partial^2 f}{\partial T^2}\right)_\mu \tag{1.16}$$

$$C_V = T\left(\frac{\partial s}{\partial T}\right)_V = -T\left[\frac{\partial^2 f}{\partial T^2} - \left(\frac{\partial^2 f}{\partial T \partial \mu_B}\right)^2 \left(\frac{\partial^2 f}{\partial \mu_B^2}\right)^{-1}\right]_\mu . \tag{1.17}$$

The baryon number susceptibility, $\chi_n = \chi_n^B(T, \mu_B)$ is obtained by taking the n-th derivative of the pressure with respect to the baryonic chemical potential

$$\chi_n = \frac{\partial^n}{\partial(\mu_B/T)^n}\left(\frac{p}{T^4}\right) . \tag{1.18}$$

1.2.4 Lattice QCD

The lattice formulation of QCD is the only approach that solves the strong interaction numerically from first principles in the non-perturbative regime. These calculations are performed by simulating the interaction of quarks and gluons on a discretized space-time lattice. The discrete lattice serves as an ultraviolet regulator that makes the field

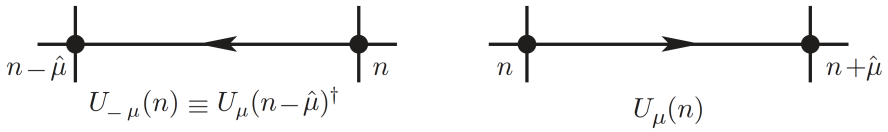

FIGURE 1.3: The link variables $U_{\mu}(n)$ and $U_{-\mu}(n)$.

formulation finite. The degrees of freedom are classical field variables living on the lattice. The basic tool for quantizing these fields is the Euclidian path integral. To construct the lattice approach, one starts from the continuum theory in Eq. (1.1), and applies the Matsubara formalism by performing a Wick rotation in the time variable ($x_4 = -\mathrm{i}x_0$). Then, one can write the Euclidian action, S^E, as a sum of the pure gauge, S^E_{glu}, which depends only on the bosonic degrees of freedom, and the fermionic part, S^E_{fer}, as

$$S^E = \mathcal{S}^E_{\mathrm{glu}} + \mathcal{S}^E_{\mathrm{fer}} = -\int_0^{\beta} dx_4 \int_V d^3x \left(\mathcal{L}^E_{\mathrm{glu}} + \mathcal{L}^E_{\mathrm{fer}}\right) . \tag{1.19}$$

Using this definition, the partition function at finite temperature is given by

$$\mathcal{Z} = \int \prod_{\mu} \mathcal{D}A_{\mu} \prod_{f} \mathcal{D}\psi_f \mathcal{D}\bar{\psi}_f \exp\left(-\mathcal{S}^E_{\mathrm{glu}} - \mathcal{S}^E_{\mathrm{fer}}\right) . \tag{1.20}$$

The first step in the lattice procedure is the replacement of the continuous space-time by a discrete lattice with separation a, such that in the limit $a \to 0$, the Euclidean continuum action is obtained. The fermionic degrees of freedom, $\psi(n)$, are placed on the lattice points labeled by the four-dimensional vector $n = \{n_\tau, n_x, n_y, n_z\}$, where the time component $n_\tau = 1, 2, ..., N_\tau$ and the spatial part $n_i = 1, 2, ..., N_s$. The size of the 4-dimensional lattice is $N_\tau \times N_s^3$. The temperature is defined in terms of the lattice separation as $T = 1/(aN_\tau)$. The simplest way to implement the discretization of the partial derivative of the fermion fields is by finite differences. However, this approach

introduces unphysical modes when recovering the continuum limit $a \to 0$ that have to be removed by procedures such as the Staggered fermions or Wilson fermions. The gauge fields are introduced as link variables $U_\mu(n)$ where the index defines the direction of the link as shown in Figure 1.3. The link $U_\mu(n)$ connects the sites n and $n+\mu$, and preserves the invariance under the SU(3) gauge transformation.

The integral over the fermionic field in the discretized version of Eq. (1.20) can be done analytically

$$\int \prod_f \mathcal{D}\psi_f \mathcal{D}\bar{\psi}_f \exp\left(-\mathcal{S}^E_{\text{fer}}\right) = \det[M] \tag{1.21}$$

producing the fermionic determinant $\det[M]$. Then, the partition function on the lattice is given by

$$\mathcal{Z} = \int \prod_\mu \mathcal{D}A_\mu \det[M] \exp\left(-\mathcal{S}^E_{\text{glu}}\right) \tag{1.22}$$

The expression in Eq. (1.22) resembles the Boltzmann factor in statistical mechanics weighted by $\det[M]$. If the $\det[M]$ is positively defined, the partition function on the lattice can be solved numerically by the use of Monte Carlo techniques. As powerful as lattice QCD is, Eq. (1.22) is pointing out two of the main limitations of this approach. The first one originates when introducing a real μ_B, which introduces a phase factor into the $\det[M]$ and prevents the use of Monte Carlo sampling. This is known as the "Fermi Sign Problem". The phase factor can be evaded if considering an imaginary μ_B, which leaves $\det[M] > 0$. Consequently, there are two approaches to study QCD on the lattice: one is to perform calculations at zero μ_B, and the other one is to do it at imaginary μ_B. The other limitation of the lattice approach is based on its formulation in the Euclidian imaginary time. This allows us to calculate directly equilibrium quantities,

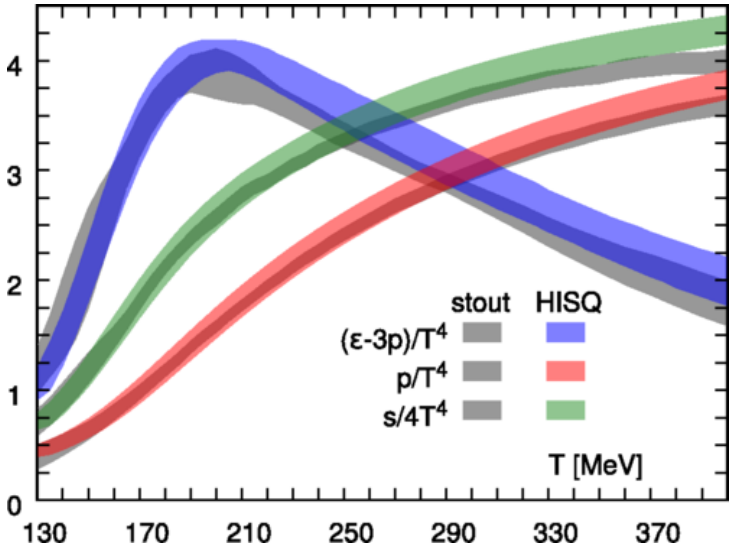

FIGURE 1.4: The comparison of the HISQ/tree (HotQCD [27]) and stout (WB [28]) results for the trace anomaly, the pressure, and the entropy density. Figure from [27].

while making the extraction of dynamical quantities difficult.

At this moment, lattice simulations have reached a remarkable precision and accuracy. Many observables have been calculated in the context of the QCD phase diagram (see [21] for a recent review). One of the most important achievements has been the calculation of the EoS at finite T and zero μ_B for physical quark masses and $N_f = 2 + 1$ quark flavors. It was obtained by two independent collaborations using different discretization methods [27, 28]. The comparison of the trace anomaly, pressure and entropy is shown in Figure 1.4. These observations show a rapid crossover transition at $T_c \sim 155$ MeV. The trace anomaly remains finite after T_c, which confirms that the QGP is strongly coupled right after the transition. In the next section the crucial importance of the EoS for a better understanding of the matter created in HICs will be emphasized.

1.3 Heavy-Ion Collisions and the QCD Phase Diagram

1.3.1 Phases of QCD

The phases of QCD reflect the conditions where the global symmetries of QCD, reviewed early in this chapter, are broken or restored. In the hadronic phase, chiral symmetry is broken while the center symmetry is restored. The opposite happens in the QGP phase, where chiral symmetry is restored and quarks and gluons are deconfined. This phase was predicted by asymptotic freedom, and it is expected that one of these symmetries changes below the energy scale $\Lambda_{QCD} \sim 200$ MeV. The heavy flavor quark masses are much larger than Λ_{QCD} and are not taken into account in the phases sketched in the QCD phase diagram.

The crossover transition from the hadronic phase to the QGP is calculated on the lattice at zero μ_B and it happens at $T_c \simeq 155 \pm 10$ MeV [4–9]. Both transitions, the chiral and deconfined, happen within the range of this crossover. On the other end of the QCD phase diagram, at low T and increasing baryonic density, the hadronic phase produces a degenerate Fermi system of quarks and gluons. What happens at this point is a topic of intense debate. A first-order phase transition from hadrons to the QGP is inferred from taking into account the effects of nonzero quark masses in chiral models [22]. If the density is very large, an attractive quark–quark channel, embedded in the weak-asymptotic region of QCD, makes the system unstable against the formation of Cooper pairs forming a state similar to the Bardeen–Cooper–Schrieffer (BCS) superconductivity. However, if the density is large but not large enough, the system develops chromomagnetic instabilities [29]. What happens in this region of QCD is important for the physics of compact stars but unfortunately it is the most uncertain region of the QCD phase diagram.

Most of the QCD phase diagram is still unexplored. The high T region is known

from resummed thermal perturbation theory for temperatures above $2-3T_c$ [30]. The lattice EoS state at zero μ_B can be extrapolated at the moment to a region limited by $\mu_B/T < 2$. The detection of this transition at higher densities, and the exploration of the existence of a CEP and a first order phase transition is one of the most important problems of high energy nuclear physics. Fortunately, the density region where the CEP could be found will be tested experimentally in the next decade in relativistic-heavy-ion-collisions. To answer these fundamental problems in QCD, the interplay between experimental results and theoretical models that describe strongly interacting matter at finite μ_B will be critical.

1.3.2 Relativistic-Heavy-Ion Colliders

The extreme conditions of T and μ_B needed to melt the nucleons of heavy atoms and create the QGP have been constantly reproduced in HICs such those taking place at RHIC at BNL, and LHC at CERN. By systematically varying the center-of-mass energy per nucleon ($\sqrt{s}$) of the colliding ion beams, those experiments can explore different regions of the QCD phase diagram. Depending on the location of the CEP, its effects may be probed using heavy ion collisions [22].

A simple sketch of the QCD phase diagram with a CEP and a first order phase transition line is shown in Figure 1.5. The dotted red line in the diagram signals the ratio $\mu_B/T = 2$, below which lattice calculations are available. The diagram indicates the positions where different experiments generate the QGP and the trajectories on which they cool down until they freeze-out. For instance, LHC with a large center of mass energy $\sqrt{s_{NN}} = 2.76 - 5.02$ TeV creates a QGP with very high T and small μ_B, recreating the conditions of the early Universe. The first phase of the Beam Energy Scan (BES) at RHIC created a medium with intermediate T and μ_B exploring the center of mass energy $\sqrt{s_{NN}} = 7.7 - 200$ GeV. Future runs of the BES with increased luminosity are

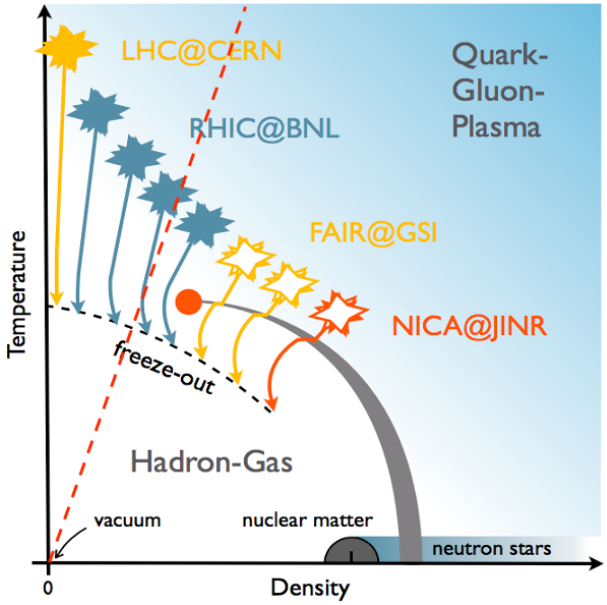

FIGURE 1.5: Sketch of the QCD phase diagram with a CEP indicating the trajectories, until they freeze-out, where different experiments generate the QGP. The red dotted line, which was added to the original picture, represents the ratio $\mu_B/T = 2$. Copyright: University of Bielefeld, Physics Department.

scheduled for 2019-2020, and fixed target experiments at RHIC are planned to reach even larger μ_B, searching for signatures of the existence of a CEP [31]. The future FAIR experiment at the GSI, currently under construction, will reach even higher μ_B producing collision energies of $\sqrt{s_{NN}} = 4.9$ GeV [32], while NICA at Dubna will reach energies of $\sqrt{s_{NN}} = 4.5$ GeV.

1.3.3 Stages of a Relativistic-Heavy-Ion-Collision

The evolution of a heavy ion collision is characterized by several stages, which can be described by different theoretical approaches. Figure 1.6 shows the standard schematic picture of a heavy ion collision. The initial state defines the condition under which

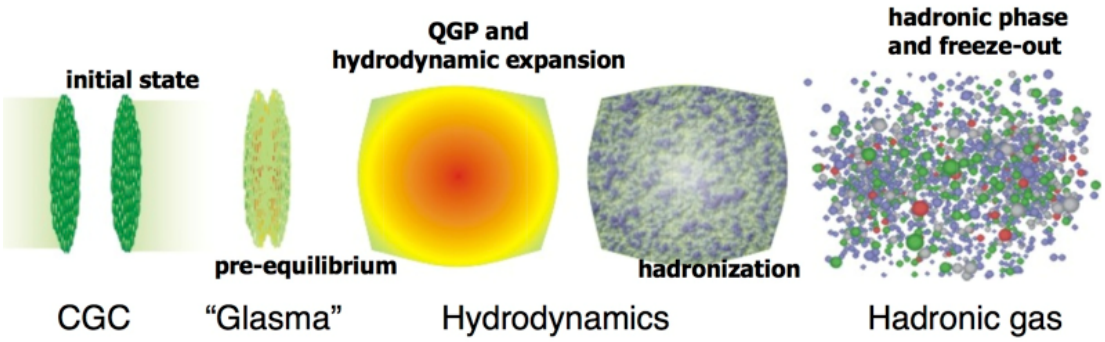

FIGURE 1.6: Stages of a relativistic-heavy-ion-collision. Figure from Steffen Bass, Quark Matter 2001

the collision takes place, and is driven by the geometry of the overlapping region between the colliding ions. This stage is usually modeled in the context of the Glauber model, or more recently on an event-by-event basis where fluctuations in the initial state are taken into account. Next, the Lorentz contracted heavy ions collide and produce a fireball in a highly excited pre-equilibrium state, which is dominated by the initial conditions. Shortly after the collision begins, the energy density reaches values that are more than ten times the normal nuclear matter one and temperatures above T_c. This stage is dominated by the Glasma phase, described by a combination of initial nuclear wave functions and classical gluon dynamics. The system deconfines forming the QGP and eventually reaching thermodynamic equilibrium. At this point the system expands and cools. It turns out that the bulk evolution during the expansion of the system can be successfully modeled by relativistic hydrodynamics. The system expands until hadronization occurs. Then hadrons reach a chemical freeze-out where all inelastic interactions cease. At his point, the chemical composition of the system is fixed. Due to event-by-event fluctuations of the initial conditions in heavy-ion collisions, fluctuations of conserved charges occur on an event-by-event basis so a distribution is formed.

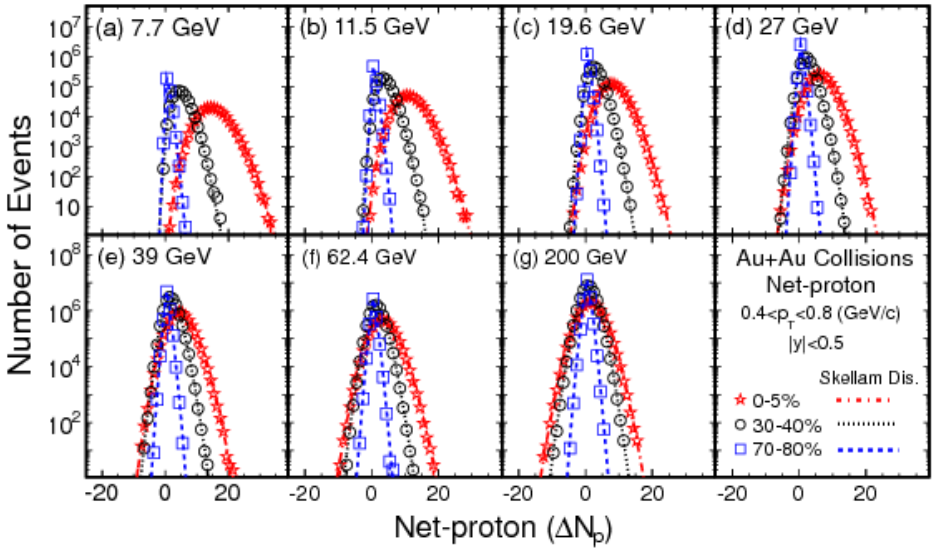

FIGURE 1.7: Net-proton multiplicity distributions in Au+Au collisions at various $\sqrt{s_{NN}}$ for 0%–5%, 30%–40%, and 70%–80% collision centralities at midrapidity [33].

The moments of those distributions are fixed at this point. Soon after chemical freeze-out, the system reaches the kinetic freeze-out, where all elastic interactions cease and the spectra of the particles that eventually reach the detector are fixed.

1.3.4 Baryon Number Susceptibilities

The baryon number susceptibility, χ_n, defined in Eq. (1.18)

$$\chi_n = \frac{\partial^n}{\partial(\mu_B/T)^n}\left(\frac{P}{T^4}\right)$$

is among the most relevant quantities used to explore the QCD phase diagram. It provides information about the effective degrees of freedom of a system, and is essential to the characterization of phase transitions. The baryon susceptibilities allow one to Taylor expand the pressure calculated at $\mu_B = 0$ to finite chemical potential as a power

of μ_B/T

$$\frac{P(T,\mu_B)-P(T,\mu_B=0)}{T^4}=\sum_{n=1}^{\infty}\frac{\chi_{2n}(\mu_B=0)}{(2n!)}\left(\frac{\mu_B}{T}\right)^{2n}.$$

This expansion is the main tool to access finite μ_B from first principle lattice calculations.

Susceptibilities are also important because they are related directly to the moments of the distribution measured in HICs. For instance, the net-proton multiplicity distributions in Au+Au measured on an event-by-event basis in STAR at midrapidity for various collision energies and centralities are shown in Figure 1.7. The distribution of net protons is a good approximation for the baryonic susceptibilities.To compare such distributions with theoretical predictions it is convenient to form volume-independent susceptibility ratios [34]

$$\begin{aligned}
\text{mean}: \quad M &= \chi_1 & M/\sigma^2 &= \chi_1/\chi_2 \\
\text{variance}: \quad \sigma^2 &= \chi_2 & S\sigma &= \chi_3/\chi_2 \\
\text{skewness}: \quad S &= \chi_3/\chi_2^{3/2} & \kappa\sigma^2 &= \chi_4/\chi_2 \\
\text{kurtosis}: \quad \kappa &= \chi_4/\chi_2^2 & S\sigma^3/M &= \chi_3/\chi_1 .
\end{aligned} \tag{1.23}$$

In a heavy-ion collision, the moments of the distributions are fixed at the chemical freeze-out. Comparing them to theoretical predictions such as lattice calculations or the holographic black hole model, allows one to extract T and μ_B at freeze-out [35–37].

Based on the theory of second order phase transitions, close to the CEP the susceptibilities and other thermodynamic variables scale with different powers of the correlation length ξ, which diverges at the CEP. For instance, at the mean field level $\chi_2 \sim VT\xi^2$ where V is the volume and, for a homogeneous system in equilibrium, it was shown

in [38] that the high order susceptibilities diverge with higher powers of ξ

$$\chi_2 \sim VT\xi^2 \qquad \chi_3 \sim VT^{3/2}\xi^{9/2} \qquad \chi_4 \sim VT^2\xi^7\,. \tag{1.24}$$

In heavy-ion collisions, the divergence of ξ is limited by the system size and by finite time effects. The comparison of ratios of susceptibilities with the moments of distributions in HICs may provide unique signatures for the detection of CEP in the QCD phase diagram. In [39], it was argued that the characteristic behavior of the ratio $\kappa\sigma^2$ has a non-monotonic dependence as it approaches the CEP. At the moment, there is a great interest in such comparison with the advent of the second run of the BES at RHIC, which will analyze fluctuations of conserved charges such as baryon number, electric charge, and strangeness, and their higher order cumulants with great precision.

1.4 AdS/CFT (Gauge/String) Duality

The AdS/CFT correspondence states a conjectured equivalence between certain conformal field theories (CFT) and certain gravitational theories in asymptotically Anti-de Sitter (AdS) spacetime. The duality was originated in string theory by studying D-branes and black holes [40–43], and has become a standard tool widely applied to study the non-perturbative behavior of different strongly correlated systems beyond CFT, including: QCD [44, 45], condensed matter systems [46–48], and quantum entanglement [49, 50]. In this context, a more appropriate name for this conjecture is a gauge/string duality or a holographic theory.

The AdS/CFT duality was originally stated as a specific equivalence between the $\mathcal{N} = 4$ SU(N_c) supersymmetric gauge theory and a type IIB string theory on $\mathrm{AdS}_5 \times S^5$ spacetime [40]. The gauge theory includes a gauge field, six real scalars fields, and four Weyl fermions in the adjoint representation, while the gravitational metric with

$AdS_5 \times S^5$ curvature is given by

$$\begin{aligned} ds^2 &= ds^2_{AdS_5} + R^2 d\Omega_5^2 \\ &= \frac{r^2}{R^2}\eta_{\mu\nu}dx^\mu dx^\nu + \frac{R^2}{r^2}\left(dr^2 + r^2\Omega_5^2\right) , \end{aligned} \tag{1.25}$$

where $\eta_{\mu\nu}$ is the Minkowski metric in four spacetime dimensions, x^μ is a Lorentz vector, R is the constant AdS radius, $d\Omega_5$ is the differential area of the five-dimensional sphere S^5, and r is the holographic coordinate. The metic in Eq. (1.25) contains the Poincare transformations of a global AdS spacetime. Following the discussion in [44], it is convenient to rewrite the metric using the radial coordinate $z = R^2/r$

$$ds^2 = \frac{R^2}{z^2}\left(\eta_{\mu\nu}dx^\mu \mathrm{d}x^\nu + dz^2 + z^2 d\Omega_5^2\right) . \tag{1.26}$$

In this equation, one can identify a four-dimensional Minkowski spacetime parametrized by each AdS_5 slice of constant z. According to the duality, a conformal gauge theory lives on the boundary of the AdS_5 when $r \to \infty$ or equivalent by $z \to 0$. In that sense, the gauge theory is a holographic projection of the five-dimensional gravitational theory.

The simplest AdS_5 Schwarzschild solution with metric obtained from Eq. (1.26) is an extremum of the action

$$S = \frac{1}{2\kappa_5^2}\int \mathrm{d}^5x\,\sqrt{-g}\left[\mathcal{R} + \frac{20}{R^2}\right] , \tag{1.27}$$

where κ_5 is the gravitational coupling, $\mathcal{R}$ is the Ricci scalar, and g the determinant of the metric, producing a dual CFT with speed of sound square $c_s^2 = 1/3$ as required by conformal symmetry.

The duality can be interpreted as a geometrization of the renormalization group

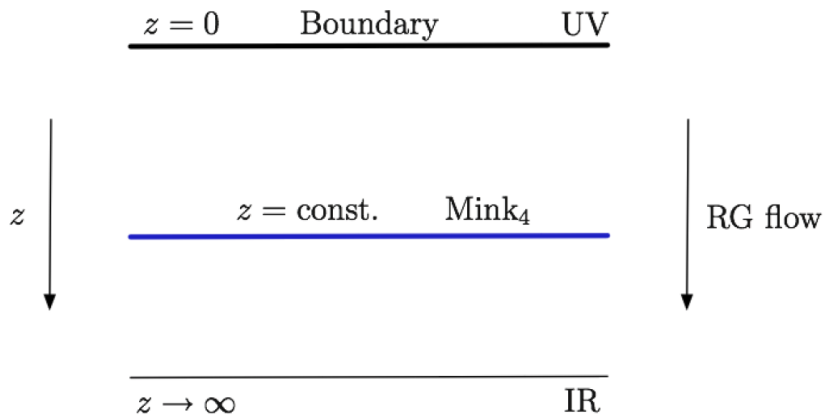

FIGURE 1.8: A geometric picture of AdS_5 (figure from [44].)

flow of a quantum field theory (QFT), where the radial coordinate z plays the role of the energy scale. This is illustrated in Figure 1.8. The region near the slice $z = 0$, where the asymptotic boundary in the gravitational theory is, corresponds to weak curvature or IR physics, while in the QFT this limit identifies physics at short distances or UV physics. Thus, a strongly interacting QFT will have a dual holographic gravitational description with a weak curvature. On the other hand, a strongly-coupled gauge theory at finite temperature has a dual gravitational theory in AdS spacetime with a d-dimensional black hole metric

$$ds_n^2 = -f(r)dt^2 + \frac{dr^2}{f(r)} + r^2 d\Omega_n^2 \tag{1.28}$$

where

$$f(r) = 1 - \frac{r_0}{r}^{d-3}, \qquad \text{and} \qquad \Omega_n = \frac{2\pi^{\frac{(n+1)}{2}}}{\Gamma\left(\frac{n+1}{2}\right)}, \tag{1.29}$$

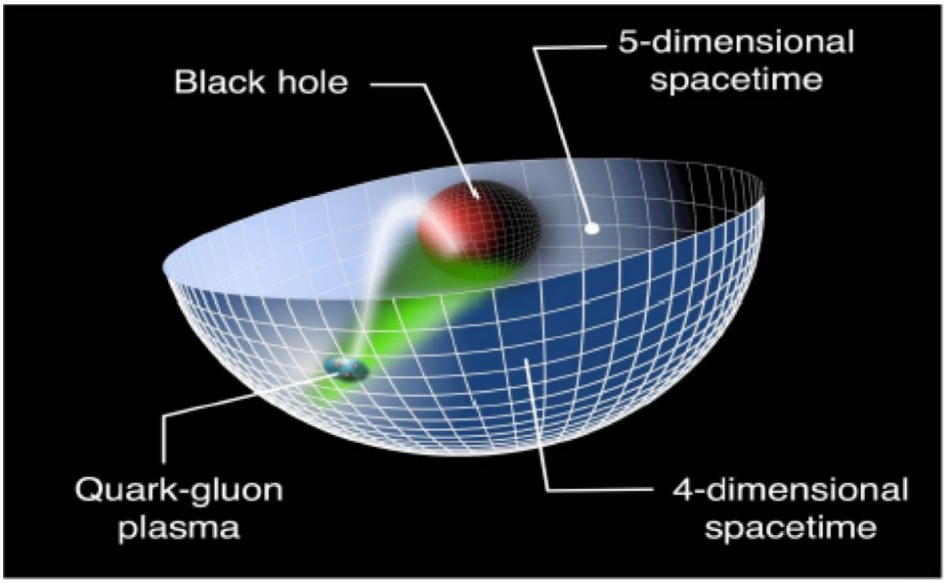

FIGURE 1.9: A schematic illustration of the duality between the asymptotic horizon of a holographic black hole and the QGP.

and r_0 is the radius at the horizon.

The black hole geometry appears in the dual description as a thermal system with a notion of temperature due to the Hawking radiation. Moreover, the black hole entropy is proportional to the area of the black hole horizon. In a five-dimensional black hole, the area of the horizon is a volume in a thermal system in four spacetime dimensions. Figure 1.9 shows a schematic illustration of a holographic black hole. It shows the near horizon represented by the read sphere, and the asymptotically far horizon where the strongly-coupled gauge theory lives.

Holographic black holes provide a mechanism to map strongly correlated thermodynamical systems into gravitational theories. Using the duality toolbox, it is possible to study equilibrium and out-of-equilibrium properties of the system. One of the most remarkable results obtained from holographic models, with at most two derivatives in

the gravity action, is the derivation of the ratio between the shear viscosity and the entropy density of a strongly coupled quantum fluid. It turns out to be $\eta/s = 1/4\pi$ [51–53]. Such a small value for η/s is compatible with the QGP produced in HICs such as RHIC and LHC [54–61]. The fact that η/s, in the strongly coupled regime of the QGP, is in agreement with holographic results increase their application to the study of real time phenomena in the strongly coupled QGP, which are otherwise inaccessible to direct calculations.

Chapter 4 of this dissertation studies a holographic model that includes charged black holes. The aim was to map the strongly interacting region of the QCD phase diagram to its dual weak gravitational theory and extract its thermodynamic variables. Contrary to most of the holographic studies, focused on studying properties of theCFT, the model used in Chapter 4 is engineered to mimic the behavior of the QGP at finite T and zero μ_B, which is highly non-conformal especially in the crossover region. Once the model parameters are fixed at $\mu_B = 0$, the model is able to calculate the behavior of the system at finite μ_B and made a prediction for the existence and location of the QCD CEP (shown in Chapter 5).

Chapter 2

Lattice QCD at Imaginary Chemical Potential

This chapter is devoted to giving a brief introduction to the lattice formulation of QCD. First, the naive representation of the fermionic fields is derived from the continuum theory. The non-physical modes that arise as a product of the discretization are discussed before introducing the Wilson formulation of QCD [62], the Symanzik improvement action [63–65], and the fermion staggered action [66]. Then, the introduction of finite temperature and imaginary chemical potential on the lattice is reviewed. The definitions for the susceptibilities at finite electric, baryonic, and strangeness chemical potentials are given, and the expressions to calculate them at imaginary chemical potential are shown.

2.1 Path Integrals and the Correlator Function

The lattice formalism is constructed from the path integral representation. The basic building blocks are the partition function and the correlator function, which are

reviewed in this section. Starting from the QCD action in Minkowski space, the continuum theory is defined in the Euclidian formalism by performing a Wick rotation from real-time to imaginary-time, denoted by $x_4 = -\mathrm{i}x_0$. In this convention, the Minkowski metric is replaced by the Euclidian metric δ_{ii} with no distinction between covariant and contravariant vectors. The QCD Lagrangian with Euclidian metric is written for convenience as a sum of the matter fields, where fermions are interacting with gluons, and the pure gauge part, depending only on the gluonic degrees of freedom as

$$S_{\mathrm{QCD}} = S_{\mathrm{fer}}[A, \psi, \bar{\psi}] + S_{\mathrm{glu}}[A]\,. \tag{2.1}$$

The fermionic action is written in compact vector notation as

$$S_{\mathrm{fer}}[A, \psi, \bar{\psi}] = \int \mathrm{d}^4x \bar{\psi}_f \left(\mathrm{i}\not{D} - m_f\right) \psi_f\,. \tag{2.2}$$

Explicitly, Eq. (2.2) reads

$$S_{\mathrm{fer}}[A, \psi, \bar{\psi}] = \sum_{f=1}^{N_f} \sum_{\alpha,\beta} \sum_{c,d} \int \mathrm{d}^4x \bar{\psi}^f_{\alpha\, c} \left((\gamma_\mu)_{\alpha\beta} \left\{ \delta_{cd} \partial_\mu + \mathrm{i}g (A_\mu)_{cd} \right\} + m^f \delta_{\alpha\beta} \delta_{cd} \right) \psi^f_{\beta\, d} \tag{2.3}$$

where the sum is on the number of flavors N_f, $\{\alpha, \beta\} = \{1, 2, 3, 4\}$ are the Euclidian indexes, and $\{c, d\} = \{r, b, g\}$ the color indexes. The γ-matrices obey the Euclidian anti-commutation relations $\{\gamma_\mu, \gamma_\nu\} = 2\delta_{\mu\nu}$.

The gluon action is written as a trace of the contracted force tensor $\mathrm{F}_{\mu\nu}$

$$S_{\mathrm{glu}}[A] = \frac{1}{4} \int \mathrm{d}^4x\, \mathrm{Tr}\left[\mathrm{F}_{\mu\nu}\mathrm{F}^{\mu\nu}\right]. \tag{2.4}$$

The gluon fields expand on the SU(3) color space in terms of the generators T_i

$$A_\mu = \sum_{i=1}^{8} A_\mu^i T_i \tag{2.5}$$

similarly, the gluon field force tensor is defined as

$$\mathrm{F}_{\mu\nu} = \sum_{i=1}^{8} \mathcal{F}_{\mu\nu}^i \qquad \text{with} \qquad \mathcal{F}_{\mu\nu}^i = \partial_\mu A_\nu^i - \partial_\nu A_\mu^i - f_{ijk} A_\nu^j A_\mu^k \,, \tag{2.6}$$

where f_{ijk} is the SU(3) group constant.

One of the most significant observables in QCD in connection to the lattice formulation is the energy spectrum and the matrix elements of operators. They can be determined from the Euclidian correlation function defined for two operators, $\hat{\mathcal{O}}_2$ and $\hat{\mathcal{O}}_1$, as

$$\begin{aligned} \langle\, \hat{\mathcal{O}}_2(t)\hat{\mathcal{O}}_1(0)\,\rangle_{\mathcal{T}} =& \frac{1}{\mathrm{Z}_{\mathcal{T}}} \mathrm{Tr}\left[\mathrm{e}^{-(\mathcal{T}-t)\hat{\mathcal{H}}}\hat{\mathcal{O}}_2 \mathrm{e}^{-t\hat{\mathcal{H}}}\hat{\mathcal{O}}_1\right] \\ =& \sum_{m,n} \mathrm{e}^{-(\mathcal{T}-t)E_m} \langle m|\hat{\mathcal{O}}_2|n\rangle \mathrm{e}^{-t\,E_n} \langle n|\hat{\mathcal{O}}_1|m\rangle \,. \end{aligned} \tag{2.7}$$

The parameters $\{t, \mathcal{T}\}$ are real numbers denoting Euclidean times. On the first line of Eq. (2.7), the $\mathcal{T}$-correlator is written in terms of quantum field operators, and in the second line as a sum over eigenstates of the Hamiltonian operator $\hat{\mathcal{H}}$. Here, the term $\mathrm{Z}_{\mathcal{T}} = \mathrm{Tr}[\mathrm{e}^{-\mathcal{T}\hat{\mathcal{H}}}]$ is a normalization factor. In the limit $\mathcal{T} \to \infty$, only the lowest energy state projected by the transporter term $\mathrm{e}^{-\mathcal{T}\hat{\mathcal{H}}}$ will survive

$$\lim_{\mathcal{T}\to\infty} \langle\, \hat{\mathcal{O}}_2(t)\hat{\mathcal{O}}_1(0)\,\rangle_{\mathcal{T}} = \sum_n \langle 0|\hat{\mathcal{O}}_1|n\rangle \langle n|\hat{\mathcal{O}}_2|0\rangle \mathrm{e}^{-t\,E_n} \tag{2.8}$$

where the lowest energy E_0 corresponds to the vacuum term denoted by the state $\langle 0|$. The energy level, E_n, is the difference between the n-energy eigenvalue and the vacuum

energy.

The expression in Eq. (2.7) is a convenient mathematical tool to extract energy levels and matrix elements which can be calculated on the lattice by expressing the correlator function in the path integral formalism

$$\langle \hat{\mathcal{O}}_2(t)\hat{\mathcal{O}}_1(0) \rangle_{\mathcal{T}} = \frac{1}{Z_{\mathcal{T}}} \int \mathcal{D}[A]\mathcal{D}[\psi]\mathcal{D}[\bar{\psi}] \mathrm{e}^{-S_{\mathrm{QCD}}} \mathcal{O}_2[A,\psi,\bar{\psi}]\mathcal{O}_1[A,\psi,\bar{\psi}] \tag{2.9}$$

where the measures for gluon and quark fields are defined as

$$\mathcal{D}[A] = \prod_x \mathrm{d}A(x) \qquad \mathcal{D}[\psi] = \prod_x \mathrm{d}\psi(x) \qquad \mathcal{D}[\bar{\psi}] = \prod_x \mathrm{d}\bar{\psi}(x) \tag{2.10}$$

The expression in Eq. (2.9) connects QCD with the techniques used in statistical mechanics by interpreting the weight $\mathrm{e}^{-S_{\mathrm{QCD}}}$ as a Boltzmann factor, and the normalization term $Z_{\mathcal{T}}$ as the grand canonical partition function defined as

$$Z_{\mathcal{T}} = \int \mathcal{D}[A]\mathcal{D}[\psi]\mathcal{D}[\bar{\psi}] \mathrm{e}^{-S_{\mathrm{QCD}}} \tag{2.11}$$

The grand partition function is the most important object to be computed on the lattice, from which all thermodynamical quantities, including the susceptibilities of conserved charges analyzed in this dissertation, are determined.

2.2 QCD on the Lattice

As discussed in the introduction, the lattice procedure consists of discretizing the space-time path integral representation of QCD into a four-dimensional grid with spacing a. The points are labeled by a vector $n = \{n_\tau, n_x, n_y, n_z\}$, with the time component $n_\tau = \{1, 2, ..., N_\tau\}$ and the spatial part $n_i = \{1, 2, ..., N_s\}$. The number of points in the

lattice is $N_\lambda = N_\tau \times N_s^3$, and the volume $V = N_\lambda * a^4$. Periodic boundary conditions are imposed to minimize the effects of the boundaries by connecting the first index in each direction with the last one. The integrals over the four Euclidian space are replaced by the sum over all the lattice points

$$\int \mathrm{d}x^4 \to \sum_{N_\lambda} a^4 \,. \tag{2.12}$$

The quark fields $\psi(n)$ and $\bar{\psi}(n)$ are placed at each of the lattice points $n = \{1, 2, ..., N_\lambda\}$. In this discrete scheme, the Lagrangian and any other observable have to be constructed in such a way that does not violate gauge invariance. To begin with, let us describe the most straightforward representation of free fermions on the lattice and motivate the introduction of link variables as transporters of the color field.

2.2.1 The Naive Discretization

Let us consider the Lagrangian for a system of free fermions on the lattice. The simplest way to implement the discretization of the partial derivatives of the fermion fields is by finite differences. Using different schemes will lead to different discretization errors, which scale as a power of the lattice separation a. For instance, using forward and central differences will lead to errors proportional to $\mathcal{O}(a)$ and $\mathcal{O}(a^2)$ respectively, and to $\mathcal{O}(a^4)$ with the 4-points central difference

$$\begin{aligned} f'(x) =& \frac{f(x+a) - f(x)}{a} + \mathcal{O}(a) \\ f'(x) =& \frac{f(x+a) - f(x-a)}{2a} + \mathcal{O}(a^2) \\ f'(x) =& \frac{-f(x+2a) + 8f(x+a) - 8f(x-a) + f(x-2a)}{12a} + \mathcal{O}(a^4) \,. \end{aligned} \tag{2.13}$$

However, it is vital that the discretized theory converges to QCD in the continuum as ones takes the limit of $a \to 0$.

In the so-called Naive representation, the partial derivative of the fermionic field is replaced by a central difference

$$\partial_\mu \psi \to \frac{1}{2a} \left(\psi(n + \hat{\mu}) - \psi(n - \hat{\mu}) \right) , \tag{2.14}$$

where the symbol $\hat{\mu} = \{\hat{1}, \hat{2}, \hat{3}, \hat{4}\}$ changes the lattice point n by one unit of the lattice spacing a in the direction $\{1, 2, 3, 4\}$.

The discrete Lagrangian for the naive free fermions becomes

$$S^0_{\text{fer}}[\psi, \bar{\psi}] = a^4 \sum_n \bar{\psi}(n) \left(\sum_{\hat{\mu}} \gamma_\mu \frac{\psi(n + \hat{\mu}) - \psi(n - \hat{\mu})}{2a} + m\psi(n) \right) . \tag{2.15}$$

Performing a gauge transformation $\Omega(n)$, the fermionic fields transform as

$$\psi(n) \to \Omega(n)\psi(n) \qquad\qquad \bar{\psi}(n) \to \bar{\psi}(n)\Omega^\dagger(n) . \tag{2.16}$$

The mass term in Eq. (2.15) is invariant under the gauge transformation $\Omega(n)$, but not the terms in the discretized derivative

$$\begin{aligned} \bar{\psi}(n)\psi(n + \vec{\mu}) &\to \bar{\psi}(n)\Omega^\dagger(n)\Omega(n + \bar{\mu})\psi(n + \vec{\mu}) \\ \bar{\psi}(n)\psi(n - \vec{\mu}) &\to \bar{\psi}(n)\Omega^\dagger(n)\Omega(n - \bar{\mu})\psi(n - \vec{\mu}) . \end{aligned} \tag{2.17}$$

Now, the fermionic fields are coupled to gauge fields to make the theory gauge invariant under the corresponding gauge group. Here is the difference between the continuum and discrete theory. The lattice separation in Eq. (2.15) has introduced a non-local interaction in the theory reflected in the gauge transformation in Eq. (2.17).

This non-physical artifact must disappear when taking the continuum limit of $a \to 0$. However, to make the theory gauge invariance on the lattice, an object similar to the gauge transporter has to be defined to move the gauge fields. The gauge transporter from coordinate x to coordinate y is defined as

$$G(x,y) = \mathrm{P}\exp\left(\mathrm{i}g\int_{\mathrm{C}(x,y)} A\cdot \mathrm{d}s\right) \tag{2.18}$$

where P is the time ordering operator, A the gauge field, and the integral is over the contour $\mathrm{C}(x,y)$ from point x to point y. The gauge transporter transforms as

$$G(x,y) \to \Omega(x)G(x,y)\Omega^{\dagger}(y) \tag{2.19}$$

In the case where the two coordinates (x,y), have the separation as the lattice $y = x + a$, the gauge transporter is defined on the lattice as a link variable U_μ. Using lattice notation, the gauge link is given by

$$G(n,n+\hat{\mu}) \to U_\mu(n) = \exp\left(\mathrm{i}gaA_\mu\right) \tag{2.20}$$

For notation convenience, a link with a negative index is defined as

$$U_{-\mu}(n) \equiv U_\mu(n-\hat{\mu}) = \exp\left(-\mathrm{i}gaA_\mu\right)\ ; \tag{2.21}$$

the direction of both links is shown in the left panel of Figure 2.1. The link variables under a gauge transformation become

$$U_\mu(n) \to \Omega(n)U_\mu(n)\Omega^{\dagger}(n+\hat{\mu}) \qquad U_{-\mu}(n) \to \Omega(n)U_{-\mu}(n)\Omega^{\dagger}(n-\hat{\mu})\,. \tag{2.22}$$

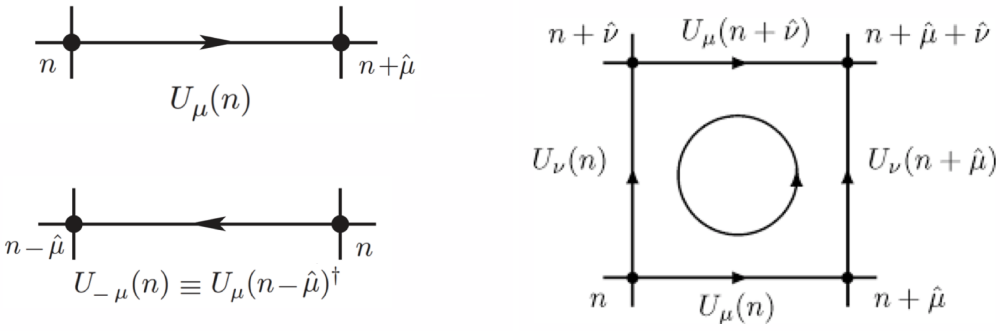

FIGURE 2.1: The gauge links $U_\mu(n)$ and $U_{-\mu}(n)$ (left panel). The four link variables which build up the gauge invariant plaquette $U_{\mu\nu}(n)$ (right panel)

Thus, the gauge fields are represented by link variables that carry the color charge among the lattice points where the fermion fields are placed.

The naive representation of the fermion action in Eq. (2.15) is now written with the gauge links as a gauge invariant action

$$S_{\text{fer}}[U,\psi,\bar{\psi}] = a^4 \sum_n \bar{\psi}(n) \Bigg(\sum_\mu \gamma_\mu \frac{U_\mu(n)\psi(n+\hat{\mu}) - U_{-\mu}(n)\psi(n-\hat{\mu})}{2a} + m\psi(n) \Bigg) \tag{2.23}$$

The link variables are considered as the fundamental variables on the lattice, over which the path integrals are integrated, and the gauge action is constructed.

From the transformation properties of the link variables in Eq. (2.22), it is straightforward to construct gauge invariant objects. For instance, the lattice version of the gauge transporter is formed by a product of link variables $P[U]$, which under gauge

transformations becomes

$$P[U] = U_{\mu_0}(n)U_{\mu_1}(n+\hat{\mu}_0)....U_{\mu_N}(n+\hat{\mu}_{N-1}) = \prod_{n,\mu} U_\mu(n)$$
$$\rightarrow \Omega(\mu_0)P[U]\Omega^\dagger(\mu_N)\,. \tag{2.24}$$

Thus, a gauge-invariant object can be constructed by coupling $P[U]$ to a fermion field at the end points $\bar{\psi}(\mu_0)P[U]\bar{\psi}(\mu_N)$. An alternative way is to ch0ose a closed path and take the trace over the product of link variables. This combination of links is called a Wilson loop and is denoted by

$$L[U] = \mathrm{Tr}\left[\prod_{n,\mu} U_\mu(n)\right]$$
$$\rightarrow \mathrm{Tr}\left[\Omega(\mu_0)\prod_{n,\mu} U_\mu(n)\Omega^\dagger(\mu_N)\right] = L[U]\,. \tag{2.25}$$

The shortest closed loop of link variables is called a plaquette $U_{\mu\nu}(n)$ defined as

$$U_{\mu\nu}(n) = U_\mu(n)U_\nu(n+\hat{\mu})U_{-\mu}(n+\hat{\mu}+\hat{\nu})U_{-\nu}(n+\hat{\nu})$$
$$= U_\mu(n)U_\nu(n+\hat{\mu})U_\mu^\dagger(n+\hat{\nu})U_\nu^\dagger(n)\,. \tag{2.26}$$

It is a loop over four connected links, as shown in the right panel of Figure 2.1. The relation $U_{-\mu}(n) = U_\mu^\dagger(n-\hat{\mu})$ was used to simplify the expression for the plaquette. The plaquettes will be the bases for the construction of the Wilson gauge action that is reviewed in the next section.

2.2.2 Gauge Action

The first formulation of the gauge action was presented by Wilson in 1975 [62]. The Wilson gauge action is constructed as a sum over all plaquettes on the lattice

$$S_W[U] = \frac{2}{g^2} \sum_n \sum_{\mu<\nu} \Re \,\mathrm{Tr}\left[1 - U_{\mu\nu}(n)\right] \,, \tag{2.27}$$

where $\Re$ represent the real part of the trace and g the gauge coupling. By expanding the link variables in terms of the gauge fields A_μ up to an order $\mathcal{O}(a^2)$ and using the Baker-Campbell-Hausdorff formula $\mathrm{e}^A\mathrm{e}^B = \mathrm{e}^{A+B+\frac{1}{2}[A,B]+\cdots}$, one can show that (see [67])

$$\begin{aligned} U_{\mu\nu}(n) &= \mathrm{e}^{\mathrm{i}a^2 g\,\mathrm{F}_{\mu\nu}(n)+\mathcal{O}(a^3)} \\ &= 1 + \mathrm{i}a^2 g\,\mathrm{F}_{\mu\nu}(n) - \frac{1}{2}\left(a^2 g\,\mathrm{F}_{\mu\nu}(n)\right)^2 + \ldots \end{aligned} \tag{2.28}$$

and in the limit $a \to 0$ the Wilson action becomes the continuum action

$$\begin{aligned} \lim_{a\to 0} S_W[U] &= \lim_{a\to 0} \frac{2}{g^2} \sum_n \sum_{\mu<\nu} \mathrm{Tr}\left[\frac{1}{2} a^4 g^2 \mathrm{F}_{\mu\nu}\mathrm{F}^{\mu\nu}\right] \\ &= \frac{1}{4}\int \mathrm{d}x^4\, \mathrm{Tr}\left[\mathrm{F}_{\mu\nu}\mathrm{F}^{\mu\nu}\right] . \end{aligned} \tag{2.29}$$

The Wilson gauge action provides a discretization with an error proportional to the lattice spacing $\mathcal{O}(a^2)$. However, the discretization of the gauge action is not unique. In Eq. (2.13), it was shown that the error using the finite difference method is reduced by adding sample points. In a similar way, the Wilson action can be improved by adding Wilson loops consisting of two plaquettes

$$\begin{aligned} R_{\mu\nu}(n) &= U_\mu(n) U_\mu(n+\hat{\mu}) U_\nu(n+2\hat{\mu}) U_{-\mu}(n+2\hat{\mu}+\hat{\nu}) U_{-\mu}(n+\hat{\mu}+\hat{\nu}) U_{-\nu}(n+\hat{\nu}) \\ &= U_\mu(n) U_\mu(n+\hat{\mu}) U_\nu(n+2\hat{\mu}) U_\mu^\dagger(n+\hat{\mu}+\hat{\nu}) U_\mu^\dagger(n+\hat{\nu}) U_\nu^\dagger(n) \,. \end{aligned} \tag{2.30}$$

The improved Symanzik gauge action, including the Wilson loops $R_{\mu\nu}(n)$, is written as

$$S_{\rm Sym}[U] = \frac{2}{g^2}\sum_n\sum_{\mu<\nu}\left[\frac{5}{3}\left(1-\frac{1}{3}\Re(U_{\mu\nu})\right) - \frac{1}{12}\left(1-\frac{1}{3}\Re(R_{\mu\nu})\right)\right]. \tag{2.31}$$

The inclusion of improved $R_{\mu\nu}(n)$ in the Symanzik gauge action decreases the discretization error, and improves the convergence to the continuum limit. This action was introduced in [63], and is used in the lattice calculations analyzed in Chapter 3 of this dissertation.

The link variables U_μ in the gauge action are introduced as members of the $SU(N)$ group. As discussed in [67], for the integration over a compact lie group, the Haar measure is used, defined as

$$\mathrm{d}U = c\sqrt{\det\left[g(w)\right]}\prod_k \mathrm{d}w^{(k)}\,, \tag{2.32}$$

where c is a normalization constant, $U(w)$ is an element of the lie group, and $g(w)$ is the metric tensor.

2.2.3 Fermion Action

The naive discretization of the fermions on the lattice was obtained in Eq. (2.23), which is rewritten here in a quadratic form

$$S_{\rm fer}[U,\psi,\bar\psi] = a^4\sum_{n,m}\sum_{\alpha,\beta}\sum_{a,b}\bar\psi(n)_{\alpha,a}D(n|m)\psi(m)_{\beta,b}\,, \tag{2.33}$$

with the Dirac operator

$$D(n|m) = \sum_\mu(\gamma_\mu)\frac{U_\mu(n)_{ab}\delta_{n+\bar\mu,m} - U_{-\mu}(n)_{ab}\delta_{n-\bar\mu,m}}{2a} + m\,\delta_{\alpha\beta}\delta_{ab}\delta_{nm}\,. \tag{2.34}$$

The fermion propagator on the lattice is the inverse of this Dirac operator. In momentum space for massless fermions, the propagator is

$$D(p)^{-1} \sim \frac{1}{\sum_\mu \sin^2(p_\mu a)}, \tag{2.35}$$

while in the limit when $a \to 0$ it reproduces the continuum limit

$$\lim_{a\to 0} D(p)^{-1} \sim \frac{1}{p^2} \tag{2.36}$$

with one pole at $p = (0,0,0,0)$ corresponding to one fermion. On the lattice, on the other hand, there is a pole every time all components of the momentum p contain zeros and/or a value of $\frac{\pi}{a}$. In total, there are sixteen fermions on the lattice, fifteen of which are unphysical poles called "doublers".

There are different strategies to deal with the "doublers". Possibly, the simplest way to get rid of the unwanted modes was suggested by Wilson and consists of adding an extra term to the Dirac operator.

$$D(p) = m + \frac{1}{a}\sum_\mu \gamma_\mu \sin(p_\mu a) + \frac{1}{a}\left[a - \cos(p_\mu a)\right] \tag{2.37}$$

the last term, called the Wilson term, cancels the "doublers". The Wilson action then reads

$$S^W_{\text{fer}}[U,\psi,\bar\psi] = \sum_f a^4 \sum_{n,m} \bar\psi^f(n) D^f_W(n|m)\psi^f(m) \tag{2.38}$$

where

$$D_W^f(n|m) = \left(m^f + \frac{4}{a}\right)\delta_{\alpha\beta}\delta_{ab}\delta_{nm} - \frac{1}{2a}\sum_\mu \Big[(1-\gamma_\mu)_{\alpha\beta}U_\mu(n)_{ab}\delta_{n+\hat{\mu},m} + (1+\gamma_\mu)_{\alpha\beta}U_{-\mu}(n)_{ab}\delta_{n-\hat{\mu},m}\Big] \tag{2.39}$$

is the Dirac operator with the inclusion of the Wilson term.

The Wilson fermion action discretization error is expected to be $\mathcal{O}(a)$. In a similar way that in the gauge action, the error term could be improved, in this case to $\mathcal{O}(a^2)$, by using the Symanzik method. The idea is to write an effective action with the symmetries of QCD but expressed as expansion in powers of a. The coefficients of the terms are chosen in order to cancel higher powers of the error, similarly to the finite difference method. The first correction term to the Wilson action is [64, 65]

$$S_{\text{fer}}^{\text{Sym}}[U,\psi,\bar{\psi}] = S_{\text{fer}}^{W}[U,\psi,\bar{\psi}] + c_{sw}\,a^5\sum_n\sum_{\mu<\nu}\bar{\psi}(n)\frac{1}{2}\sigma_{\mu\nu}\hat{\mathrm{F}}_{\mu\nu}(n)\psi(n)\,, \tag{2.40}$$

where $\sigma = \frac{[\gamma_\mu,\gamma_\nu]}{2i}$, c_{sw} is the Sheikholeslami-Wohlert coefficient defined in [68], and $\hat{\mathrm{F}}_{\mu\nu}$ is a discrete version of the force tensor $\mathrm{F}_{\mu\nu}$. The Symanzik method as well as a possible way to discretize the force tensor is described in [67].

In the calculations analyzed in Chapter 3 of this dissertation, the staggered fermions method was used to deal with the "doubler" modes [66]. The idea of staggered fermions is to construct a diagonal action in spinor space by performing the staggered transformation in the fermion fields

$$\psi(n) \to \gamma_1^{n_1}\gamma_2^{n_2}\gamma_3^{n_3}\gamma_4^{n_4}\psi(n) \qquad \bar{\psi}(n) \to \bar{\psi}(n)\gamma_4^{n_4}\gamma_3^{n_3}\gamma_2^{n_2}\gamma_1^{n_1}\,. \tag{2.41}$$

In that way, the sixteen fermions that are in the naive fermion action are reduced to four groups containing an exact copy of each other

$$S^S_{\text{fer}}[U,\psi,\bar{\psi}] = a^4 \sum_n \bar{\psi}(n) \Bigg(\sum_{\hat{\mu}} \eta_\mu \frac{U_\mu(n)\bar{\psi}(n+\hat{\mu}) - U_{-\mu}(n)\psi(n-\hat{\mu})}{2a} + m\chi(n) \Bigg) \tag{2.42}$$

the γ-matrices, which mix the spinor indexes, are now diagonal and real η-matrices defined in terms of the lattice vector $n = \{n_1, n_2, n_3, n_4\}$ as

$$\eta_1(n) = 1 \quad \eta_2(n) = (-1)^{n_1} \quad \eta_3(n) = (-1)^{n_1+n_2} \quad \eta_4(n) = (-1)^{n_1+n_2+n_3}\,. \tag{2.43}$$

Three of those copies can be dropped leaving only one denoted by χ, a Grassmann-valued field containing the physical fermion and three "doublers". The staggered fermion action becomes

$$S^S_{\text{fer}}[U,\chi,\bar{\chi}] = a^4 \sum_n \bar{\chi}(n) \Bigg(\sum_{\hat{\mu}} \eta_\mu \frac{U_\mu(n)\chi(n+\hat{\mu}) - U_{-\mu}(n)\chi(n-\hat{\mu})}{2a} + m\chi(n) \Bigg)\,. \tag{2.44}$$

To remove the effects of the extra fermions, a rooting strategy is performed. This consist of taking the fourth root of the fermion determinant, which is the result of integrating the fermion fields. The reduction of the spinor space made the computations much less expensive.

2.2.4 Finite Temperature and Chemical Potential

At the beginning of this chapter in Section 2.1, the normalization factor in the path integral formalism (Eq. (2.9)) was recognized as the partition function with the same structure than in statistical mechanics, but with the QCD action as a Boltzmann factor.

The partition function in a quantum mechanical canonical ensemble at finite T is

$$Z(T) = \mathrm{Tr}\left[\mathrm{e}^{-\beta\hat{\mathcal{H}}}\right] \tag{2.45}$$

where β here denotes the inverse temperature $\beta = 1/T$, and $\hat{\mathcal{H}}$ the Hamiltonian operator. Following the Matsubara formalism, a Fourier transform is performed in the imaginary time direction, leading to discrete energy levels in term of Matsubara frequencies ω_n with periodicity in the interval $\left(-\frac{\pi}{a}, \frac{\pi}{a}\right]$. For bosons $\omega_n = 2n\pi T$ and the time direction is periodic, while for fermions $\omega_n = (2n+1)\pi T$ and the time direction is anti-periodic.

On the lattice, the partition function depends on the link variables and the fermion fields

$$Z = \int \mathcal{D}[U]\mathcal{D}[\psi]\mathcal{D}[\bar{\psi}]\mathrm{e}^{-S_{\mathrm{QCD}}[U,\psi,\bar{\psi}]} \tag{2.46}$$

with the QCD Euclidian action

$$S_{\mathrm{QCD}}[U,\psi,\bar{\psi}] = \int_0^\beta \mathrm{d}x_4 \int \mathrm{d}^3x \mathcal{L}_{QCD}[U,\psi,\bar{\psi}] \tag{2.47}$$

In Eq. (2.46), at zero temperature the finite integral in the time direction was considered only as a discretization effect. To introduce finite temperature, as done in the Matsubara formalism, the integration in the imaginary time is imposed to be periodic for the gluon fields and anti-periodic for the fermions. The limits of the integration in the imaginary

time are from zero up to the extension of the temporal lattice $\beta = aN_\tau$, by following the analogy

$$\beta = \frac{1}{T} = aN_\tau \,. \tag{2.48}$$

In this equation, a finite β corresponds to a system with finite T. In the $\lim \beta \to \infty$, $T \to 0$. On the other hand, in the continuum limit on the lattice $a \sim \beta \to 0$ will lead to $T \to \infty$. To keep T constant, aN_τ and aN_s have to be constant while taking the continuum limit. This can be done by keeping the ratio $\frac{aN_\tau}{aN_s}$ constant as one approaches the continuum limit.

The inclusion of a baryonic chemical potential μ_B, or a quark chemical potential $\mu_q = \mu_B/3$, is more complicated. In the continuum theory, one has to consider the partition function in the grand canonical ensemble

$$Z(T, \mu_B) = \mathrm{Tr}\left[\mathrm{e}^{-\beta(\hat{\mathcal{H}} - \mu_B \hat{N})}\right] \,; \tag{2.49}$$

this can be done by coupling μ_B with the temporal component of the conserved current $\bar{\psi}(x)\gamma_\mu\psi(x)$. However, adding the term $\mu_B\bar{\psi}(n)\gamma_4\psi(n)$ to the Dirac operator on the lattice leads to an energy density ϵ that diverges in the continuum limit,

$$\lim_{a\to 0}\left[\epsilon(\mu_B) - \epsilon(0)\right] \sim \left(\frac{\mu_B}{a}\right)^2 \tag{2.50}$$

and therefore is not a physical solution. The problem was understood in [69]. The main observation there was that in the continuum Euclidian formalism the chemical potential couples to a conserved charge, and it acts like the imaginary part of the four component of a vector potential. Then, μ_B was introduced as imaginary abelian vector

field on the lattice in a similar way as the link variables

$$\begin{aligned} U_{\hat{4}} &= \mathrm{e}^{\mathrm{i}A_4} \qquad \rightarrow \qquad \mathrm{e}^{a\mu_B} \\ U_{\hat{4}}^{\dagger} &= \mathrm{e}^{-\mathrm{i}A_4} \qquad \rightarrow \qquad \mathrm{e}^{-a\mu_B}\,. \end{aligned} \tag{2.51}$$

The exponential $\mathrm{e}^{\pm a\mu_B}$ was introduced as a multiplying factor on the fourth component of the link variables, so that the Dirac Operator for Wilson Fermions in Eq. (2.39) becomes

$$\begin{aligned} D_W^f(n|m) = &\left(m^f + \frac{4}{a}\right)\delta_{\alpha\beta}\delta_{ab}\delta_{nm} \\ &-\frac{1}{2a}\sum_{\mu=1}^{3}\left[(1-\gamma_\mu)_{\alpha\beta}U_\mu(n)_{ab}\delta_{n+\hat{\mu},m} + (1+\gamma_\mu)_{\alpha\beta}U_{-\mu}(n)_{ab}\delta_{n-\hat{\mu},m}\right] \\ &-\frac{1}{2a}\left[(1-\gamma_4)_{\alpha\beta}\mathrm{e}^{a\mu_B}U_4(n)_{ab}\delta_{n+\hat{4},m} + (1+\gamma_4)_{\alpha\beta}\mathrm{e}^{-a\mu_B}U_{-4}(n)_{ab}\delta_{n-\hat{4},m}\right] \end{aligned} \tag{2.52}$$

at finite μ_B. In this way, the correct energy density is recovered in the continuum limit, and at finite temperature, a closed loop in the time direction will recover the fugacity term: $\left(\mathrm{e}^{a\mu_B}\right)^{N_\tau} = \mathrm{e}^{\mu_B/T}$.

2.2.5 Fermion Determinant

One of the properties of fermions is that they obey Fermi statistics. The anti-commuting relations for fermions are captured by Grassmann numbers. The fermion action in the partition function Eq. (2.46) is quadratic in the fermion fields, and can be integrated analytically, leading to the fermion determinant

$$\begin{aligned} Z &= \int \mathcal{D}[U]\mathrm{e}^{-S_{\mathrm{glu}}[U]}\left(\int \mathcal{D}[\psi]\mathcal{D}[\bar{\psi}]\mathrm{e}^{-\bar{\psi}M\psi}\right) \\ &= \int \mathcal{D}[U]\mathrm{e}^{-S_{\mathrm{glu}}[U]}\det[M]\,. \end{aligned} \tag{2.53}$$

After integration, the partition function depends on the measure $\mathcal{D}[U]$, and the integrand $\rho_M \sim \mathrm{e}^{-S_{\mathrm{glu}}[U]} \det[M]$, which at $\mu = 0$ is positive defined and can be interpreted as probability weight in numerical Monte Carlo simulation. However, introducing a chemical potential the fermion determinant becomes a complex function depending on μ in the following way

$$[\det(\mu)]^* = \det(-\mu^*) \tag{2.54}$$

resulting in a weight ρ_M that is complex for real μ and cannot be used in traditional simulation algorithms. This numerical limitation of the lattice formalism is referred to as the "sign problem". However, the introduction of μ allows one to calculate the expressions for μ-dependent observables, such as susceptibilities of conserved charges that can later be calculated on the lattice at $\mu = 0$. On the other hand, by introducing an imaginary-μ ($\mu \to \mathrm{i}\mu_I$) the fermion determinant stays real, as well as the weight ρ_M. Treating μ as a complex parameter allows one to calculate observables that can be analytical continuations to the real μ-plane. Since the partition function has a matter anti-matter symmetry, $\mathrm{Z}(\mu) = \mathrm{Z}(-\mu)$, the continuations can be done by mapping $\mu_I^2 \to -\mu^2$.

2.3 Imaginary Chemical Potential

QCD at imaginary quark chemical potential $\mu = \mathrm{i}\mu_i$ has an intricate phase structure, whose main characteristics are mentioned in this section. The interplay between the chemical potential and the centre symmetry of the pure gauge sector plays an important role in the structure of this phase diagram. Another aspect to consider is the chiral/deconfinement transition, which is very sensitive to the mass of the quarks. The

Columbia plot, displayed in the right panel of Figure 2.2, shows the order of the transition at $\mu_B = 0$ as a function of the light flavor quark masses. The horizontal axis indicates the mass of the light quarks u and d, while the heavy quark s is shown on the vertical axis. For physical quark masses the transition is a crossover. On the other hand, in the two extremes of the plot: in the vicinity of the chiral limit where the quark masses are zero, and in the limit of infinite quark masses, corresponding to the pure gauge sector, the transition is first order. The dependence of the transition on the quark masses, and also as function of μ_B, is an important aspect to consider and emphasizes the importance of performing calculations with physical quark masses.

The center symmetry of the SU(3) gauge sector on the lattice

$$U_4 \to z^k U_4 \qquad \text{where} \qquad z^k = \mathrm{e}^{\frac{2\pi \mathrm{i} k}{3}} \qquad \text{for:} \quad k = \{0, 1, 3\} \tag{2.55}$$

is broken explicitly with the inclusion of quarks. By including an imaginary quark chemical potential μ_i multiplying the temporal links, the transformation in Eq. (2.55) is modified to

$$\begin{aligned} \mathrm{e}^{\mathrm{i}\frac{\mu_i}{T}} z^k =& \mathrm{e}^{\mathrm{i}\left(\frac{\mu_i}{T} + \frac{2\pi k}{3}\right)} \\ =& \mathrm{e}^{\mathrm{i}\left(\frac{\mu_B^I + 2\pi k}{3T}\right)} \qquad \text{where: } \mu_B = \mathrm{i}\mu_B^I \,. \end{aligned} \tag{2.56}$$

In this equation, a centre symmetry can be undone by a shift in μ_i. This leads to a non-trivial periodicity $\mu_i \to \mu_i + \mathrm{i}2\pi T/3$ known as the Roberge-Weiss symmetry (RW) [70]. The RW is independently of the charge conjugation symmetry $\mu_i \to -\mu_i$, and translates to the imaginary baryonic chemical potential as $\mu_B^I \to \mu_B^I + \mathrm{i}2\pi T$.

The left panel of Figure 2.2 shows the RW periodicity in the imaginary-μ plane. The approximate order parameter of the center symmetry is the Polyakov loop P, which is

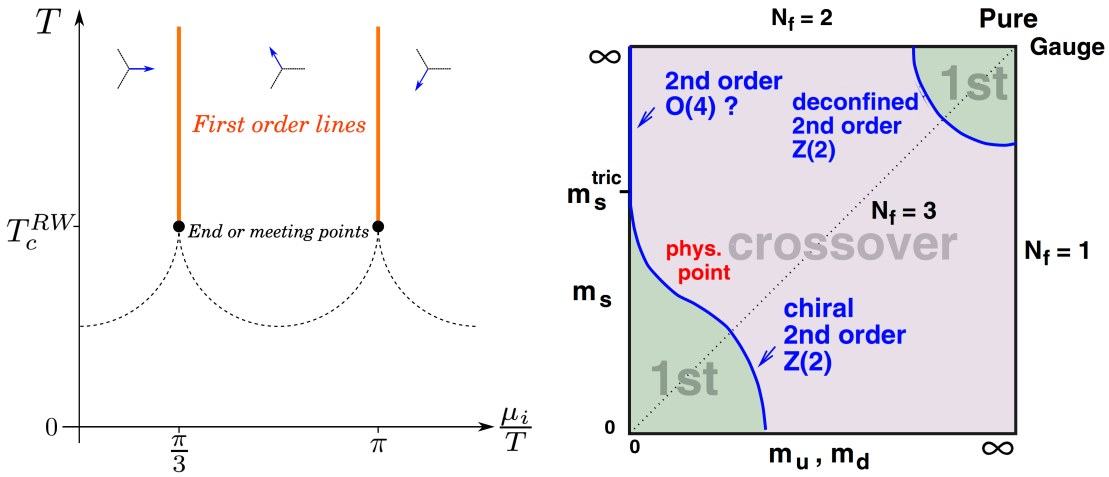

FIGURE 2.2: Left panel: QCD phase diagram in the Imaginary μ plane. The solid lines represent the Roberge-Weiss (RW) first-order phase transitions that terminate on the tricritical points represented by the black dots. The dashed lines signal the chiral/deconfinement transition whose nature depends on the quark masses (figure from [71]). Right panel: the Columbia plot shows the order of the transition as a function of the quark masses at $\mu_i = 0$ (figure form [72])

invariant under a center transformation. In the deconfined phase, $\langle \mathrm{P} \rangle \neq 0$, and as μ_i increases, its expectation value cycles through one of the three different possibilities. The direction of symmetry breaking changes as P rotates, and consequently a 1st-order transition occurs. The direction of P is shown with arrows in this figure. The 1st-order transition is illustrated with solid lines. The dotted lines represent the crossover line where the confined phase with $\langle \mathrm{P} \rangle = 0$ begins. Those two lines meet at the tricritical point, represented by the black dots.

In terms of the baryonic chemical potential, the RW transition occurs at $\mu_B^I = \mathrm{i}\pi T$. The region $\mathrm{i}\pi T \leq \mu_B^2 \leq 0$ that can be explored on the lattice to find the μ-dependence of the observables. For instance, recent simulations at imaginary-μ have been dedicated to determine the transition line in the $T - \mu_B^2$ phase diagram and, using analyticity arguments, continue the transition to the real $T - \mu_B$ plane [73–75]. In [76], the QCD

EoS has been explored and extrapolated from imaginary-μ_B, and in [77] the low order susceptibilities at imaginary-μ were used to calculate generalized quark number susceptibilities. In this dissertation, the lower order baryon susceptibilities at imaginary-μ_B were analyzed to determine the higher order susceptibilities that are discussed in Chapter 3 and were published in [23].

2.4 Susceptibilities of Conserved Charges

The susceptibilities of conserved charges are important thermodynamic quantities that can be calculated on the lattice and are related to the moments of the distribution of conserved charges measured in HICs, as it was shown in Section 1.3.4. The phenomenological conserved charges that are interesting in the context of HICs are baryon number (B), electric charge (Q) and strangeness (S), which are fixed during the entire collision. In QCD there is a conserved charge for each quark flavor (μ_u, μ_d, μ_s). The relations between the chemical potentials of quarks and those of the conserved charges are

$$\begin{aligned} \mu_u &= \frac{1}{3}\mu_B + \frac{2}{3}\mu_Q \\ \mu_d &= \frac{1}{3}\mu_B - \frac{1}{3}\mu_Q \\ \mu_s &= \frac{1}{3}\mu_B - \frac{1}{3}\mu_Q - \mu_S \,. \end{aligned} \tag{2.57}$$

The susceptibilities are the derivatives of the free energy with respect to the chemical potentials. Since the free energy is proportional to the pressure, the susceptibilities can be defined as

$$\chi^{B,Q,S}_{i,j,k} = \frac{\partial^{i+j+k}(\hat{p})}{(\partial\hat{\mu_B})^i(\partial\hat{\mu_Q})^j(\partial\hat{\mu_S})^k} \tag{2.58}$$

with the dimensionless variables

$$\hat{p} = \frac{p}{T^4} \qquad \hat{\mu}_i = \frac{\mu_i}{T}. \tag{2.59}$$

An additional chemical potential relevant in the study of HIC is the light isospin, defined as

$$\mu_I = \mu_u - \mu_d \,. \tag{2.60}$$

Here, some useful relations of susceptibilities that are calculated on the lattice, and can be related to observables in HICs are shown. Simplifications of these expressions occur by assuming $\mu_B = 0$ and degenerate u and d quarks [78, 79]. The susceptibilities of the conserved charges are expressed in terms of the quark derivatives. The second order combinations in B, Q, S are given by

$$\begin{aligned}
\chi_2^B &= \frac{1}{9}\left[2\chi_2^u + \chi_2^s + 4\chi_{11}^{us} + 2\chi_{11}^{ud}\right] & \chi_2^I &= \frac{1}{2}\left[\chi_2^u - \chi_{11}^{ud}\right] \\
\chi_2^Q &= \frac{1}{9}\left[5\chi_2^u + \chi_2^s - 2\chi_{11}^{us} - 4\chi_{11}^{ud}\right] & \chi_{11}^{BS} &= -\frac{1}{3}\left[\chi_2^s + 2\chi_{11}^{us}\right] \\
\chi_{11}^{BQ} &= \frac{1}{9}\left[\chi_2^u - \chi_2^s - \chi_{11}^{us} + \chi_{11}^{ud}\right] & \chi_{11}^{QS} &= \frac{1}{3}\left[\chi_2^s - \chi_{11}^{us}\right] \,,
\end{aligned} \tag{2.61}$$

while the fourth order diagonal baryon and electric susceptibilities, related to the kurtosis in Eq.(1.23), are

$$\begin{aligned}
\chi_4^B &= \frac{1}{81}\left[2\chi_4^u + \chi_4^s + 6\chi_{22}^{ud} + 12\chi_{22}^{us} + 8\chi_{13}^{us} + 8\chi_{31}^{us} + 8\chi_{31}^{ud} + 24\chi_{211}^{uds} + 12\chi_{112}^{uds}\right] \\
\chi_4^Q &= \frac{1}{81}\left[17\chi_4^u + \chi_4^s + 24\chi_{22}^{ud} + 30\chi_{22}^{us} - 4\chi_{13}^{us} - 28\chi_{31}^{us} - 40\chi_{31}^{ud} + 24\chi_{211}^{uds} - 24\chi_{112}^{uds}\right] \,.
\end{aligned} \tag{2.62}$$

Up to forth order combination of susceptibilities are needed to perform the calculations in Chapter 3. The next section shows the expression for the partial derivatives of the

susceptibilities in terms of the fermionic determinant that is calculated on the lattice.

2.4.1 Susceptibilities on the Lattice

The expressions needed to compute susceptibilities on the lattice at $\mu_B = 0$ are derivatives in terms of the fermion determinant. The QCD partition function, after integrating the fermionic degrees of freedom, is given by

$$Z = \int \mathcal{D}[U] e^{-S_{\rm glu}[U]} (\det M_u)^{1/4} (\det M_d)^{1/4} (\det M_s)^{1/4} (\det M_c)^{1/4} \tag{2.63}$$

where S_g is the gauge action and M_i is the fermionic determinant of the quark of flavor i. The derivative of the fermion matrix M is expressed as

$$\frac{dM}{d\mu}\psi(x) = \frac{1}{2}\eta_4(x)\left[U_4(x)\psi(x+\hat{4}) + U_4^+(x-\hat{0})\psi(x-\hat{4})\right],$$
$$\frac{d^2M}{d\mu^2}\psi(x) = \frac{1}{2}\eta_0(x)\left[U_4(x)\psi(x+\hat{4}) - U_4^+(x-\hat{0})\psi(x-\hat{4})\right];$$

any higher odd and even derivative are equal to $dM/d\mu$ and $d^2M/d\mu^2$, respectively. The derivatives of the fermionic determinant det M are expressed as traces of the fermion matrix M_j. The terms needed to calculate up to the forth-order susceptibility are given

by the following expressions

$$\begin{aligned}
\frac{d}{d\mu_j}\log(\det M_j)^{1/4} &= \frac{1}{4}\mathrm{tr}\left[M_j^{-1}M_j'\right] \\
\frac{d^2}{(d\mu_j)^2}\log(\det M_j)^{1/4} &= \frac{1}{4}\mathrm{tr}\left[(M_j''M_j^{-1} - M_j'M_j^{-1}M_j'M_j^{-1}\right] \\
\frac{d^3}{(d\mu_j)^3}\log(\det M_j)^{1/4} &= \frac{1}{4}\mathrm{tr}\left[M_j'M_j^{-1} - 3M_j''M_j^{-1}M_j'M_j^{-1} + 2M_j'M_j^{-1}M_j'M_j^{-1}M_j'M_j^{-1}\right] \\
\frac{d^4}{(d\mu_j)^4}\log(\det M_j)^{1/4} &= \frac{1}{4}\mathrm{tr}\left[(M_j''M_j^{-1} - 4M_j'M_j^{-1}M_j'M_j^{-1} - 3M_j''M_j^{-1}M_j''M_j^{-1}\right. \\
&\quad \left. +12M_j''M_j^{-1}M_j'M_j^{-1}M_j'M_j^{-1} - 6M_j'M_j^{-1}M_j'M_j^{-1}M_j'M_j^{-1}M_j'M_j^{-1}\right] \qquad (2.64)
\end{aligned}$$

by using the notation

$$\begin{aligned}
\langle A_i\rangle &= \partial_i \log Z\,. & \langle B_i\rangle &= \partial_i^2 \log Z\,. \\
\langle C_i\rangle &= \partial_i^3 \log Z\,. & \langle D_i\rangle &= \partial_i^4 \log Z\,. \qquad (2.65)
\end{aligned}$$

the derivative of the expectation value of any lattice observable X is obtained as

$$\partial_j \langle X\rangle = \langle XA_j\rangle - \langle X\rangle\langle A_j\rangle + \langle \partial_j X\rangle\ . \qquad (2.66)$$

the higher order formulas are obtained by using Eq. 2.66, recursively, and setting $\mu = 0$ at the end of the calculation. The analytical calculations to obtain up to the fourth order expressions on the susceptibilities requires extensive analytical work. For example,

expressions for high order diagonal derivatives

$$\begin{aligned}
\partial_i^2 \log Z &= \left\langle A_i^2 \right\rangle - \left\langle A_i \right\rangle^2 + \left\langle B_i \right\rangle \\
\partial_i^4 \log Z &= \left\langle A_i^4 \right\rangle - 3 \left\langle A_i^2 \right\rangle^2 + 3 \left(\left\langle B_i^2 \right\rangle - \left\langle B_i \right\rangle^2 \right) \\
&\quad + 6 \left(\left\langle A_i^2 B_i \right\rangle - \left\langle A_i^2 \right\rangle \left\langle B_i \right\rangle \right) + 4 \left\langle A_i C_i \right\rangle + \left\langle D_i \right\rangle \ , \qquad (2.67)
\end{aligned}$$

and for non-diagonal derivatives

$$\begin{aligned}
\partial_u^2 \partial_d^2 \log Z &= \left\langle A_u^4 \right\rangle - 3 \left\langle A_u^2 \right\rangle^2 + \left\langle B_u^2 \right\rangle - \left\langle B_u \right\rangle^2 + 2 \left(\left\langle A_i^2 B_i \right\rangle - \left\langle A_i^2 \right\rangle \left\langle B_i \right\rangle \right) \\
\partial_u \partial_s^3 \log Z &= \left\langle A_u A_s^3 \right\rangle - 3 \left\langle A_s^2 \right\rangle \left\langle A_u A_s \right\rangle + 3 \left(\left\langle A_u A_s B_s \right\rangle - \left\langle A_u A_s \right\rangle \left\langle B_s \right\rangle \right) + \left\langle A_u C_s \right\rangle \\
\partial_u^2 \partial_s^2 \log Z &= \left\langle A_u^2 A_s^2 \right\rangle - 2 \left\langle A_u A_s \right\rangle^2 - \left\langle A_u^2 \right\rangle \left\langle A_s^2 \right\rangle + \left\langle B_u B_s \right\rangle - \left\langle B_u \right\rangle \left\langle B_s \right\rangle + \left\langle A_u^2 B_s \right\rangle \\
&\quad - \left\langle A_u^2 \right\rangle \left\langle B_s \right\rangle + \left\langle A_s^2 B_u \right\rangle - \left\langle A_s^2 \right\rangle \left\langle B_u \right\rangle \\
\partial_u \partial_d \partial_s^2 \log Z &= \left\langle A_u^2 A_s^2 \right\rangle - 2 \left\langle A_u A_s \right\rangle^2 - \left\langle A_u^2 \right\rangle \left\langle A_s^2 \right\rangle + \left\langle A_u^2 B_s \right\rangle - \left\langle A_u^2 \right\rangle \left\langle B_s \right\rangle \ . \qquad (2.68)
\end{aligned}$$

Everyone of those expectation values can be calculated on the lattice at $\mu = 0$, and from them construct the corresponding combination of susceptibilities.

Chapter 3

Higher Order Susceptibilities from the Lattice

The direct calculation of susceptibilities at $\mu_B = 0$ is affected by a signal-to-noise ratio with an exponent that grows with the order of the susceptibility, and consequently the uncertainty on the higher order ones, such as χ_6, is at the moment large [20]. An alternative strategy to improve the calculation of higher order susceptibilities is to calculate the lower order ones at imaginary-μ_B with great precision [23, 80]. Then, one can take the results of the simulations to the real plane $(\mathrm{i}\mu_B^I)^2 \to \mu_B^2$ and extract the higher order susceptibilities at $\mu_B = 0$, using the method described below.

The topic of this chapter is precisely to analyze the lower order susceptibilities (χ_1, χ_2, χ_3, and χ_4) computed at imaginary-μ_B and perform their combined fit to extract higher order ones at $\mu_B = 0$ (χ_6 and χ_8).

3.1 Lattice Setup

The action used to calculate the lower order susceptibilities is a tree-level Symanzik improved gauge action, with four times stout smearing and smearing parameter $\rho = 0.125$ [81].

It simulates $2+1+1$ dynamical quarks [23, 80]

$$Z = \int \mathcal{D}[U] e^{-S_{glu}[U]} (\det M_u)^{1/4} (\det M_d)^{1/4} (\det M_s)^{1/4} (\det M_c)^{1/4} \tag{3.1}$$

The analysis was done on a lattice with $N_S = 48$ and $N_\tau = 12$. The light flavors, u and d quarks, are considered degenerate, and are tuned in a way to reproduce the physical pion and kaon masses. The charm mass is introduced by the continuum extrapolated quark mass ratio $\frac{m_c}{m_s} = 11.85$ of [82]. The light and strange quark masses are obtained by tuning the following ratios to their physical values:

$$R_S^{phys} = \frac{2m_K^2 - m_\pi^2}{f_\pi^2} = 27.65 \qquad R_L^{phys} = \frac{m_\pi}{f_\pi} = 1.069\,, \tag{3.2}$$

where isospin-averaged pion (π) and kaon (K) masses were used [83]. The scale was determined by setting $f_\pi = 130.41$ MeV [84]. The ratio μ_B/T is denoted in this chapter for simplicity with a hat as $\hat{\mu}_B$.

3.1.1 Lattice Data

The lower order susceptibilities (χ_1, χ_2, χ_3, and χ_4) are obtained using the expressions shown in Section 2.4 at imaginary-μ_B. In terms of quark chemical potentials, the ensembles were generated with $\mu_u = \mu_d = \mu_s = \mu_B/3$ in the temperature range $T = \{135, 140, \ldots, 220\}$ MeV. At each temperature, eight values of imaginary μ_B are obtained at the points $\hat{\mu_B}^{(j)} = i\frac{j\pi}{8}$ for $j = \{0, 1, 2, 3, 4, 5, 6, 7\}$. From all the generated configurations, $N = 48$ Jackknife estimators are obtained for each lattice point. The Jackknife estimators (x_i) are used to calculate the mean ($\bar{x}$) and the variance (σ^2)

$$\bar{x} = \frac{1}{N}\sum_{i=1}^{N} x_i \qquad \sigma^2 = \frac{N-1}{N}\sum (x_i - \bar{x})^2 \tag{3.3}$$

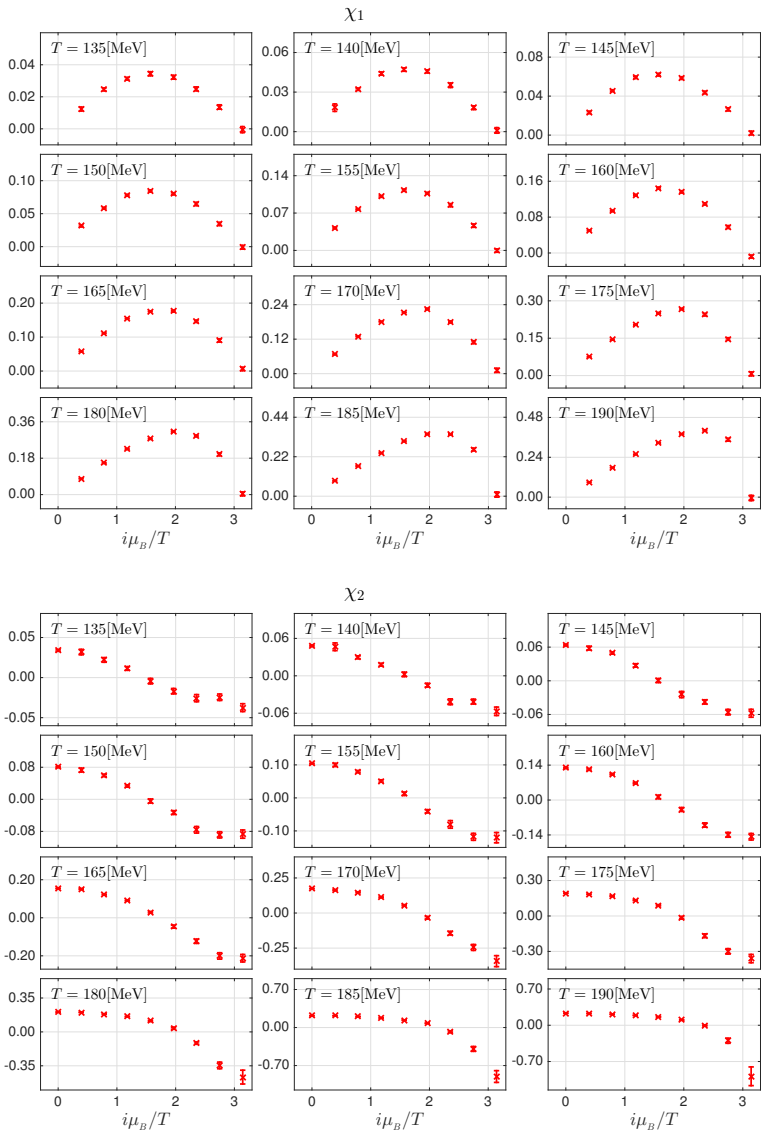

FIGURE 3.1: Lower order susceptibilities in the imaginary-μ_B plane as functions of $\hat{\mu_B} = \mu_B/T$ for different temperatures, T.
Upper panel: $\chi_1(\mathrm{i}\hat{\mu_B})$. Lower panel: $\chi_2(\mathrm{i}\hat{\mu_B})$.

on each lattice point. The lattice points simulated in the imaginary-$\hat{\mu_B}$ plane are shown in Figure 3.1, and Figure 3.2.

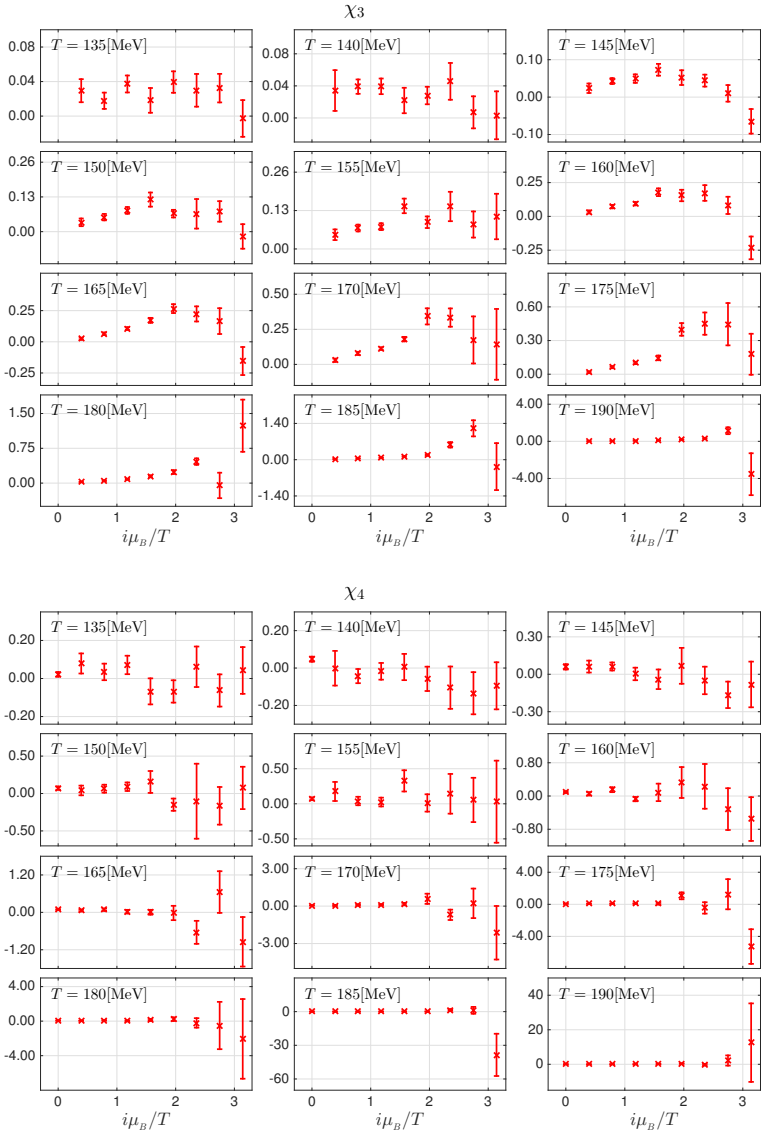

FIGURE 3.2: Lower order susceptibilities in the imaginary-μ_B plane as functions of $\hat{\mu}_B = \mu_B/T$ for different temperatures, T.
Upper panel: $\chi_3(\mathrm{i}\hat{\mu}_B)$. Lower panel: $\chi_4(\mathrm{i}\hat{\mu}_B)$.

3.2 Combined Fit Part 1

The main goal of this section is to calculate $\chi_2^B(T)$, $\chi_4^B(T)$, $\chi_6^B(T)$, and $\chi_8^B(T)$ at $\mu_B = 0$ by performing a combined fit of the susceptibilities $\chi_1^B(T)$, $\chi_2^B(T)$, $\chi_3^B(T)$ and $\chi_4^B(T)$ from

simulations at imaginary-μ_B. Note that only $\chi_2^B(T)$ and $\chi_4^B(T)$ can be determined from simulations at $\mu_B = 0$, since $\chi_1^B(T)$ and $\chi_3^B(T)$ are odd functions of μ_B and they vanish because of matter antimatter symmetry.

All the lattice points are shown in Figure 3.1, and Figure 3.2. The fit was performed at a fixed temperature T. In this way, the results for different temperatures are obtained completely independently. Thus, the error bars in the results will be independent. On the other hand, the errors between the quantities $\chi_2^B(T)$, $\chi_4^B(T)$, χ_6^B(T), and $\chi_8 T)$ will be highly correlated since these are extracted through the same set of ensembles at a given temperature.

In this section, the ansatz for the pressure (χ_0^B) is a Taylor expansion in terms of $\hat{\mu_B}^2$ up to $\hat{\mu_B}^{10}$

$$\chi_0^B(\hat{\mu_B}) = c_0 + c_2\hat{\mu_B}^2 + c_4\hat{\mu_B}^4 + c_6\hat{\mu_B}^6 + c_8\hat{\mu_B}^8 + c_{10}\hat{\mu_B}^{10}, \tag{3.4}$$

from which expressions depending only on μ_B^2 for the susceptibilities can be obtained as follows:

$$\frac{\chi_1^B(\hat{\mu_B}^2)}{\hat{\mu_B}} = 2c_2 + 4c_4\hat{\mu_B}^2 + 6c_6\hat{\mu_B}^4 + 8c_8\epsilon_1\hat{\mu_B}^6 + 10c_{10}\hat{\mu_B}^8 \tag{3.5}$$

$$\chi_2^B(\hat{\mu_B}^2) = 2c_2 + 12c_4\hat{\mu_B}^2 + 30c_6\hat{\mu_B}^4 + 56c_8\hat{\mu_B}^6 + 90c_{10}\hat{\mu_B}^8 \tag{3.6}$$

$$\frac{\chi_3^B(\hat{\mu_B}^2)}{\hat{\mu_B}} = 24c_4 + 120c_6\hat{\mu_B}^2 + 336c_8\hat{\mu_B}^4 + 720c_{10}\hat{\mu_B}^6 \tag{3.7}$$

$$\chi_4^B(\hat{\mu_B}^2) = 24c_4 + 360c_6\hat{\mu_B}^2 + 1680c_8\hat{\mu_B}^4 + 5040c_{10}\hat{\mu_B}^6\,. \tag{3.8}$$

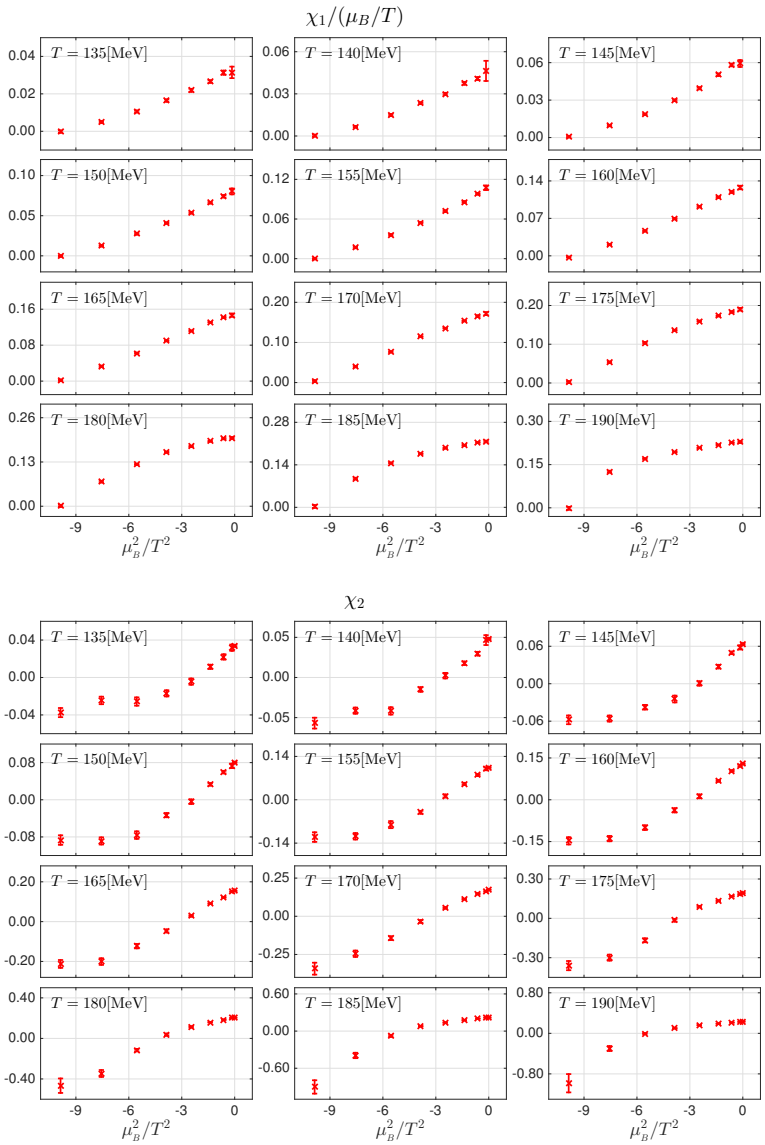

FIGURE 3.3: Lower order susceptibilities calculated on the lattice at imaginary-μ_B as a function of $\hat{\mu_B}^2 = \mu_B^2/T^2$ for different temperatures, T. Upper panel: $\chi_1^B(\hat{\mu_B}^2)/(\hat{\mu_B})$. Lower panel: $\chi_2^B(\hat{\mu_B}^2)$.

The baryonic susceptibilities at $\mu_B = 0$ are related to the Taylor coefficients in Eq. (3.4) by the following relations

$$\chi_2^B = 2!c_2 \qquad \chi_4^B = 4!c_4 \qquad \chi_6^B = 6!c_6 \qquad \chi_8^B = 8!c_8\,. \tag{3.9}$$

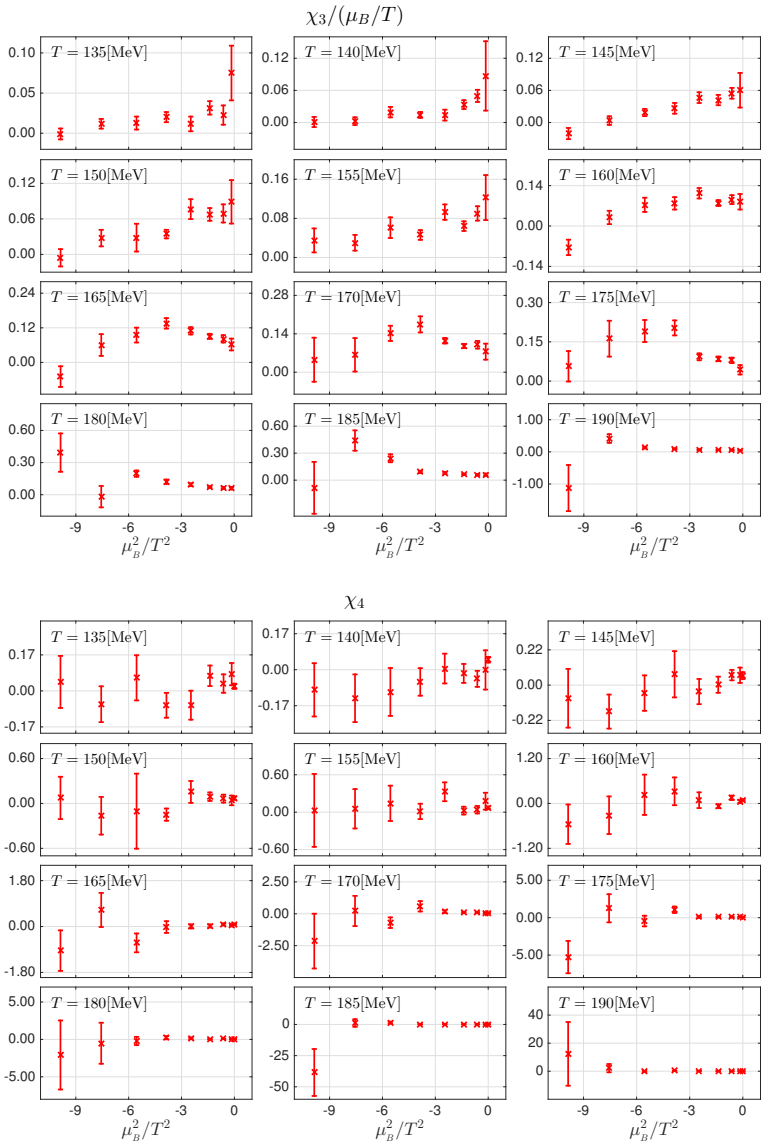

FIGURE 3.4: Lower order susceptibilities calculated on the lattice at imaginary-μ_B as a function of $\hat{\mu_B}^2 = \mu_B^2/T^2$ for different temperatures, T. Upper panel: $\chi_3^B(\hat{\mu_B}^2)/\hat{\mu_B}$. Lower panel: $\chi_4^B(\hat{\mu_B}^2)$.

The lattice points in the μ_B^2 plane for the expressions in Eqs. (3.5-3.8) are shown in Figure 3.3 and Figure 3.4. There are 34 lattice point in total for each Jackknife estimator, and 48 estimators for each temperature T. The combined fit is done by performing

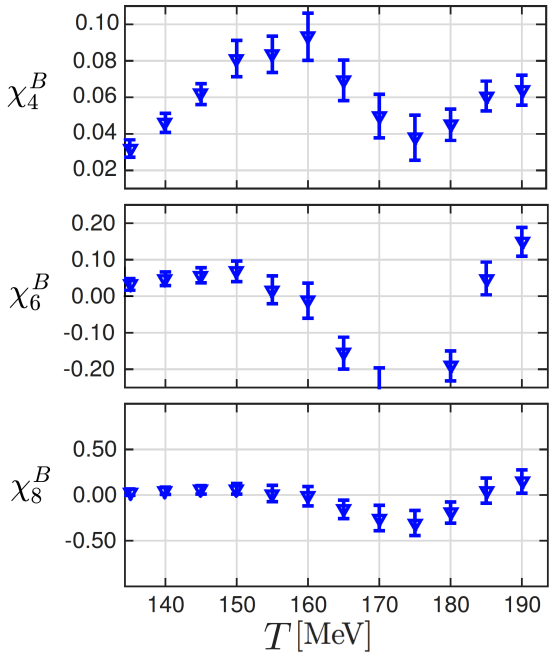

FIGURE 3.5: Results for χ_4^B, χ_6^B and χ_8^B as functions of the temperature T using the ansatz in Eq. (3.4).

a linear least square (LLS) fitting of each Jackknife estimator and then computing the mean and standard deviation in order to obtain a point with its respective error bar. Some of the lattice points in Figure 3.3 and Figure 3.4 show big error bars. To reduce the negative effect of those points, a combination of up to three points on each of the quantities in Eqs. (3.5-3.8) were omitted in order to find the combined fit with smaller error bars on χ_6 and χ_8.. The results of the best fit are shown in Figure 3.5. χ_4 has been calculated by direct method on the lattice at $\mu_B = 0$, and it is known to have a smooth dependence as a function of T. Our result shows that the combined fit done with the ansatz in Eq. (3.4) is not stable.

The HRG model predicts that for temperatures, T, smaller that the transition temperature, T_c, the functional form of the baryon density $\rho_B \sim \sinh(\hat{\mu_B})$, which translate

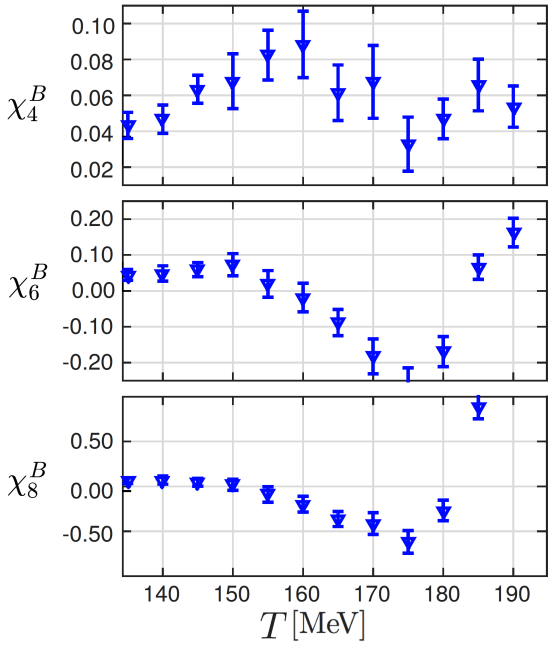

FIGURE 3.6: Results for χ_4^B, χ_6^B and χ_8^B as functions of the temperature T using the ansatz in Eq. (3.10).

at the imaginary-μ_B plane as $\rho_B \sim \sin(\mu_B^I)$. The fact that the baryon density ρ_B is proportional to χ_1^B motivates to add a $\cos(\hat{\mu}_B)$ to Eq. (3.4) to produce a $\chi_1^B \sim \sinh(\hat{\mu}_B)$. The second ansatz for the pressure that is consider is given by

$$\chi_0^B(\hat{\mu}_B) = c_0 + c_2\hat{\mu}_B^2 + c_4\hat{\mu}_B^4 + c_6\hat{\mu}_B^6 + c_8\hat{\mu}_B^8 + c_{10}\hat{\mu}_B^{10} + c_c\cos(\hat{\mu}_B)\,. \tag{3.10}$$

The results of the combined fit using Eq. (3.10) are shown in Figure 3.6. One more time, the fitting of χ_4 is shown to be not smooth. Later, different approaches to try to get a better quality for the results were used such as Fourier series, T-dependent 2D fitting with polynomial, cubic splines, and thin-plate splines. However, the results were similar to the ones already shown in Figure 3.5, and Figure 3.6.

3.3 Expected Results for χ_8^B

The results obtained in Section 3.2 can be improved if one has an intuition of the expectations for the higher order susceptibilities that help to constrain the parameters in the calculation. The aim is to create a toy model able to calculate up to χ_8 from known features of the susceptibilities that are available.

The first and second baryon susceptibilities are related at $\mu_B \simeq 0$ by the ratio

$$\left.\frac{\chi_1^B(T,\hat{\mu}_B)}{\hat{\mu}_B}\right|_{\hat{\mu}_B \simeq 0} \simeq \chi_2^B(T,0)\,; \tag{3.11}$$

therefore, at very small chemical potential $\chi_1^B(T,\mu_B) \simeq \chi_2^B(T,0)\hat{\mu}_B$. The ratio $\chi_1^B(T,\hat{\mu}_B)/\hat{\mu}_B$ can be calculated for an imaginary value of μ_B while $\chi_2^B(T,0)$ has been calculated by direct method. The left panel in Figure 3.7 shows lattice points for $\chi_2^B(T,0)$ (purple points), and also shows the calculation of $\chi_1^B(T,\hat{\mu}_B)/\hat{\mu}_B$ for $\hat{\mu}_B = \mathrm{i}5\pi/8$ (yellow points). The qualitative behavior is similar for both set of points, but the latter are shifted to higher values. The figure also shows, with a yellow curve, the interpolation obtained for $\chi_2^B(T,0)$ using the simple fit function form

$$\chi_2^B(T,0) \simeq A + BT + C\,\mathrm{atan}(D(T-E)) \tag{3.12}$$

this function reproduces the gross features of the curve in the $T = \{120:300\}$ MeV interval.

On the other hand, the dependence of the transition temperature T_c at $\mu_B = 0$ is known to decrease for small values of $\hat{\mu}_B$, tracing a parabola in the phase diagram with positive curvature κ [73–75, 85]

$$T_c = T\left[1 - \kappa{\hat{\mu}_B}^2 + \mathcal{O}\left({\hat{\mu}_B}^4\right)\right] \tag{3.13}$$

Taking this into account, the approximation in Eq. (3.11) can be improved (at least close to the transition temperature where high order susceptibilities have more structure) by rescaling the T-dependence in Eq. (3.13) by T_c giving the following relation

$$\begin{aligned}\chi_1^{B(\text{toy})}(T,\hat{\mu}_B) &= \hat{\mu}_B \chi_2^B\left(T(1+\kappa\hat{\mu}_B{}^2)\right) \\ &= \hat{\mu}_B\left[A + B\,T(1+\kappa\hat{\mu}_B{}^2) + C\,\text{atan}(D(T(1+\kappa\hat{\mu}_B^2)-E))\right] \end{aligned} \tag{3.14}$$

with both dependence on T and $\hat{\mu}_B$. This toy model was able to reproduce the behavior of the lattices points calculated at $\hat{\mu}_B = \text{i}5\pi/8$ as is shown in Figure 3.7 with a purple curve. The curve is essentially similar to the one parametrized by Eq. (3.12), but its inflection point has been shifted to higher temperatures, as a consequence of a positive curvature of the parameter κ.

The approximation given by the toy model in Eq. (3.14) gives access to the μ_B dependence at any temperature. Although the toy model only incorporates the feature of a smooth χ_2^B and the shifting of T_c with the chemical potential, it correctly reproduces the oscillatory pattern of the higher order susceptibilities.

On the right panel in Figure 3.7, the ratio χ_8^B/χ_4^B is shown to motivate a prior strategy to stabilize the combined fitting that was done in Section 3.2. This ratio is equal to one in the HRG model, while at high temperatures higher order fluctuations quickly approach the Stefan-Boltzmann limit as it was seen in HTL perturbation theory [86, 87] as well as on the lattice [80, 88]. The Stefan-Boltzmann limit is zero for χ_{2n}^B if $n \geq 3$. There is no reason to expect the toy model to work at high temperatures and it actually converges to zero slower than the HTL prediction. However, deviations from the HRG model predictions are expected, which would correspond to a signal from a nearby CEP. The pattern of χ_8^B/χ_4^B in the toy model is slightly asymmetric. The dark and light bands in the figure correspond to one and two σ regions of the prior distribution. This

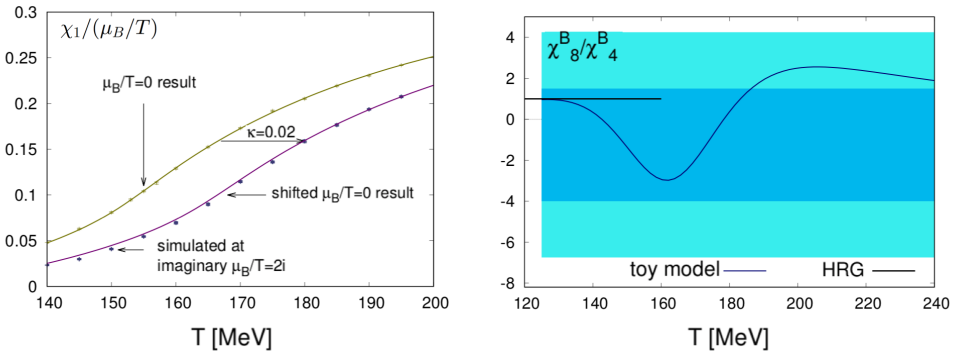

FIGURE 3.7: Left panel: shows lattice calculations for χ_2^B at $\hat{\mu_B} = 0$ (purple points), and the ratio $\chi_1^B/\hat{\mu_B}$ calculated at $\hat{\mu_B} = i5\pi/8$ (yellow points). The yellow curve represents the parametrization in Eq. (3.12) for χ_2^B at $\hat{\mu_B} = 0$ (purple points). The purple curve is obtained from the toy model in Eq. (3.14), which has an excellent agreement with the shifted lattice points (yellow points). Right panel: the toy model results for the ratio χ_8^B/χ_4^B is shown as a blue curve (the HRG prediction is represented by a black line). The dark and light bands corresponds to one and two σ regions of the prior distribution.

fact motivates to define a prior relation between χ_8^B and χ_4^B giving by

$$\chi_8^B = \chi_4^B\,(-1.25 + 2.75\xi) \tag{3.15}$$

where ξ is a stochastic variable with normal distribution.

3.4 Combined Fit Part 2

Our data did not allow for an independent determination of c_8 and c_{10} in Section 3.2. Nevertheless, in order to have some control over these, guided by the toy model described in Section 3.3, one can impose some assumption on the higher order terms. In

particular, the relation in Eq. (3.16) is imposed in the following way

$$\frac{\chi_8^B}{\chi_4^B} = \frac{8! c_8}{4! c_4} = \epsilon_1 \tag{3.16}$$

where ϵ_1 is a stochastic variable. For simplicity, a similar relation is also imposed for χ_{10}^B

$$\frac{\chi_{10}^B}{\chi_4^B} = \frac{10! c_{10}}{4! c_4} = \epsilon_2 \,. \tag{3.17}$$

Note that, without this term, the statistical errors on χ_8^B are smaller, but the fit would be less controlled. As the highest order in the expansion, the resulting χ_8^B probably contains contamination from higher order terms.

The ansatz in Eq. (3.4) is rewriting with as

$$\chi_0^B(\hat{\mu_B}) = c_0 + c_2 \hat{\mu_B}^2 + c_4 \hat{\mu_B}^4 + c_6 \hat{\mu_B}^6 + \frac{4!}{8!} c_4 \epsilon_1 \hat{\mu_B}^8 + \frac{4!}{10!} c_4 \epsilon_2 \hat{\mu_B}^{10}, \tag{3.18}$$

where ϵ_1 and ϵ_2 are drawn randomly from a normal distribution with mean -1.25 and variance 2.75. The coefficients c_8 and c_{10} become stochastic variables. The used distribution for $\epsilon_{1,2}$ implements a prior for χ_8^B and χ_{10}^B.

For the ansatz in Eq. (3.18), the following derivatives are obtained

$$\chi_1^B(\hat{\mu_B}) = 2c_2 \hat{\mu_B} + 4c_4 \hat{\mu_B}^3 + 6c_6 \hat{\mu_B}^5 + \frac{4!}{7!} c_4 \epsilon_1 \hat{\mu_B}^7 + \frac{4!}{9!} c_4 \epsilon_2 \hat{\mu_B}^9 \tag{3.19}$$

$$\chi_2^B(\hat{\mu_B}) = 2c_2 + 12c_4 \hat{\mu_B}^2 + 30c_6 \hat{\mu_B}^4 + \frac{4!}{6!} c_4 \epsilon_1 \hat{\mu_B}^6 + \frac{4!}{8!} c_4 \epsilon_2 \hat{\mu_B}^8 \tag{3.20}$$

$$\chi_3^B(\hat{\mu_B}) = 24c_4 \hat{\mu_B} + 120c_6 \hat{\mu_B}^3 + \frac{4!}{5!} c_4 \epsilon_1 \hat{\mu_B}^5 + \frac{4!}{7!} c_4 \epsilon_2 \hat{\mu_B}^7 \tag{3.21}$$

$$\chi_4^B(\hat{\mu_B}) = 24c_4 + 360c_6 \hat{\mu_B}^2 + c_4 \epsilon_1 \hat{\mu_B}^4 + \frac{4!}{6!} c_4 \epsilon_2 \hat{\mu_B}^6 \,. \tag{3.22}$$

Using Eqs. (3.19-3.22), a correlated fit is performed for the four measured observables,

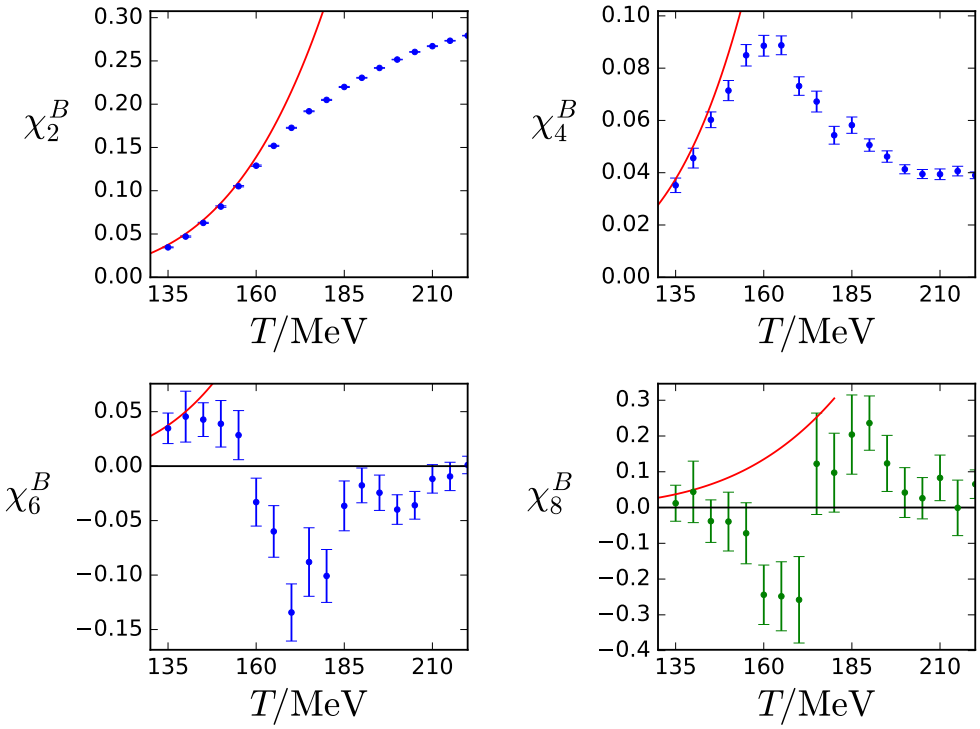

FIGURE 3.8: Results for χ_2^B, χ_4^B, χ_6^B and an estimate for χ_8^B as functions of the temperature T obtained from the single-temperature analysis. The red curves are calculation made with the HRG model.

obtaining the values of c_2, c_4 and c_6 for each temperature, and the corresponding χ_2^B, χ_4^B and χ_6^B. The fit is repeated for 1000 random draws for ϵ_1 and ϵ_2. Through these weights we get a posterior distribution from the prior one. The final estimate for χ_8^B represents this posterior distribution. The results for χ_{10}^B are not shown since this term becomes mostly noise.

Finally, the results of the analysis ffor $\chi_2^B(T)$, $\chi_4^B(T)$ and $\chi_6^B(T)$ are shown in Figure 3.8 together with an estimate of χ_8^B, related to χ_4^B by Eq. (3.16). The results are very smooth, with small error bars for χ_2^B, χ_4^B, while χ_6^B and the estimate for χ_8^B show the trend expected from universality arguments [39].

Chapter 4

Holographic Model

This chapter describes the holographic black hole model used in this dissertation to study the strongly interacting region of the QCD phase diagram. The construction is a bottom-up dilatonic dual model based on the coupling between the bulk metric field $g_{\mu\nu}$, a real scalar dilaton field ϕ, and a Maxwell vector field A_μ defining an Einstein-Maxwell-dilaton (EMD) model. The EMD model was originally introduced in [89], and has only as free parameters: the gravitational constant κ_5^2, an energy scale Λ, and two functions of the dilaton field. One of these functions is the dilaton-scalar potential $V(\phi)$ and the other one is the Maxwell-dilaton coupling $f(\phi)$. In Section 4.1, the EMD model is defined and the equations of motion are written. Then, the numerical sett-up is described in Section 4.2, and the engineering of the black holes to mimic QCD is described in Section 4.3.

4.1 EMD Black Hole Model

This section describes the EMD holographic model used in this dissertation. In the EMD model, the effects due to a nonzero baryon chemical potential μ_B one taken into account by the zero component of a Maxwell field A_μ. The EMD model action is given

by [89]

$$S = \frac{1}{2\kappa_5^2}\int \mathrm{d}^5x\,\sqrt{-g}\left[\mathcal{R} - \frac{1}{2}(\partial_\mu\phi)^2 - V(\phi) - \frac{1}{4}f(\phi)F_{\mu\nu}^2\right], \tag{4.1}$$

where $\kappa_5^2 \equiv 8\pi G_5$ is Newton's constant in five spacetime dimensions, $\mathcal{R}$ is the Ricci scalar, ϕ is a dilaton field which couples to the metric $g_{\mu\nu}$ trough the potential $V(\phi)$, the Maxwell field is introduced in the field tensor $F_{\mu\nu} = \partial_\mu A_\nu - \partial_\nu A_\mu$, and $f(\phi)$ is the Maxwell-dilaton coupling. The action in Eq. (4.1) is complemented by some boundary terms which affect the evaluation of the free energy, but not the equations of motion or the calculation of the entropy or temperature.

The EMD model becomes completely specified by fixing only two parameters and two functions. The dilaton potential $V(\phi)$ is a free function responsible of breaking the conformal symmetry of the theory in the infrared regime, emulating the effects of a dynamically generated Λ_{QCD} scale, and it will determine the behavior of the thermodynamics at $\mu_B = 0$. The Maxwell-dilaton coupling $f(\phi)$ is a free function that will define the response of the system to a finite μ_B. The other two free parameters are the gravitational constant κ_5^2 and a characteristic energy scale, Λ. The energy scale Λ is used to convert physical observables, calculated on the gravity side in terms of inverse powers of the AdS radius L, to physical units expressed in powers of MeV.

A general metric for charged black hole backgrounds, spatially isotropic and translationally invariant, is described by the ansatz

$$ds^2 = e^{2A(r)}\left[-h(r)dt^2 + d\vec{x}^2\right] + \frac{e^{2B(r)}dr^2}{h(r)} \tag{4.2}$$

where the field depends only on r as

$$\phi = \phi(r) \qquad \text{and} \qquad A_\mu dx^\mu = \Phi(r)dt \tag{4.3}$$

with the radial location of the black hole horizon given by the largest root of $h(r_H) = 0$.

4.1.1 Equations of Motion

The equations of motion are obtained by extremizing the action in Eq. (4.1) with respect to the fields in the EDM model defined in Eq. (4.2) and Eq. (4.3). They are given by [89]

$$\begin{aligned}
&\phi''(r) + \left[\frac{h'(r)}{h(r)} + 4A'(r) - B'(r)\right]\phi'(r) \\
&\quad - \frac{e^{2B(r)}}{h(r)}\left[\frac{\partial V(\phi)}{\partial\phi} - \frac{e^{-2[A(r)+B(r)]}\Phi'(r)^2}{2}\frac{\partial f(\phi)}{\partial\phi}\right] = 0
\end{aligned} \tag{4.4}$$

$$\Phi''(r) + \left[2A'(r) - B'(r) + \frac{d\left[\ln\left(f(\phi)\right)\right]}{d\phi}\phi'(r)\right]\Phi'(r) = 0 \tag{4.5}$$

$$A''(r) - A'(r)B'(r) + \frac{\phi'(r)^2}{6} = 0 \tag{4.6}$$

$$h''(r) + [4A'(r) - B'(r)]h'(r) - e^{-2A(r)}f(\phi)\Phi'(r)^2 = 0\,. \tag{4.7}$$

By combining the independent components of Einstein's equations, a constraint on the fields is obtained

$$h(r)[24A'(r)^2 - \phi'(r)^2] + 6A'(r)h'(r) + 2e^{2B(r)}V(\phi) + e^{-2A(r)}f(\phi)\Phi'(r)^2 = 0 \tag{4.8}$$

There are two conserved charges in the radial direction associated with the EMD equations of motions: the Gauss charge Q_G, and the Noether charge Q_N [89]

$$\begin{aligned} Q_G(r) &= f(\phi)\mathrm{e}^{2A(r)-B(r)}\Phi'(r), \\ Q_N(r) &= \mathrm{e}^{2A(r)-B(r)}\left[\mathrm{e}^{2A(r)}h'(r) - f(\phi)\Phi(r)\Phi'(r)\right]. \end{aligned} \tag{4.9}$$

Using these conserved charges, the equation of motion in Eq. (4.5) for the gauge field $\Phi(r)$ can be rewritten as $\frac{dQ_G}{dr} = 0$, while the equation of motion in Eq. (4.7) for the blackening function $h(r)$ is obtained from $\frac{dQ_N}{dr} = 0$. The constraints in Eq. (4.8) and the conserved charges are used when numerically extracting thermodynamical quantities in Section 4.2.

On the other hand, the background function $B(r)$ can be fixed to any value since it does not show any dynamics in the equations of motion. In order to simplify numerical calculations, $B(r)$ is chosen to be zero everywhere.

4.2 Numerical Calculation of Thermodynamic Quantities

In order to numerically solve the EMD equations of motion and calculate physical observables, it is convenient to use two different sets of coordinates: the standard holographic coordinates denoted with a tilde, and the numerical holographic coordinates without tilde. In the standard coordinates, the blackening function goes to unity at the boundary, and the thermodynamical quantities are calculate using standard holographic formulas. On the other hand, to numerically solve the EMD equations of motion, it is convenient to rescale some of the Taylor coefficients obtained by expanding the EMD fields near the black hole horizon in order to initiate the numerical integration of the equations of motion from close to the horizon up to the asymptotically far AdS_5

spacetime.

4.2.1 Standard Holographic Coordinates

The EDM fields in Eqs. (4.2,4.3) using the gauge $\tilde{B}(\tilde{r}) = 0$, in the standard coordinates are given by

$$\begin{aligned} d\tilde{s}^2 &= e^{2\tilde{A}(\tilde{r})}\left[-\tilde{h}(\tilde{r})d\tilde{t}^2 + d\vec{\tilde{x}}^2\right] + \frac{d\tilde{r}^2}{\tilde{h}(\tilde{r})} \\ \tilde{\phi} &= \tilde{\phi}(\tilde{r}), \quad \tilde{A} = \tilde{A}_\mu d\tilde{x}^\mu = \tilde{\Phi}(\tilde{r})d\tilde{t} \end{aligned} \tag{4.10}$$

Physical quantities in the gauge theory are obtained from the far-from-the-horizon, near-boundary behavior of the bulk fields. The ultraviolet behavior of these fields are obtained by considering $\tilde{r} \to \infty$, where:

$$\tilde{\phi}(\tilde{r} \to \infty) \to 0 \qquad \tilde{h}(\tilde{r} \to \infty) \to 1 \qquad V(0) = -12 \qquad f(0) = \text{const} \tag{4.11}$$

and the background metric goes back to the AdS_5 geometry. Then the EMD equations of motion are solved in terms of $\tilde{A}(\tilde{r})$ and $\tilde{\Phi}(\tilde{r})$. After this is done, a backreaction of these fields into the dynamics of $\tilde{\phi}(\tilde{r})$ is considered by plugging these results back into the EMD equations of motion and solving them for $\tilde{\phi}(\tilde{r})$ with the dilaton potential truncated at quadratic order. This backreacted process may be repeated to obtain the

following ultraviolet expansion of the EMD fields

$$\begin{aligned}
\tilde{A}(\tilde{r}) &= \tilde{r} + \mathcal{O}\left(e^{-2\nu\tilde{r}}\right), \\
\tilde{h}(\tilde{r}) &= 1 + \mathcal{O}\left(e^{-4\tilde{r}}\right), \\
\tilde{\phi}(\tilde{r}) &= e^{-\nu\tilde{r}} + \mathcal{O}\left(e^{-2\nu\tilde{r}}\right), \\
\tilde{\Phi}(\tilde{r}) &= \tilde{\Phi}_0^{\text{far}} + \tilde{\Phi}_2^{\text{far}} e^{-2\tilde{r}} + \mathcal{O}\left(e^{-(2+\nu)\tilde{r}}\right),
\end{aligned} \tag{4.12}$$

where $\nu \equiv d - \Delta$, $d = 4$ is the number of spacetime dimensions of the dual gauge theory,

$$\Delta = (d + \sqrt{d^2 + 4m^2})/2 \tag{4.13}$$

is the scaling dimension of the gauge theory operator dual to the dilaton field and m is the mass of the dilaton obtained by Taylor expanding the dilaton potential close to the boundary.

The temperature of the gauge theory is obtained by the Hawking's temperature of the black hole,

$$T = \left.\frac{\sqrt{-g'_{\tilde{t}\tilde{t}} g^{\tilde{r}\tilde{r}\,\prime}}}{4\pi}\right|_{\tilde{r}=\tilde{r}_H} \Lambda = \frac{e^{\tilde{A}(\tilde{r}_H)}}{4\pi} |\tilde{h}'(\tilde{r}_H)| \Lambda, \tag{4.14}$$

where the energy scale Λ is used to express T in physical units. The energy scale introduced here gives a self-consistent setup to convert holographic units to physical ones. This is different from to the strategy employed in [89], where different units where introduced to convert each thermodynamical quantity artificially augmenting the number of free parameters of the holographic model.

The entropy density in the gauge theory is associated with the area of the bulk black hole horizon by the Bekenstein-Hawking formula [90, 91],

$$s = \frac{A_H}{4G_5 V}\Lambda^3 = \frac{2\pi}{\kappa_5^2} e^{3\tilde{A}(\tilde{r}_H)}\Lambda^3 \tag{4.15}$$

and the baryon chemical potential in the gauge theory is extracted from the boundary value of the gauge field

$$\mu_B = \lim_{\tilde{r}\to\infty} \tilde{\Phi}(\tilde{r})\Lambda = \tilde{\Phi}_0^{\text{far}}\Lambda, \tag{4.16}$$

while the baryon charge density is obtained from the boundary value of the radial momentum conjugate to the Maxwell field,

$$\rho_B = \lim_{\tilde{r}\to\infty} \frac{\partial\mathcal{L}}{\partial\left(\partial_{\tilde{r}}\tilde{\Phi}\right)}\Lambda^3 = \frac{Q_G(\tilde{r}\to\infty)}{2\kappa_5^2}\Lambda^3 = -\frac{\tilde{\Phi}_2^{\text{far}}}{\kappa_5^2}\Lambda^3. \tag{4.17}$$

4.2.2 Numerical Holographic Coordinates

A different set of coordinates is defined in this section to numerically solve the EMD equations of motion and extract the thermodynamic variables. In order to initiate the integration of the equations of motion, the first step is to consider a Taylor expansion of the EMD fields near horizon

$$X(r) = \sum_{n=0}^{\infty} X_n (r - r_H)^n, \qquad \text{where} \qquad X = \{A, h, \phi, \Phi\} \tag{4.18}$$

In this expansion, it is possible to rescale the holographic coordinate to fix $r_H = 0$; $h_0 = 0$ follows from the fact that the blackening function has a simple zero at the black hole horizon; $h_1 = 1$ and $A_0 = 0$ are fixed by rescaling the time coordinate and the spacetime coordinates parallel to the boundary respectively, by a common factor. Φ_0 is

set to zero, otherwise an ill defined Maxwell field is obtained.

The nonzero near horizon Taylor coefficients h_0, h_1, A_0 and Φ_0 are determined in terms of only two initial conditions (ϕ_0, Φ_1) by solving the EMD equations of motion order by order considering the expansion in Eq. (4.19). The numerical integration is then started from $r_{\text{start}} \to 0$ up to a value r_{max} where the black hole backgrounds have already reached the far-horizon corresponding to the AdS_5 spacetime. By analyzing Eq. (4.6) in the gauge $B(r) = 0$

$$A''(r) = -\frac{\phi'(r)^2}{6} \leq 0 \tag{4.19}$$

one can see that $A(r)$ is a concave function of the holographic coordinate. However, for asymptotically AdS_5 geometries, the background function $A(r)$ must increase for large values of r, which implies a positive derivative at the horizon, $A_1 > 0$. By plugging the near horizon expansions into the constraint (4.8) and evaluating it at the black hole horizon one obtains

$$A_1 = -\frac{1}{6}\left[2V(\phi_0) + f(\phi_0)\Phi_1^2\right] \tag{4.20}$$

here, $V(\phi)$ is negative defined, and $f(\phi)$ is positive-defined implying that $A_1 > 0$ only for [89]

$$\Phi_1 < \sqrt{-\frac{2V(\phi_0)}{f(\phi_0)}} \equiv \Phi_1^{\text{max}}(\phi_0). \tag{4.21}$$

In the numerical coordinates, the ultraviolet behavior of these fields is

$$\begin{aligned} A(r) &= \alpha(r) + \mathcal{O}\left(e^{-2\nu\alpha(r)}\right), \\ h(r) &= h_0^{\text{far}} + \mathcal{O}\left(e^{-4\alpha(r)}\right), \\ \phi(r) &= \phi_A e^{-\nu\alpha(r)} + \mathcal{O}\left(e^{-2\nu\alpha(r)}\right), \\ \Phi(r) &= \Phi_0^{\text{far}} + \Phi_2^{\text{far}} e^{-2\alpha(r)} + \mathcal{O}\left(e^{-(2+\nu)\alpha(r)}\right), \end{aligned} \tag{4.22}$$

where

$$\alpha(r) = (A_{-1}^{\text{far}})r + A_0^{\text{far}}. \tag{4.23}$$

Evaluating the constraint (4.8) at the boundary gives

$$A_{-1}^{\text{far}} = \frac{1}{\sqrt{h_0^{\text{far}}}} \tag{4.24}$$

and by equating the radially conserved Gauss charge in Eq. (4.9) evaluated at the horizon and at the boundary

$$\Phi_2^{\text{far}} = -\frac{\sqrt{h_0^{\text{far}}}}{2f(0)} f(\phi_0)\Phi_1 . \tag{4.25}$$

The thermodynamic quantities calculated in this dissertation are obtained from the coefficients h_0^{far}, Φ_0^{far}, Φ_2^{far}, and ϕ_A from the fields evaluated at $r_{\max}$. They can be determined by relating the standard and the numerical coordinates

$$\tilde{\phi}(\tilde{r}) = \phi(r) \qquad d\tilde{s}^2 = ds^2 \qquad \tilde{\Phi}(\tilde{r})d\tilde{t} = \Phi(r)dt \tag{4.26}$$

and by comparing the ultraviolet asymptotics given in Eq. (4.12) and Eq. (4.22) [89],

$$\tilde{r} = \frac{r}{\sqrt{h_0^{\text{far}}}} + A_0^{\text{far}} - \ln(\phi_A^{1/\nu}) \qquad \tilde{A}(\tilde{r}) = A(r) - \ln(\phi_A^{1/\nu}) \tag{4.27}$$

$$\vec{\tilde{x}} = \phi_A^{1/\nu}\vec{x} \qquad \tilde{t} = \phi_A^{1/\nu}\sqrt{h_0^{\text{far}}}\, t \qquad \tilde{h}(\tilde{r}) = \frac{h(r)}{h_0^{\text{far}}} \tag{4.28}$$

$$\tilde{\Phi}(\tilde{r}) = \frac{\Phi(r)}{\phi_A^{1/\nu}\sqrt{h_0^{\text{far}}}} \qquad \tilde{\Phi}_0^{\text{far}} = \frac{\Phi_0^{\text{far}}}{\phi_A^{1/\nu}\sqrt{h_0^{\text{far}}}} \qquad \tilde{\Phi}_2^{\text{far}} = \frac{\Phi_2^{\text{far}}}{\phi_A^{3/\nu}\sqrt{h_0^{\text{far}}}}\,. \tag{4.29}$$

The thermodynamical quantities are obtained from the numerical coordinates by

$$T = \frac{1}{4\pi\phi_A^{1/\nu}\sqrt{h_0^{\text{far}}}}\,\Lambda \tag{4.30}$$

$$\mu_B = \frac{\Phi_0^{\text{far}}}{\phi_A^{1/\nu}\sqrt{h_0^{\text{far}}}}\,\Lambda \tag{4.31}$$

$$s = \frac{2\pi}{\kappa_5^2\,\phi_A^{3/\nu}}\,\Lambda^3 \tag{4.32}$$

$$\rho_B = \frac{-\Phi_2^{\text{far}}}{\kappa_5^2\,\phi_A^{3/\nu}\sqrt{h_0^{\text{far}}}}\,\Lambda^3\,. \tag{4.33}$$

These expressions relates directly the numerical solutions of the equations of motion Eqs. (4.4-4.7) to a thermodynamical point in a gauge theory. In the next section, the free parameters of the model are fixed in such a way to match lattice QCD calculations at $\mu_B = 0$.

4.3 Engineering EMD Black Hole Model

The free scaling parameters of the EMD model and the free functions are engineered by matching the black hole solutions with lattice QCD results with $2+1$ flavors and physical quark masses calculated at $\mu_B = 0$ in the process called "black hole engineering" in [24]. In particular, the scalar potential $V(\phi)$ is constructed to reproduce the entropy density $s(t)$, which is directly calculated from the black hole model in Eqs. (4.30,4.32). On the other hand, the gauge field in the bulk is associated with a conserved charge at the boundary; to ensure that the charge is baryonic, the Maxwell-dilaton coupling $f(\phi)$ is constructed to reproduce the second baryon susceptibility χ_2. A simple expression for the second susceptibility at zero chemical potential was obtained in [89] in terms of holographic parameters

$$\chi_2(\mu_B = 0) = \frac{1}{16\pi^2}\frac{s}{T^3}\frac{1}{f(0)\int_{r_H}^{\infty} dr\, \mathrm{e}^{-2A(r)} f^{-1}(\phi(r))}, \tag{4.34}$$

this expression is evaluated using the black hole backgrounds defined at $\mu_B = 0$, obtained by setting the initial condition Φ_1 to zero.

The first quantities to be engineered are the potential $V(\phi)$, the gravitational constant κ_5^2 and the energy scale Λ. If the potential V does not depends on ϕ, in particular if $V_0 = 20/L^2$ where L is the AdS radius like in Eq. (1.27), the dual theory turns out to have conformal symmetry with speed of sound $c_s^2 = \frac{1}{3}$ as expected from a CFT. The first attempt to obtain $V(\phi)$ was done in [92]. There, it was considered that if $V(\phi)$ has a simple exponential form:

$$V(\phi) = V_0 \mathrm{e}^{\gamma\phi} \qquad \text{with:} \qquad V_0 = \frac{20}{L^2} \qquad \text{and} \qquad \gamma = \frac{1}{6} \tag{4.35}$$

it will produce a

$$c_s^2 = \frac{1}{3} - \frac{\gamma^2}{2}. \tag{4.36}$$

Thus, the theory will be non-conformal, and c_s^2 will change only by a constant with respect to the CFT in Eq. (1.27). The next step in the attempt to translate the profile of $V(\phi)$ into an arbitrary EoS was to assume γ as a slowly varying function of ϕ. In this approximation, it was shown that

$$c_s^2 \approx \frac{1}{3} - \frac{1}{2}\frac{V'(\phi_H)^2}{V(\phi_H)^2} \tag{4.37}$$

where ϕ_H is the value of ϕ at the horizon. This approximation gives a particular dependence of $V(\phi)$ on the thermodynamical variables. However, it does not work well for small values of ϕ_H, where $V(\phi)$ is close to a maximum. By studying the asymptotic behavior of the model when $\phi_H \to 0$, it was found that a simple stable solution was given by the analytic function

$$V(\phi)_{cosh} = -\frac{12}{L^2}\cosh\gamma\phi\,. \tag{4.38}$$

This equation has been shown to be stable for a wide range of ϕ_H. The parameter γ is restricted by c_s^2 in Eq. (4.36) to be $\gamma \leq \sqrt{2/3}$. Starting from the simple function obtained in Eq. (4.38), the authors of [93] added correcting terms proportional to ϕ^2. The same functional form is used here

$$V(\phi) = -12\cosh(\gamma\,\phi) + b_2\,\phi^2 + b_4\phi^4 + b_6\phi^6\,. \tag{4.39}$$

This equation must satisfy the Breitenlohner-Freedman bound [94–96]

$$m^2 L^2 \geq -4 \tag{4.40}$$

where the dilaton mass term is obtained from

$$m^2 = V''(\phi)|_{\phi \to 0} \tag{4.41}$$

and the scaling dimension Δ, defined in Eq. (4.13), must satisfy the constraint $2 < \Delta < 4$.

In this dissertation, the parameters in Eq. (4.39) were fixed by ocular inspection to follow the entropy density on the lattice like is shown in the left panel of Figure 4.1. They are given by

$$\gamma = 0.63 \qquad b_2 = 0.65 \qquad b_4 = 0.05 \qquad b_6 = 0.003 \tag{4.42}$$

The gravitational constant and energy scale are given respectively by

$$\kappa_5^2 = 8\pi G_5 = 8\pi(0.46) \qquad \Lambda = 1058.83\ \mathrm{MeV}\,; \tag{4.43}$$

they were originally fixed in [97], and this choice turns out to work well with the potential in Eq. (4.39).

The parameters that have been set in Eqs. (4.39,4.43) fix the thermodynamics of the gauge theory at $\mu_B = 0$. They are not affected by the introduction of the Maxwell-dilaton coupling $f(\phi)$. This coupling will produce a response of the thermodynamics to a change in chemical potential. The function $f(\phi)$ is constructed to mimic χ_2. The intuition behind the functional form is based on the similar behavior between χ_2 and

$\frac{s}{T^3}$ in Eq. (4.34) and also on the lattice. They both start from zero, increase rapidly during the crossover, and tend to a finite value for $T \gg T_c$. However, χ_2 stays close to its high-temperature value down to a lower temperature than $\frac{s}{T^3}$ before plunging rapidly to small values (see Figure 4.1). The integration in Eq. (4.34) makes the difference between χ_2 and $\frac{s}{T^3}$.

The argument, given in [89], is that the integral in Eq. (4.34) becomes small at the horizon where $\phi \to 0$ due to the factor e^{-2A} in the integral. Since ϕ is expected to go from $\phi = 0$ to positive values, $f(\phi)$ needs first to increase as a function of ϕ, then to decrease rapidly. In that way, χ_2 will start increasing at higher temperatures than s/T^3. With that feature in mind, $f(\phi) \sim \text{sech}(\phi)$ in [89].

In this work, the Maxwell-dilaton coupling is constructed with a similar structure, but adding more parameters to give freedom to adjust to the lattice calculations. The Maxwell-dilaton coupling function form is

$$f(\phi) = \frac{\text{sech}\left(c_1\phi + c_2\phi^2\right)}{1+c_3} + \frac{c_3}{1+c_3}\,\text{sech}(c_4\phi), \tag{4.44}$$

where the parameters are given by

$$c_1 = -0.27 \qquad c_2 = 0.4 \qquad c_3 = 1.7 \qquad c_4 = 100 \tag{4.45}$$

and $f(0) \to 1$ as is expected.

Figure 4.1 shows the excellent agreement of our model when compared with lattice calculations for both s/T^3 and χ_2. On the left panel, the black hole s/T^3 is shown as a function of T. The lattice points were taken from [28]. The right panel of this figure shows χ_2 for three different parameters of the the black hole model in comparison to lattice calculations taken from [98]. The best fitting, showed with a black line, was obtained with the parameters in Eq. (4.45). All the results in Chapter 5, including the

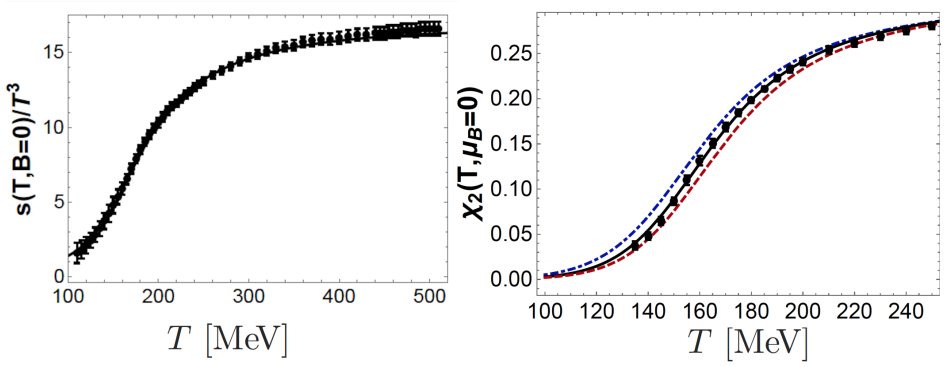

FIGURE 4.1: Left panel: lattice QCD calculations (BW [28]) compared with holographic results for the normalized entropy density as a function of the temperature. Right panel: lattice QCD calculations (WB [98]) compared with three different holographic results, for the second baryon susceptibility χ_2. The solid black curve represents the best choice of parameters used in this work. The dotted red and dot-dashed blue curves are generated by varying either c_1 or c_2 in Eq. (4.44)

prediction for the CEP, use the best fitting, which crosses over the lattice points. However, in order to quantify the dependence of the location of the CEP on the parameters of the model, two additional fitting were done trying to enclose the error bars on the lattice points. Those curves were obtained by changing one of the parameters of $f(\phi)$ while keeping the rest unchanged. The dashed red curve below the lattice points was obtained by setting $c_1 = -0.189$, while for the dot-dashed blue curve above the lattice points, the parameter that changed was $c_2 = 0.36$. The results of combining the three fits will permit to estimate a range in the QCD phase diagram for the location of the CEP (see Section 5.4.1).

4.3.1 Locating the QCD Critical End Point

This section discusses how the black hole solutions map into the QCD phase diagram, and the strategy followed to localize the CEP and the line of first-order phase transition found in our Black Hole model, as explained in [99]. The two initial variables that

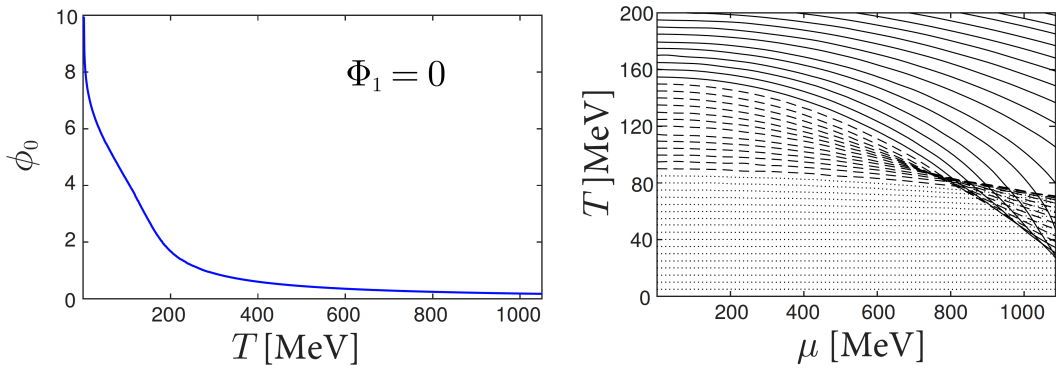

FIGURE 4.2: Mapping of the initial values of the black holes (ϕ_0, Φ_1) to the QCD phase diagram (T, μ_B). Left panel: T-dependence of ϕ_0 when $\Phi_1 = 0$ ($\mu_B = 0$). Right panel: lines of constant ϕ_0 evolving in the μ_B direction as Φ_1 increases.

defines of a black hole are the value of the field at the near-horizon, ϕ_0, and the value of the electric field, Φ_1, in the holographic direction r. Setting $\Phi_1 = 0$, corresponds to values over the T axis, where $\mu_B = 0$, as shown on the left panel of Figure 4.2. The mapping is highly non-linear, thus, to populate the QCD phase diagram with black hole solutions, the variable ϕ_0 is chosen to produce equally spaced intervals of T. Then, Φ_1 is increased from zero to the maximum bound described in Eq. (4.21). The right panel in Figure 4.2 shows the lines of constant ϕ_0 evolving in the μ_B direction as Φ_1 increases. One can distinguish between three kinds of lines: the dotted lines that do not cross each other; the dashed lines in the middle of the plane that cross some of the dotted lines; and the solid lines on the top of the plane that cross some of the dotted and dashed lines.

The crossing of the lines creates a region of the phase diagram with multi-solutions that begins at the point with $T^c = 89$ MeV and $\mu_B^c = 724$ MeV, and extends to lower T and higher μ_B. The stable solution in this region is required to minimize the free energy

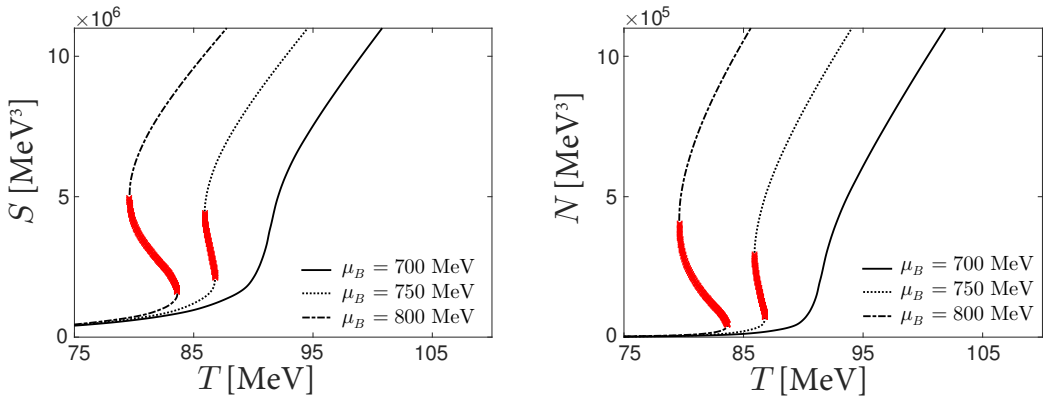

FIGURE 4.3: Thermodynamic quantities obtained from the Black Hole model as function of T for $\mu_B = 700$ MeV, $\mu_B = 750$ MeV, and $\mu_B = 800$ MeV. Left panel: entropy density. Right panel: baryon number density. The thick red lines indicate thermodynamically unstable points.

(or maximize the entropy), and also to be locally stable under small fluctuations. Thermodynamic stability requires the entropy (S), and the baryon number (N) to be positive definite. Figure 4.3 shows S and N as functions of T for three different values of μ_B: one below μ_B^c ($\mu_B = 700$) and two above μ_B^c ($\mu_B = 750$ and $\mu_B = 800$). This figure also shows, with a thick red line, the values of S and N that are thermodynamically unstable. The unstable regions belong to the dashed lines in the phase diagram in Figure 4.2, which is the plane that is bent in the middle between the dotted and the solid lines. Moreover, it was found that the entropy S is higher in the dotted lines than in the dashed lines at fixed μ_B. Therefore, the system will maximize the entropy by moving from the lower plane (dotted lines on the right panel in Figure 4.2) to the higher plane (solid lines on the right panel in Figure 4.2), and when the overlapping between those two regions begin, a discontinuity in the entropy and baryon density is developed, and therefore, a first order phase transition happens. This transition extends along the line defined by the boundary of those two regions (dotted and solid lines). The point where the overlapping of the planes begins ($T^c = 89$ MeV, $\mu_B^c = 724$ MeV) was identify as the location

of the CEP in our holographic model.

Chapter 5

Black Hole Results

This chapter shows the main results obtained using the Black Hole model described in Chapter 4. The model parameters were adjusted to match two crucial observables calculated on the lattice and are shown in Eqs. (4.39,4.43,4.44). The only exception was when estimating the uncertainty in the location of the CEP. In this case, the best fit was combined with other two different sets of parameters, adjusted to enclose the lattice data corresponding to the second baryon susceptibility χ_2, as explained in Section 4.3.

Most of the results presented in this chapter were summarized in [24], and published in proceeding journals [99–103]. Remarkably, the best set of parameters in the Black Hole model produces black hole solutions that match the entropy density s/T^3 and the second baryon susceptibility χ_2 from lattice calculations with great precision at $\mu_B = 0$, as shown in the upper panels of Figure 5.1. Once those parameters are fixed, the output of the Black Hole model is mapped onto the QCD phase diagram producing an entropy $s(T, \mu_B)/T^3$ and a baryon density $\rho_B(T, \mu_B)/T^3$ as functions of T and μ_B, which are shown in the lower panels, of Figure 5.1. Here we consider black hole solutions that map the QCD phase diagram in the range $T = \{50 - 400\}$ MeV and $\mu_B = \{0 - 750\}$ MeV. The calculations that are presented in this chapter are derived from those two thermodynamical quantities, and therefore are predictions of our

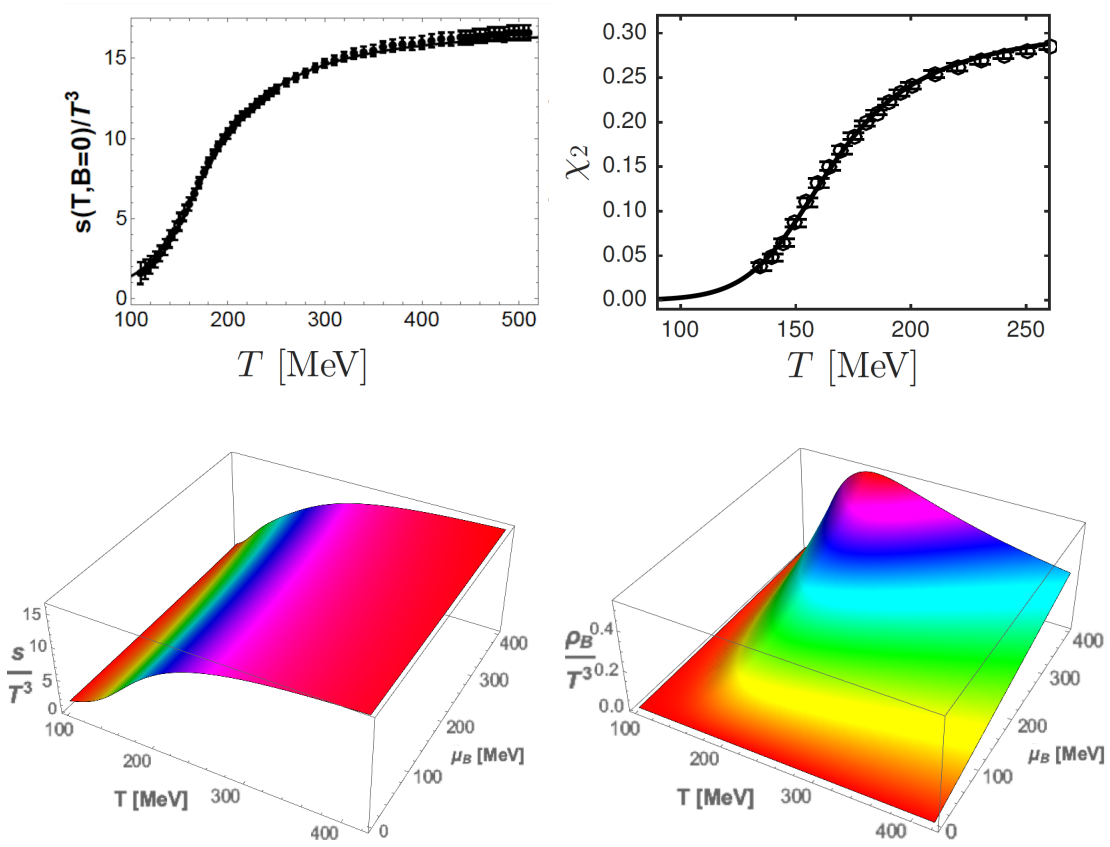

FIGURE 5.1: Upper panel: lattice QCD calculations (BW [28]) compared with holographic results for the normalized entropy density s/T^3 and the second baryon density χ_2 as functions of the temperature T, at zero baryonic chemical potential μ_B. Lower panel: normalized entropy density s/T^3, and normalized baryon density $\rho_B(T,\mu_B)/T^3$, obtained from the Black Hole model, as functions fo T and μ_B

model.

5.1 Thermodynamical Quantities at $\mu_B = 0$

The thermodynamical quantities at $\mu_B = 0$ are obtained by setting the black-hole initial condition Φ_1 to zero, while changing ϕ_0. The entropy was computed directly by using

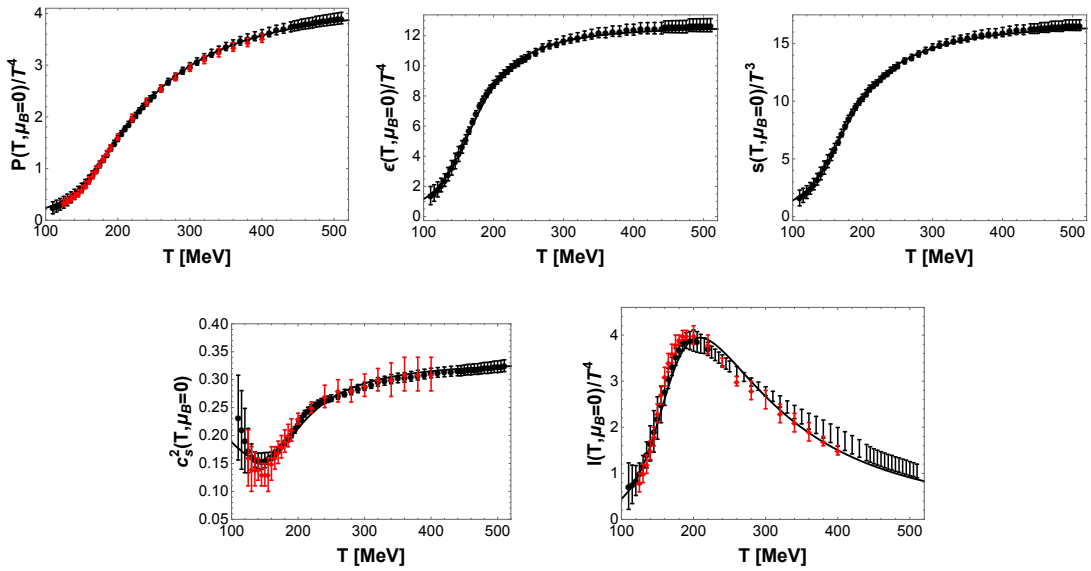

FIGURE 5.2: Normalized thermodynamical quantities calculated in the Black Hole model as functions of the temperature T, at zero baryonic chemical potential μ_B, in comparison with lattice QCD results. The black points were obtained from [28], and the red points from [104]. Upper left panel: pressure (p/T^4). Upper central panel: energy density (ϵ/T^4). Upper right panel: entropy (s/T^3). Lower right panel: speed of sound squared (c_s^2). Lower right panel: trace anomaly (I/T^4).

the Bekenstein-Hawking relation in Eq. (4.32). The pressure is obtained by integrating the entropy, while the rest of the thermodynamical quantities are calculated from the pressure. Figure 5.2 shows the normalized pressure, (p/T^4), followed by the energy density (ϵ/T^4), the entropy (s/T^3), the speed of sound squared (c_s^2), and the trace anomaly (I/T^4). One can see that the holographic result agrees quantitatively very well with the lattice data taked from [28, 104].

One can note, from the behavior of s, that the degrees of freedom smoothly change from hadrons to a QGP state at $T_c \sim 155$ MeV. Moreover, c_s^2 and I/T^4, which are sensitive thermodynamical quantities obtained by second derivatives of the pressure, give

an overall good description of the lattice points. I/T^4 in particular measures the deviation of the system from a conformal one, and is an indicator of the strength of the interaction. The Black Hole model, having a small shear viscosity per entropy density η/s, is expected to be a good approximation for computations of transport properties when the system is highly interacting, which happens during and after the crossover.

5.2 Baryon Susceptibilities

Among the most interesting thermodynamical observables to calculate, from the baryonic pressure, are the susceptibilities because:

- They provide essential information about the effective degrees of freedom of a system.
- The susceptibilities calculated at $\mu_B = 0$ can be used to Taylor expand the pressure at finite μ_B.
- They are directly related to the moments of the distribution measured on an event-by-event basis in particle colliders.
- They are very sensitive to the CEP since they scale with different powers of the diverging correlation length ξ.

This section presents the baryon susceptibilities calculated in the Black Hole model, and shows their behavior close to the CEP. The susceptibilities obtained in the Black Hole model at $\mu_B = 0$ are used to Taylor expand the pressure in powers of μ_B/T to find the threshold at which the expansion breaks down. The ratio of susceptibilities are compared with the moments of the net-proton distribution measured at RHIC and the chemical freeze-out parameters for several collision energies are extracted and compared with previous analyses.

5.2.1 Higher Order Susceptibilities

The first-order susceptibility is proportional to the baryon density computed directly from the Black Hole model $\chi_1 = \rho_B/T^3$. Higher order susceptibilities can be obtained by taking derivatives of ρ_B/T^3 with respect to μ_B/T.

$$\chi_{n+1}(T,\mu_B) = \frac{\partial^n(\rho_B/T^3)}{\partial(\mu_B/T)^n}\,. \tag{5.1}$$

In the vicinity of the CEP, the higher order baryon number susceptibilities diverge with different powers of the correlation length ξ, as written in Eq. (1.24).

The black hole susceptibilities χ_2 and χ_4 are shown in the left panel of Figure 5.3 as functions of T for different values of μ_B. One can see that χ_2 begins to develop a peak as μ_B increases, which eventually evolves into a divergence at the CEP. The latter is located at $T_{\rm CEP} = 89$ MeV and $\mu_B^{\rm CEP} = 724$ MeV in our Black Hole model. Since χ_4 is more sensitive to the CEP, the peak is shown even for smaller values of μ_B. It also displays the negative peak when approaching the CEP from low T, as expected from universality arguments [39]. This panel also shows the available lattice results for χ_2, χ_4 [80]. The right panels show χ_6 and χ_8 calculated in the Black Hole model at $\mu_B = 0$ in comparison with the lattice data from [23]. The error-band on χ_6 and χ_8 indicates the uncertainty due to the numerical calculation. Notice that those predictions were obtained one year before the lattice results were available. Even though the lattice calculation for χ_8 is only an estimate, both results exhibit the features expected from universality arguments [105].

5.2.2 Reconstruction of the EoS

Using the higher order susceptibilities calculated at $\mu_B = 0$, one can reconstruct the system's pressure P and baryon density ρ_B as a Taylor series in powers of μ_B/T as

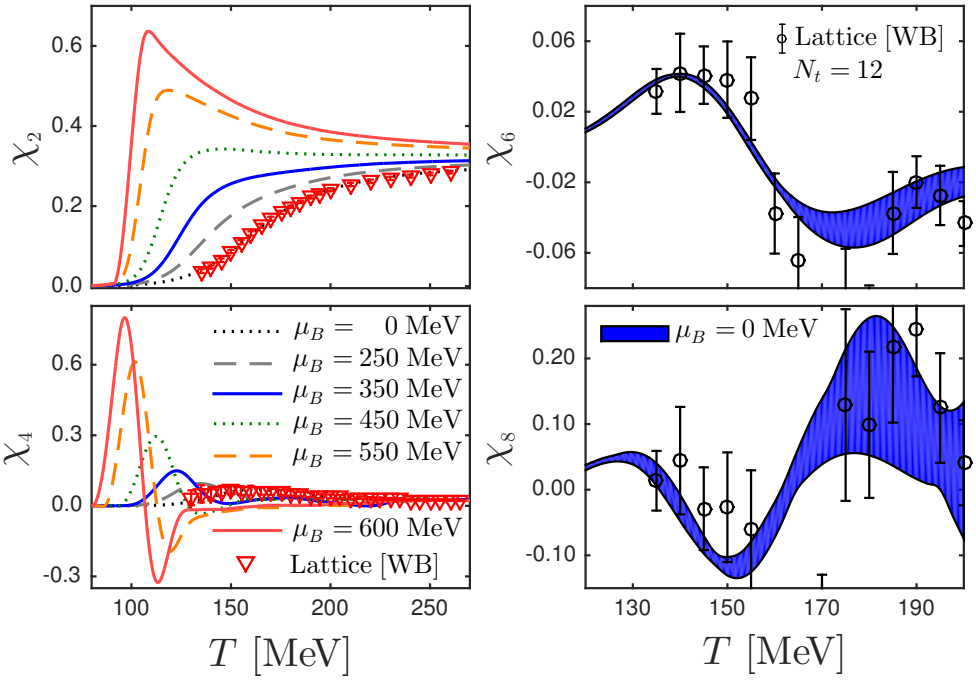

FIGURE 5.3: Baryon number susceptibilities (χ_n) as functions of T for different values of μ_B, computed using the EMD Black Hole model in comparison with lattice results at $\mu_B = 0$. Left panel: χ_2 and χ_4 for values of μ_B in the range of $[0 - 600]$ MeV. The lattice results at zero μ_B were taken from WB: [80]. Left panel: χ_6 and χ_8 are shown at zero μ_B. The error-band on those susceptibilities denotes the uncertainty in the numerical calculation. The Lattice results at zero μ_B were taken from WB: [23].

follows

$$\frac{P(T,\mu_B) - P(T,\mu_B = 0)}{T^4} = \sum_{n=1}^{\infty} \frac{1}{(2n!)} \chi_{2n}(T) \left(\frac{\mu_B}{T}\right)^{2n}, \tag{5.2}$$

$$\frac{\rho_B(T,\mu_B)}{T^3} = \sum_{n=1}^{\infty} \frac{1}{(2n-1)!} \chi_{2n}(T) \left(\frac{\mu_B}{T}\right)^{2n-1}. \tag{5.3}$$

A Taylor expansion of observables computed at $\mu_B = 0$ is a common analysis done with lattice calculations to access a finite region of μ_B. The expansion is considered

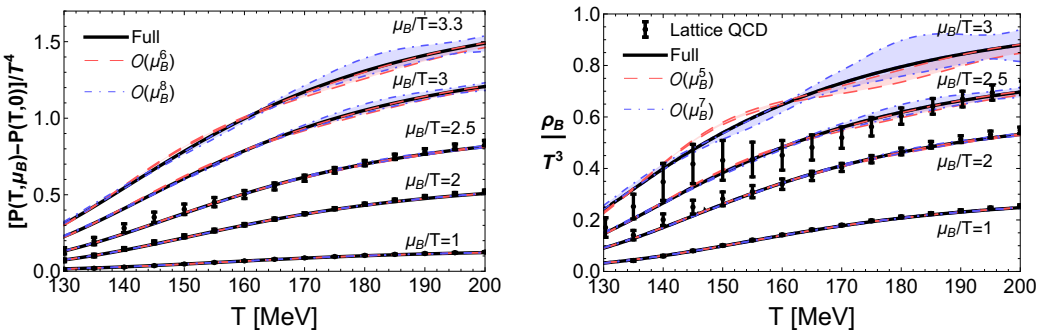

FIGURE 5.4: The μ_B-dependent contributions to p (left panel) and ρ_B (right panel) as functions of T for different values of μ_B/T. The solid curves correspond to the full calculation in the Black Hole model. The bands denote the Taylor series reconstruction using the susceptibilities in Figure 5.3. The lattice points correspond to the reconstructed Taylor series up to $\mathcal{O}(\mu_B^6)$ for p and $\mathcal{O}(\mu_B^5)$ for ρ_B computed in [20].

stable for a certain ratio of μ_B/T if adding another term to the Taylor expansion does not show a variation in the observable. Figure 5.4 shows the Taylor expansion of the pressure and baryon susceptibility up to χ_6 done on the lattice in [20]. In this analysis, it was determined that the pressure and the baryon density could be expanded up to a ratio of $\mu/T \leq 2$ before the expansion breaks down. The same analysis is shown in Figure 5.4, with the susceptibilities calculated in the Black Hole model from Figure 5.3. The pressure difference in Eq. (5.2), and the baryon density in Eq. (5.3) calculated in the holographic model with no truncations are shown as black curves. The Taylor expansion up to order $\mathcal{O}(\mu_B^6)$ is shown as a red band enclosed with dashed lines, while the Taylor expansion up to order $\mathcal{O}(\mu_B^8)$ is shown as a blue band enclosed with dot-dashed lines. The analysis with the Black Hole model susceptibilities confirms the applicability of the $\mathcal{O}(\mu_B^6)$ truncation done in [20] for $\mu_B/T \leq 2$, and it also predicts that the inclusion of $\chi_8(T)$ into the expansion extends the domain of applicability of the Taylor series to at least $\mu_B/T \sim 2.5$.

In Figure 5.5, an analogous Taylor series reconstruction for χ_2 and χ_4 is obtained

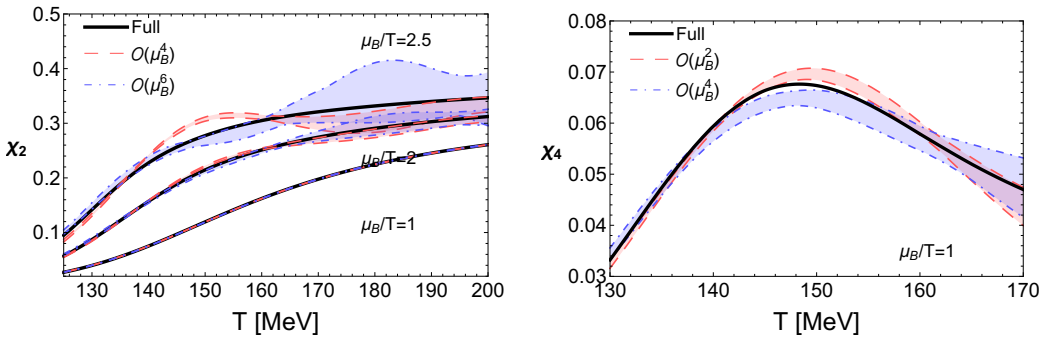

FIGURE 5.5: The μ_B-dependent contribution to χ_2 (left panel) and χ_4 (right panel) as functions of T for different values of μ_B/T. The solid curves correspond to the full calculation in the Black Hole model. The bands denote the Taylor series reconstruction using the susceptibilities in Figure 5.3.

up to $\mathcal{O}(\mu_B^6)$ red curves, and $\mathcal{O}(\mu_B^8)$ blue curves. Since the higher order susceptibilities are more sensitives to the CEP, any information that could be extracted from their reconstruction could be relevant to investigate critical behavior.

The reconstructed χ_2 is shown for $\mu_B/T = \{1, 2, 2.5\}$ in comparison with the full holographic result. There is a good agreement up to $\mu_B/T \sim 2$ using terms up to $\mathcal{O}(\mu_B^6)$. On the other hand, for $\mu_B/T \sim 2.5$, χ_2 shows a bump at $\mathcal{O}(\mu_B^4)$, product of the limited number of terms in the Taylor series. The bump is reduced with the inclusion of the terms up to $\mathcal{O}(\mu_B^6)$. One has to be carful with this kind of behavior, which is not an indication of criticality but of the truncation of the Taylor expansion. This fact highlights the need of higher order susceptibilities to study critical phenomena. In the case of the reconstruction of χ_4, one can see that the Taylor expansion does not reproduce the right behavior even for $\mu_B/T = 1$ when using terms up to $\mathcal{O}(\mu_B^4)$.

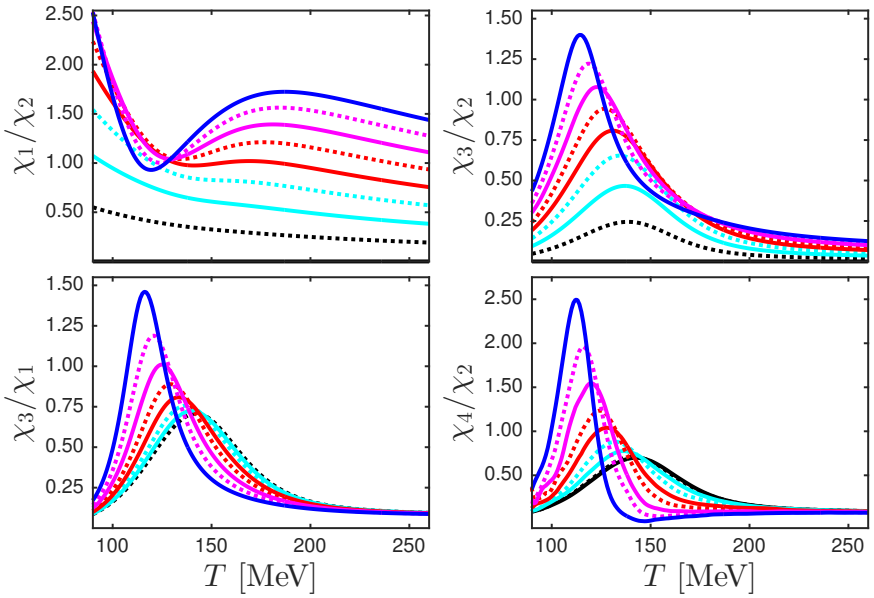

FIGURE 5.6: Susceptibility ratios, χ_1/χ_2 (upper left panel), χ_3/χ_1 (lower left panel), χ_3/χ_2 (upper right panel), and χ_4/χ_2 (lower right panel) obtained from EMD black hole model as function of T for different values of μ_B. Black solid(dashed) $\mu_B = 0$ ($\mu_B = 50$), cyan solid(dashed) $\mu_B = 100$ ($\mu_B = 150$), red solid(dashed) $\mu_B = 200$ ($\mu_B = 250$), magenta solid(dashed) $\mu_B = 300$ ($\mu_B = 350$), and blue solid $\mu_B = 400$.

5.3 Chemical Freeze-out

In HICs, the particle yields, and consequently, the distribution of particles are fixed at the chemical freeze-out (see Section 1.3.4). Therefore, the freeze-out parameters T and μ_B for a particular collision energy $\sqrt{s}$ can be extracted from comparing the particle yields in HICs with theoretical models. There are two common approaches to obtain the freeze-out variables. One is based on the Statistical Hadronization models (SHM) where the particle yields are compared with the corresponding ones in the

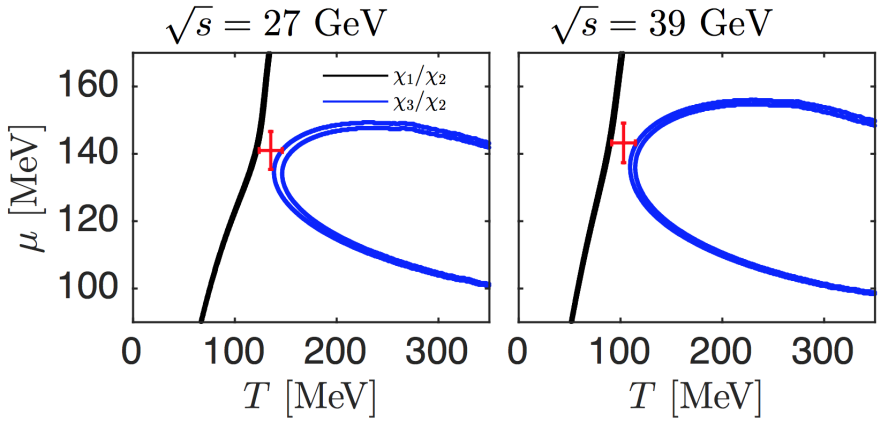

FIGURE 5.7: This figure shows the bands in the (T, μ)-plane expanded by the ratios in Eq. (5.4) computed in the Black Hole model that match the experimental values for the net-proton distribution at collision energies of $\sqrt{s} = 27$ GeV (left panel) and $\sqrt{s} = 39$ GeV (right panel) obtained by STAR [33]. It also shows with a red cross the extracted freeze-out parameter computed by finding the closest line between the trajectory of the two bands

HRG model [106–108]. The other one focused on the distribution of particles measured on an event-by-event basis in HICs. The moment of such distributions are directly related to the susceptibilities of the conserved charges [109, 110] as was specified in Eq. (1.23). For instance, by measuring the distribution of net-protons one can obtain a reasonable approximation for the distribution of net-baryons, and measuring the distribution of charged particles will provide the fluctuation of the electric charge. Thus, by comparing for example the ratio of mean over the variance M/σ^2 with the corresponding ratio of baryonic susceptibilities χ_1/χ_2 calculated in the HRG model, for both conserved charges, one has two equations to calculate the freeze-out parameters.This approach was used in [36] to obtain the freeze-out variables for collision energies $\sqrt{s} = \{7.7, 19.6, 27, 39, 64.2, 200\}$ GeV at STAR.

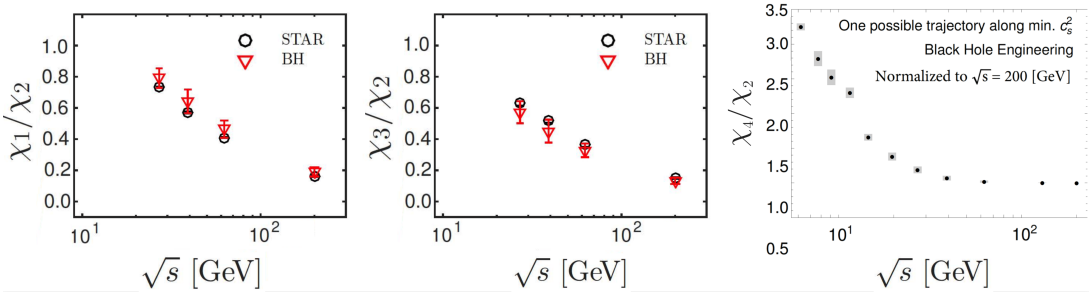

FIGURE 5.8
Collision energy dependence of susceptibilities ratio. χ_1/χ_2 (left panel) and χ_3/χ_2 (central panel) along the chemical freeze-out line computed using Black Hole model (red triangles) in comparison with the net-proton distribution from the STAR experiment [33] (red triangles) for $\sqrt{s} = \{27, 39, 62.4, 200\}$ MeV. χ_2/χ_4 (right panel) is also shown along the minimum of c_s^2 calculated in the Black Hole model. The ratio is normalized with its value at $\sqrt{s} = 200$ MeV

5.3.1 Freeze-out parameters from the Black Hole model.

The susceptibility ratios as functions of T are shown in Figure 5.6 for different values of μ_B in the range $\mu_B = \{0 - 400\}$ MeV. Since in the Black Hole model there is only one conserved charged, the baryonic charge, in order to extract freeze-out variables one needs to compare at least two of those ratios. The most appropriate choice, considering the statistical uncertainties in the measurements, is to use: χ_1/χ_2 and χ_3/χ_2, which are later compered with the corresponding relations for the moments of distribution of net-protons from STAR.

The comparison is shown in Figure 5.7 where the bands in the (T, μ)-plane are expanded by the ratios from Eq. (1.23)

$$\frac{M}{\sigma^2} = \frac{\chi_1}{\chi_2} \qquad S\sigma = \frac{\chi_3}{\chi_2} \tag{5.4}$$

computed in the Black Hole model that match the experimental values for the net-proton distribution at collision energies of $\sqrt{s} = 27$ GeV (left panel) and $\sqrt{s} = 39$ GeV

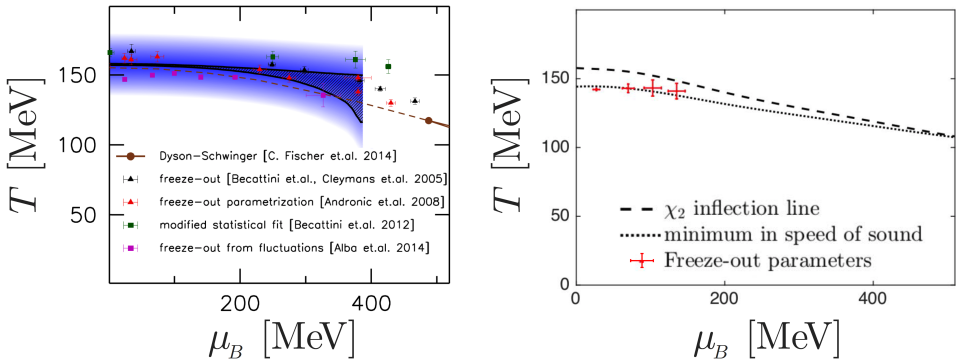

FIGURE 5.9: Comparison of the phase diagram obtained by lattice analysis and the one obtained by the Black Hole model. Left panel: the phase diagram from [74] based on the μ_B-dependent T_c from the chiral condensate, analytically continued from imaginary chemical potential. The blue band indicates the width of the transition. On top of the diagram are the Dyson-Schwinger result of [111] for the transition temperature, and the freeze-out variables from [36, 107, 112–116]. Right panel: the phase diagram obtained from the Black Hole model. The crossover transition is signaled by the inflection point of χ_2 (dashed curve) and the minimum in speed of sound squared c_s^2 (dotted curve). The red points indicate the freeze-out variables obtained in the Black Hole model.

(right panel) obtained by STAR [33]. The freeze-out variables for collision energy of $\sqrt{s} = 19.6$ GeV and lower are not consider in this analysis since at those energies the μ_B at freeze-out is large and the effect of strangeness and electric charge, which are not included in the Black Hole model, become important. Figure 5.7 shows that the areas spanned by the ratios do not overlap. To obtain the freeze-out variables, the closest line between the trajectory of the two bands is obtained, to span an area that becomes the freeze-out point shown in red with its error bar.

The extracted freeze-out points are compared with the measured susceptibilities as functions of the collision energy $\sqrt{s}$ in Figure 5.8. The left panel shows χ_1/χ_2 and the central panel χ_3/χ_2. The black circles are the measured ratios and the extracted points are shown as red triangles. By construction they both agrees within error bars.

Those two ratios were the only ones used to extract the freeze-out parameter. On the right panel, a prediction for the ratio χ_4/χ_2 along the minimum of the speed of sound squared c_s^2 is shown. This ratio follows the trend of the experimental data at low $\sqrt{s}$, however, for this particular trajectory the ratio has a monotonic behavior. It is expected, based on universality arguments, that a freeze-out trajectory sufficiently close to the CEP will show a non-monotonic behavior in the ratio χ_4/χ_2 [39]. This did not happened for the the trajectory along c_s^2. What was found with the Black Hole model is that a non-monotonic behavior can be observed along a curved freeze-out trajectory when it is not close to the CEP. Therefore, it is not possible to prove or disprove the statement at the moment, with the results that were computed for this work.

The freeze-out parameters obtained with the Black Hole model are placed along the crossover transition line. Figure 5.9 shows a comparison of the phase diagram obtained by lattice analysis, in the left panel, and the phase diagram obtained by the Black Hole model, in the right panel. The phase diagram obtained by lattice calculations in [74] is based on the μ_B-dependent T_c from the chiral condensate, analytically continued from imaginary chemical potential. The blue band indicates the width of the transition. On top of the diagram are the Dyson-Schwinger result, of [111] for the transition temperature, and the freeze-out variables from [36, 107, 112–116]. On the other hand, to signal the crossover transition in the Black Hole model, it is necessary to identify observables sensitive to a change in the relevant degrees of freedom of the system from hadrons to quarks and gluons. In the holographic phase diagram, the crossover is marked by the inflection point of χ_2 and the minimum in the speed of sound squared c_s^2, which are shown with a dotted curve and a dashed curve respectively. The red points in the diagram indicate the freeze-out variables obtained in the Black Hole model.

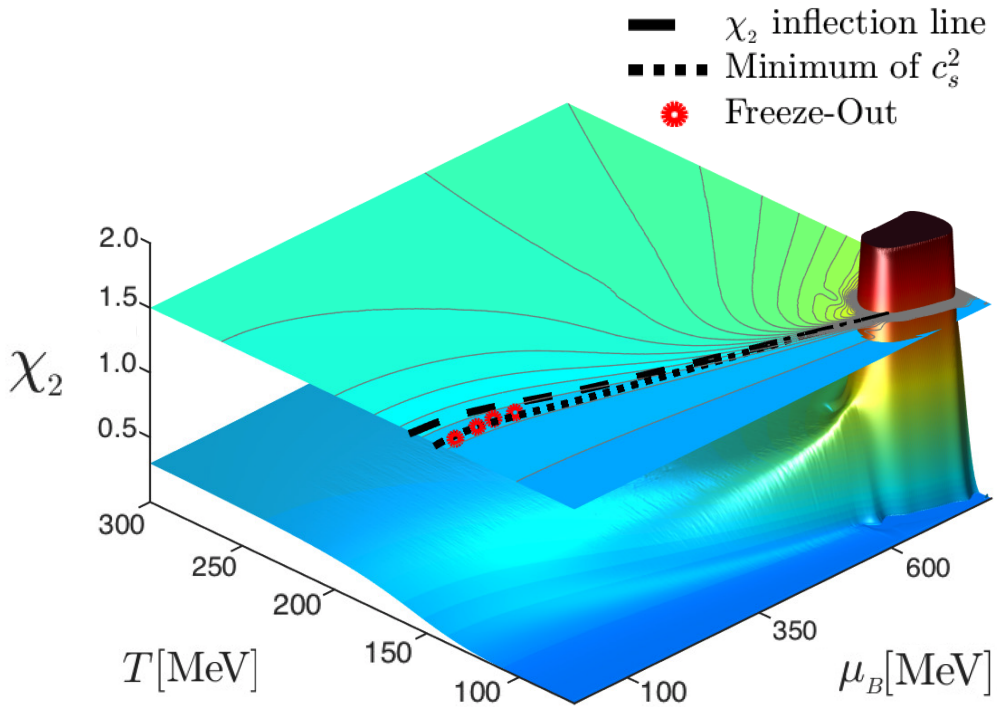

FIGURE 5.10: This figure shows the behavior of the baryon susceptibility χ_2 in the QCD phase diagram obtained with the Black Hole model. The susceptibility increases approaching the CEP located at $T_{\text{CEP}} = 89$ MeV and $\mu_B^{\text{CEP}} = 724$ MeV, developing a peak that diverges at the CEP. On top of the plot, there is a plane that shows the contour lines of χ_2, and the transition line signaled by the inflection point of χ_2 (dashed curve) and the minimum of c_s^2 (dotted curve). Those two lines meet at the critical point where χ_2 diverges and c_s^2 becomes zero. The Freeze-out points extracted in the Black Hole model are shown on the plane with red circles.

5.4 QCD Critical end Point

The CEP and the line of first order phase transition was located by analyzing the behavior of the entropy and the baryon density obtained in the the Black Hole model, as was explained in Section 4.3.1. The holographic phase diagram up to the CEP is shown in Figure 5.10. The figure displays the behavior of the baryon susceptibility χ_2 obtained

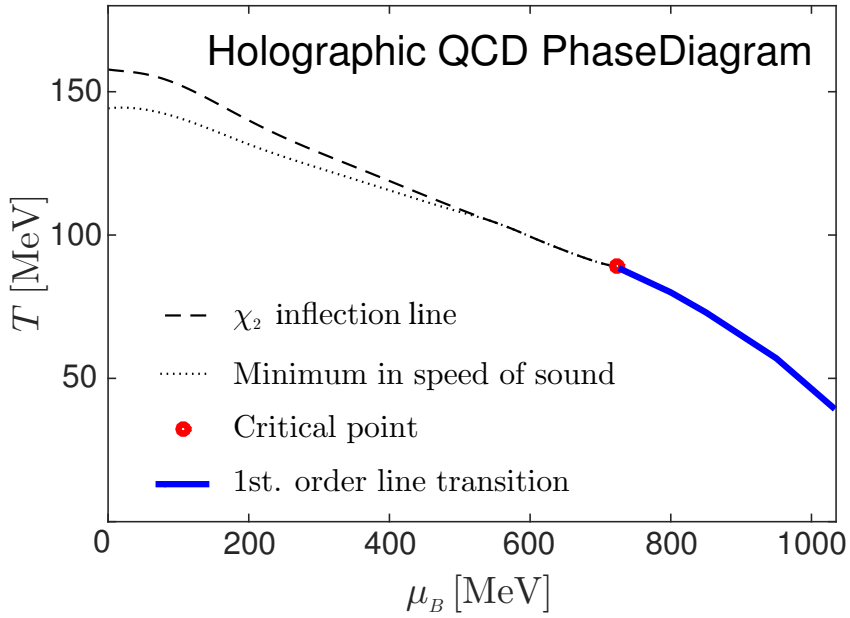

FIGURE 5.11: QCD Phase diagram obtained from the Black Hole model. The crossover is signaled by two observables: the inflection point of χ_2 (dashed curve) and the minimum in c_s^2 (dotted curve). The CEP is shown with a red dot. An estimate for the first order phase transition is shown as a blue curve.

with the Black Hole model. One can see that the susceptibility increases approaching the CEP, located at $T_{\text{CEP}} = 89\,\text{MeV}$ and $\mu_B^{\text{CEP}} = 724\,\text{MeV}$, thus developing a peak that diverges at the CEP. On top of the plot, there is a plane that shows the contour lines of χ_2 together with the transition line signalized by the inflection point of χ_2 (dashed curve) and the minimum of c_s^2 (doted curve). Those two lines meet at the CEP where χ_2 diverges and c_s^2 becomes zero.

The holographic QCD phase diagram, extended to $\mu_B = 1000\,\text{MeV}$, is shown in Figure 5.11. This figure shows once again the crossover illustrated by the inflection point of χ_2 (dashed curve) and the minimum in c_s^2 (dotted curve). The CEP is shown with a red dot, and the first order phase transition line with a blue curve.

5.4.1 Exclusion plot

This sections shows a phase diagram in Figure 5.12 that includes the CEP obtained with the Black Hole model. In this case, the error bars on the location of the CEP are the product of a more detailed investigation that takes into account the effect of uncertainties in the lattice points used to fix the model parameters, as was explained in Section 4.3. As a result, the holographic CEP obtained in this dissertation is located at $T_{\rm CEP} = 89 \pm 11$ MeV and $\mu_B^{\rm CEP} = 724 \pm 36$ MeV. The critical point is located along the line $\mu_B/T \sim 8.1$ in the phase diagram, which is beyond the reach of current lattice QCD calculations where $\mu_B/T \lesssim 2$ [20, 21].

Figure 5.12 also shows the region of the QCD phase diagram that has been excluded by current analyses. The current lattice QCD constraints [20] exclude the dark blue region, while the green region is unlikely due to the negative curvature of the QCD transition line [74]. A finite-size scaling analysis [117] has exclude the light blue region. This plot illustrates that the position of the holographic CEP is in a region of the QCD phase diagram that is still open for exploration.

5.4.2 Collision Energy at the Critical end Point

This section combine most of the previous analysis using the Black Hole model to give an estimate of the collision energy needed to hit the CEP in HICs. Figure 5.13 shows the collision energy dependence of the freeze-out chemical potential $\mu_B(\sqrt{s})$ in the left panel, and temperature $T(\sqrt{s})$ in the right panel.

The left panel of Figure 5.13 displays in purple squares the freeze-out points extracted using the susceptibilities calculated within the HRG model [36]. The red triangles are the freeze-out points obtained with the Black Hole model. The solid black curve

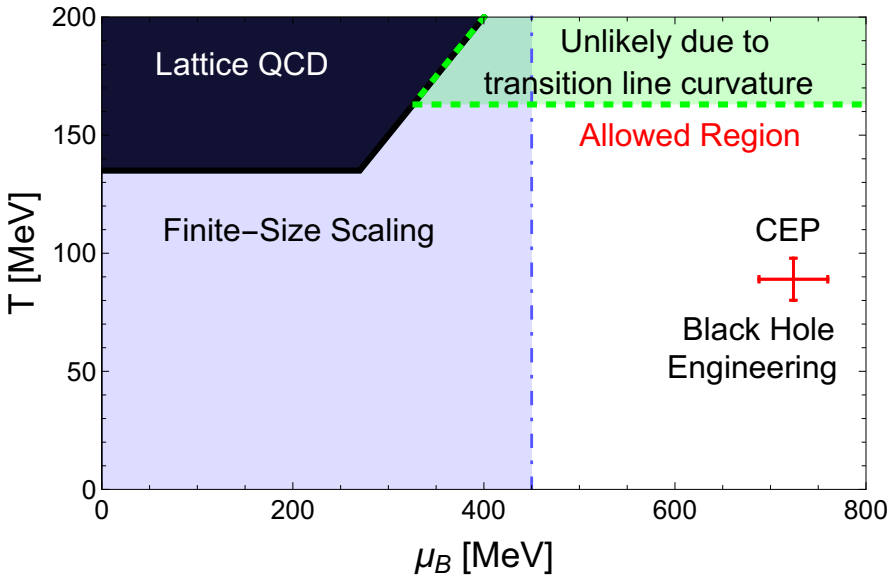

FIGURE 5.12: This figure shows the regions in the QCD phase diagram where the presence of a CEP has been excluded by: (dark blue) current lattice QCD constraints [20], (light blue) finite-size scaling analysis [117], and (green) the negative curvature of the QCD transition line, which made this region unlikely [74]. It also shows (red point) the location of our CEP. The error bars are obtained by combining the three different model parameters studied in this work.

was obtained from the parametrization using the statistical hadronization model calculations obtained in [107] (SHM1), and the dashed grey curve from [108] (SHM2). One can see that the freeze-out points from the HRG model and the Black Hole model are compatible with the results from the statistical hadronization models. Those parametrization are extrapolated to lower energies to find the red band that represent the μ_B range of the CEP. Note that SHM1 is almost identical to SHM2.

In the right panel of Figure 5.13, the $T(\sqrt{s})$ is shown for the parametrization of SHM1 and SHM2. It also shows the minimum of the speed of sound squared c_s^2 along

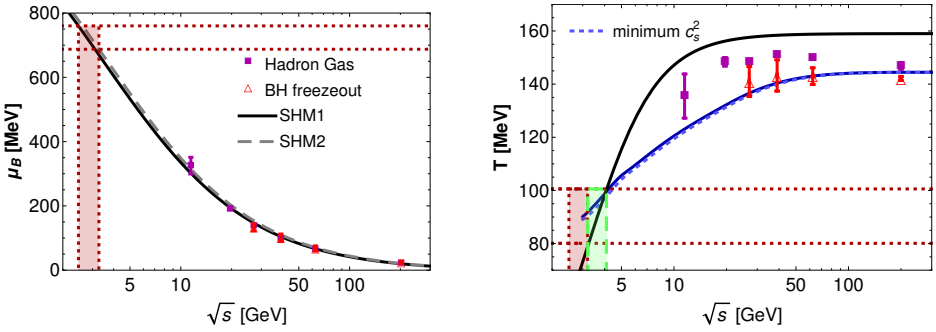

FIGURE 5.13: Collision energy dependence of μ_B (left panel) and T (right panel) at the chemical freeze-out as a function of the energy of the colliding beam $\sqrt{s}$. The solid black curve was obtained from the parametrization using the statistical hadronization model calculations obtained in [107] (SHM1), and the dashed grey curve from [108] (SHM2). The blue curves show the trajectory in the phase diagram that follows the minimum of c_s^2 using the parametrization in SHM1 (solid curve) and SHM2 (solid-dashed curve). The purple square points were obtained by comparing the net-proton and net-electric charge fluctuations using the HRG model in [36]. The red triangles represent the chemical freeze-out points extracted with the EMD black hole model by comparing the susceptibility ratios χ_1/χ_2 and χ_3/χ_2 with the corresponding net-proton experimental data from STAR [33]. The bands are used to find the value of $\sqrt{s}$ corresponding to the CEP, including the combined effect from uncertainties coming from both parametrizations ($T(\sqrt{s})$, and $\mu_B(\sqrt{s})$) and the error bars in the location of the CEP by the holographic model.

the $\mu_B(\sqrt{s})$ parametrization obtained in the left panel. As mentioned before, the freeze-out points are expected to be close to the transition temperature and c_s^2 gives an estimate of the region of the crossover. The freeze-out points for both the HRG model and Black Hole model lie in between the parametrization of SHM1, SHM2, and the c_s^2. Then, the three parametrizations are extrapolated to lower energies to meet the green area that represents the T range within the uncertainties of the holographic CEP.

By combining both uncertainties, the red region from the $\mu_B(\sqrt{s})$ dependence and the green region from the $T(\sqrt{s})$ dependence, it was found that the collision energy needed to hit the CEP is in the range $\sqrt{s} = \{2.5 - 4.1\}$ GeV. These collision energies

are below the current plans for the second run of the BES in collider mode, but they are within the reach of the HADES experiment [118], the planned Fixed Target (FXT) program also at RHIC [31], and the future Compressed Baryonic Matter (CBM) experiment at FAIR [32].

Chapter 6

Concluding Remarks

The investigation presented in this dissertation has been focused on the study of the QCD phase diagram at finite T and μ_B. The precise mapping of those phases is one of the biggest challenges in theoretical physics. At high temperature or densities, the running of the coupling constant of QCD will produce the deconfinement of hadrons into a QGP state. The change of degrees of freedom from hadrons to quarks and gluons is a non-perturbative phenomenon that can only be addressed from first principles by means of lattice simulations.

Thanks to lattice calculations, the QCD EoS is known with great precision at zero μ_B. It predicts that the transition from hadrons to deconfined quarks and gluons is a smooth crossover taking place in the temperature range $T \simeq 145 - 165$ MeV [4–9]. It is believed that this crossover sharpens at finite μ_B into a CEP, where a line of first order phase transitions begins. The position of the CEP that terminates this line is of considerable interest, especially with the forthcoming second Beam Energy Scan at RHIC, scheduled for 2019-2020, the next fixed-target CMB project at FAIR, which is presently under construction at GSI in Germany, and the NICA facility operating in Russia. Those machines are dedicated to explore on unprecedented high density region

of the QCD phase diagram, where the CEP could be located. However, it is hard to determine theoretically if QCD displays critical phenomena at large μ_B because the QCD coupling constant is strong, and moreover, lattice simulations cannot be performed at finite density due to the sign problem. As a result, the QCD phase diagram is mostly unexplored at finite chemical potential.

In the effort to constraint the location of the CEP using lattice calculations, this dissertation devotes special attention to the baryonic susceptibilities. These observables are of great interest because they can be used to Taylor expand the pressure calculated on the lattice at $\mu_B = 0$ to a finite density region of the QCD phase diagram in powers of μ_B/T [10–14]. They also allow one to make a direct connection with the moment of distribution of the baryonic charge measured in HICs. Thus, a comparison between theoretical and experimental results allows to extract the chemical freeze-out parameters as functions of the collision energy [21, 34, 35, 119, 120]. In the search for the CEP, the susceptibilities are sensitive to the location of the CEP since they are proportional to powers of the correlation length, which diverges at the CEP, and may provide a signature for its experimental detection [38]. The first part of this dissertation was dedicated to compute higher order baryon susceptibilities from the lower order ones calculated at imaginary-μ_B.

Moreover, in the absence of lattice calculations at finite μ_B, effective approaches must be used to guide the experimental search for the CEP in HICs. The alternative approach used in the second part of this dissertation is based on the holographic correspondence developed in string theory [40]. The holographic model intrinsically contains an important feature of the strongly coupled QGP, which is the small value obtained for the ratio between the shear viscosity and the entropy density. The gauge/gravity correspondence with at most two derivatives in the gravitational action predicts a value

of $\eta/s = 1/4\pi$ [51–53], which is remarkably close to estimates obtained from comparisons between hydrodynamic simulations of the QGP and heavy-ion data [121]. Then, using the holographic gauge/gravity duality, the baryonic susceptibilities in the dense and strongly coupled QGP were mapped onto a numerically tractable gravitational problem involving the charge fluctuations of holographic black holes.

6.1 High Order Susceptibilities from Lattice QCD

Chapter 3 of this dissertation was devoted to analyzing the lower order baryonic susceptibilities simulated at imaginary-μ_B to calculate the higher order ones at zero μ_B. The lower-order baryonic susceptibilities were calculated at imaginary-μ_B in the temperature range 135 MeV $\leq T \leq$ 220 MeV, for a system of $2+1+1$ dynamical quarks with physical masses and lattice size $48^3 \times 12$. A combined fit of the first four baryonic susceptibilities (χ_1, χ_2, χ_3, χ_4) was done in order to obtain χ_6 and a good estimate for χ_8 [23].

In a previous calculation [20], χ_6 in the continuum limit was obtained using a direct evaluation at $\mu_B = 0$. Direct methods are affected by a signal-to-noise ratio with an exponent that grows with the order of the susceptibility and consequently the uncertainty on χ_6 was large. On the other hand, the analysis that was done here with the data simulated at imaginary-μ_B at small lattice spacing provide not only a stable χ_6 but also an estimate for χ_8.

The Taylor expansion of the EoS with the baryonic susceptibilities up to $\mathcal{O}(\mu_B^6)$ was shown in [20] to provide a good approximation for a ratio $\mu_B/T \leq 2$. This ratio is not enough to have access to the regions that will be explored during the second run of the BES, where $\mu_B/T \sim 3$. In this case, higher order susceptibilities are needed. Once χ_8 is

refined by a further analysis with more precise lattice calculations, the ratio $\mu_B/T \sim 3$ may be reach.

6.2 Holographic Model

The calculation with the holographic model described in Chapter 4 is not limited by the μ_B, and can be used to span the whole QCD phase diagram. In principle, the model is limited to the strongly coupled regime of the corresponding gauge theory. However, the scalar dilaton potential $V(\phi)$ and the Maxwell-dilaton coupling $f(\phi)$ were not obtained directly from the holographic correspondence, but were constructed to mimic the EoS from the lattice at $\mu_B = 0$. Thus, the holographic EoS at finite μ_B is a prediction of the holographic model, and the quantitative agreement found in Figure 5.2 and Figure 5.4 with the available lattice calculations for $\mu_B/T \leq 2$ is a highly nontrivial test of the phenomenological applicability of the Black Hole model to describe QCD data far from the region of the phase diagram where the free parameters of the model were fixed. The model also predicted χ_6 and χ_8, for which the behavior of the lattice results was reproduced as shown in Figure 5.3.

Notice that the general form of the EMD action used in this dissertation was first presented in [89], where now outdated lattice results for the entropy and baryon susceptibility [122] were used in the determination of the functions $V(\phi)$ and $f(\phi)$. In [93] a new version of the Black Hole model was constructed which, contrary to the one originally devised in [89], does not introduce any additional free parameters in the holographic model besides the ones already featured in the EMD action, making it a self-consistent gravitational setup. Furthermore, more recent lattice QCD results for the entropy and baryon susceptibility [98, 104] were used to fix the model parameters. The new version of the Black Hole model [24] studied in this dissertation provides

a much more precise description of thermodynamical quantities in comparison with lattice results at $\mu_B = 0$.

The main result of the analysis with the Black Hole model is the prediction of the existence of a CEP on the QCD phase diagram located at $T_{\rm CEP} = 89\,\mathrm{MeV}$ and $\mu_B^{\rm CEP} = 724\,\mathrm{MeV}$. Moreover, by analyzing the ratio of susceptibilities computed at finite μ_B, freeze-out parameters for the net-proton distribution from the STAR experiment [33] were obtained. Then through a consistent analysis of the behavior of the freeze-out obtained by the holographic model, and parametrizations obtained in the context of SHM (see Figure 5.13), the collision energy needed to hit the CEP in HICs was estimated in the range $\sqrt{s} = \{2.5 - 4.1\}\,\mathrm{GeV}$. These collision energies are below the threshold of the BES at RHIC operating in collider mode (where the minimum is $\sqrt{s} = 7.7\,\mathrm{GeV}$) but they are within the reach of the HADES experiment [118], the planned Fixed Target (FXT) program also at RHIC [31], and the future Compressed Baryonic Matter (CBM) experiment at FAIR [32].

Bibliography

[1] S. Weinberg. *"The quantum theory of fields"*. Vol. [1-3]. Cambridge University Press, 1995.

[2] D. J. Gross and F. Wilczek. "Asymptotically free gauge theories - I". *Phys. Rev.* D8 (1973), 3633–3652.

[3] D. J. Gross and F. Wilczek. "Asymptotically free gauge theories -II". *Phys. Rev.* D9 (1974), 980–993.

[4] Y. Aoki, G. Endrodi, Z. Fodor, S. D. Katz, et al. "The order of the quantum chromodynamics transition predicted by the standard model of particle physics". *Nature* 443 (2006), 675–678.

[5] Y. Aoki, Z. Fodor, S. D. Katz, and K. K. Szabo. "The QCD transition temperature: results with physical masses in the continuum limit". *Phys. Lett.* B643 (2006), 46–54.

[6] Y. Aoki, S. Borsanyi, S. Durr, Z. Fodor, et al. "The QCD transition temperature: Results with physical masses in the continuum limit II." *JHEP* 06 (2009), 088.

[7] S. Borsanyi, Z. Fodor, C. Hoelbling, S. D. Katz, et al. "Is there still any T_c mystery in lattice QCD? Results with physical masses in the continuum limit III". *JHEP* 09 (2010), 073.

[8] T. Bhattacharya, M. I. Buchoff, N. H. Christ, H. T. Ding, et al. "QCD phase transition with chiral quarks and physical quark masses". *Phys. Rev. Lett.* 113 (2014), 082001.

[9] A. Bazavov, T. Bhattacharya, M. Cheng, C. DeTar, et al. "The chiral and deconfinement aspects of the QCD transition". *Phys. Rev.* D85 (2012), 054503.

[10] C. R. Allton, S. Ejiri, S. J. Hands, O. Kaczmarek, et al. "The QCD thermal phase transition in the presence of a small chemical potential". *Phys. Rev.* D66 (2002), 074507.

[11] C. R. Allton, M. Doring, S. Ejiri, S. J. Hands, et al. "Thermodynamics of two flavor QCD to sixth order in quark chemical potential". *Phys. Rev.* D71 (2005), 054508.

[12] R. V. Gavai and S. Gupta. "QCD at finite chemical potential with six time slices". *Phys. Rev.* D78 (2008), 114503.

[13] S. Basak, A. Bazavov, C. Bernard, C. DeTar, et al. "QCD equation of state at non-zero chemical potential". *Proceedings, 26th International Symposium on Lattice field theory*. *PoS* Lattice2008, (2008), 171.

[14] O. Kaczmarek, F. Karsch, E. Laermann, C. Miao, et al. "Phase boundary for the chiral transition in (2+1) -flavor QCD at small values of the chemical potential". *Phys. Rev.* D83 (2011), 014504.

[15] Z. Fodor and S. D. Katz. "A new method to study lattice QCD at finite temperature and chemical potential". *Phys. Lett.* B534 (2002), 87–92.

[16] P. de Forcrand and O. Philipsen. "The QCD phase diagram for small densities from imaginary chemical potential". *Nucl. Phys.* B642 (2002), 290–306.

[17] M. D'Elia and M. P. Lombardo. "Finite density QCD via imaginary chemical potential". *Phys. Rev.* D67 (2003), 014505.

[18] Z. Fodor and S. D. Katz. "Lattice determination of the critical point of QCD at finite T and μ". *JHEP* 03 (2002), 014.

[19] Z. Fodor and S. D. Katz. "Critical point of QCD at finite T and μ, lattice results for physical quark masses". *JHEP* 04 (2004), 050.

[20] A. Bazavov, H. T. Ding, P. Hegde, O. Kaczmarek, et al. "The QCD equation of state to $\mathcal{O}(\mu_B^6)$ from lattice QCD". *Phys. Rev.* D95 (2017), 054504.

[21] C. Ratti. "Lattice QCD and heavy ion collisions: a review of recent progress". *Rept. Prog. Phys.* 81 (2018), 084301.

[22] M. A. Stephanov, K. Rajagopal, and E. V. Shuryak. "Signatures of the tricritical point in QCD". *Phys. Rev. Lett.* 81 (1998), 4816–4819.

[23] S. Borsanyi, Z. Fodor, J. N. Guenther, S. K. Katz, et al. "Higher order fluctuations and correlations of conserved charges from lattice QCD". *JHEP* 10 (2018), 205.

[24] R. Critelli, J. Noronha, J. Noronha-Hostler, I. Portillo, et al. "Critical point in the phase diagram of primordial quark-gluon matter from black hole physics". *Phys. Rev.* D96 (2017), 096026.

[25] M. Tanabashi, K. Hagiwara, K. Hikasa, K. Nakamura, et al. "Review of particle physics". *Phys. Rev.* D98 (2018), 030001.

[26] S. Bethke. "Experimental tests of asymptotic freedom". *Prog. Part. Nucl. Phys.* 58 (2007), 351–386.

[27] A. Bazavov, T. Bhattacharya, C. DeTar, H. T. Ding, et al. "Equation of state in (2+1)-flavor QCD". *Phys. Rev.* D90 (2014), 094503.

[28] S. Borsanyi, Z. Fodor, C. Hoelbling, S. D. Katz, et al. "Full result for the QCD equation of state with 2+1 flavors". *Phys. Lett.* B730 (2014), 99–104.

[29] M. Huang and I. A. Shovkovy. "Chromomagnetic instability in dense quark matter". *Phys. Rev.* D70 (2004), 051501.

[30] S. Mogliacci, J. O. Andersen, M Strickland, N. Su, et al. "Equation of state of hot and dense QCD: Resummed perturbation theory confronts lattice data". *JHEP* 12 (2013), 055.

[31] K. Meehan. "STAR Results from Au + Au Fixed-Target Collisions at $\sqrt{s_{NN}} =$ 4.5 GeV". *Proceedings, 26th International Conference on Ultra-relativistic Nucleus-Nucleus Collisions (QM 2017). Nucl. Phys.* A967, (2017), 808–811.

[32] T. Ablyazimov, A. Abuhoza, R. P. Adak, M. Adamczyk, et al. "Challenges in QCD matter physics –The scientific programme of the Compressed Baryonic Matter experiment at FAIR". *Eur. Phys. J.* A53 (2017), 60.

[33] L. Adamczyk, J. K. Adkins, G. Agakishiev, M. M. Aggarwal, et al. "Energy dependence of moments of net-proton multiplicity distributions at RHIC". *Phys. Rev. Lett.* 112 (2014), 032302.

[34] F. Karsch. "Determination of freeze-out conditions from lattice QCD calculations". *7th International Workshop on Critical Point and Onset of Deconfinement (CPOD 2011). Central Eur. J. Phys.* 10, (2012), 1234–1237.

[35] S. Borsanyi, Z. Fodor, S. D. Katz, S. Krieg, et al. "Freeze-out parameters from electric charge and baryon number fluctuations: is there consistency?" *Phys. Rev. Lett.* 113 (2014), 052301.

[36] P. Alba, W. Alberico, R. Bellwied, M. Bluhm, et al. "Freeze-out conditions from net-proton and net-charge fluctuations at RHIC". *Phys. Lett.* B738 (2014), 305–310.

[37] J. Noronha-Hostler, R. Bellwied, J. Gunther, P. Parotto, et al. "Kaon fluctuations from lattice QCD" (2016). submitted to *Phys. Rev. Lett.* arXiv: 1607.02527.

[38] M. A. Stephanov. "Non-Gaussian fluctuations near the QCD critical point". *Phys. Rev. Lett.* 102 (2009), 032301.

[39] M. A. Stephanov. "On the sign of kurtosis near the QCD critical point". *Phys. Rev. Lett.* 107 (2011), 052301.

[40] J. M. Maldacena. "The large N limit of superconformal field theories and supergravity". *Int. J. Theor. Phys.* 38 (1999), 1113–1133.

[41] S. S. Gubser, I. R. Klebanov, and A. M. Polyakov. "Gauge theory correlators from noncritical string theory". *Phys. Lett.* B428 (1998), 105–114.

[42] E. Witten. "Anti-de Sitter space and holography". *Adv. Theor. Math. Phys.* 2 (1998), 253–291.

[43] E. Witten. "Anti-de-Sitter space, thermal phase transition, and confinement in gauge theories". *Adv. Theor. Math. Phys.* 2 (1998), 505–532.

[44] J Casalderrey-Solana, H. Liu, D. Mateos, K. Rajagopal, et al. *Gauge/String Duality, Hot QCD and Heavy Ion Collisions*. Cambridge University Press, 2014.

[45] A. Adams, L. D. Carr, T. Schafer, P. Steinberg, et al. "Strongly correlated quantum fluids: ultracold quantum gases, quantum chromodynamic plasmas, and holographic duality". *New J. Phys.* 14 (2012), 115009.

[46] A. Donos and S. A. Hartnoll. "Interaction-driven localization in holography". *Nature Phys.* 9 (2013), 649–655.

[47] S. A. Hartnoll. "Theory of universal incoherent metallic transport". *Nature Phys.* 11 (2015), 54.

[48] S. Sachdev. "What can gauge-gravity duality teach us about condensed matter physics?" *Ann. Rev. Condensed Matter Phys.* 3 (2012), 9–33.

[49] T. Nishioka, S. Ryu, and T. Takayanagi. "Holographic entanglement entropy: An overview". *J. Phys.* A42 (2009), 504008.

[50] J. Maldacena and L. Susskind. "Cool horizons for entangled black holes". *Fortsch. Phys.* 61 (2013), 781–811.

[51] G. Policastro, D. T. Son, and A. O. Starinets. "The Shear viscosity of strongly coupled N=4 supersymmetric Yang-Mills plasma". *Phys. Rev. Lett.* 87 (2001), 081601.

[52] A. Buchel and J. T. Liu. "Universality of the shear viscosity in supergravity". *Phys. Rev. Lett.* 93 (2004), 090602.

[53] P. Kovtun, D. T. Son, and A. O. Starinets. "Viscosity in strongly interacting quantum field theories from black hole physics". *Phys. Rev. Lett.* 94 (2005), 111601.

[54] M. Gyulassy and L. McLerran. "New forms of QCD matter discovered at RHIC". *Quark gluon plasma. New discoveries at RHIC: A case of strongly interacting quark gluon plasma. Nucl. Phys.* A750, (2005), 30–63.

[55] I. Arsene, I.G. Bearden, D. Beavis, C. Besliu, et al. "Quark gluon plasma and color glass condensate at RHIC? The Perspective from the BRAHMS experiment". *Nucl. Phys.* A757 (2005), 1–27.

[56] K. Adcox, S.S. Adler, S. Afanasiev, C. Aidala, et al. "Formation of dense partonic matter in relativistic nucleus-nucleus collisions at RHIC: Experimental evaluation by the PHENIX collaboration". *Nucl. Phys.* A757 (2005), 184–283.

[57] B. B. Back, M.D. Baker, M. Ballintijn, D.S. Barton, et al. "The PHOBOS perspective on discoveries at RHIC". *Nucl. Phys.* A757 (2005), 28–101.

[58] J. Adams, M.M. Aggarwal, Z. Ahammed, J. Amonett, et al. "Experimental and theoretical challenges in the search for the quark gluon plasma: The STAR Collaboration's critical assessment of the evidence from RHIC collisions". *Nucl. Phys.* A757 (2005), 102–183.

[59] G. Aad, T. Abajyan, B. Abbott, J. Abdallah, et al. "Measurement of the distributions of event-by-event flow harmonics in lead-lead collisions at $\sqrt{s_{NN}} = 2.76$ TeV with the ATLAS detector at the LHC". *JHEP* 11 (2013), 183.

[60] U. Heinz and R. Snellings. "Collective flow and viscosity in relativistic heavy-ion collisions". *Ann. Rev. Nucl. Part. Sci.* 63 (2013), 123–151.

[61] E. Shuryak. "Strongly coupled quark-gluon plasma in heavy ion collisions". *Rev. Mod. Phys.* 89 (2017), 035001.

[62] K. G. Wilson. "Confinement of quarks". *Phys. Rev.* D10 (1974), 2445–2459.

[63] M. Luscher and P. Weisz. "Computation of the action for on-shell improved lattice gauge theories at weak coupling". *Phys. Lett.* 158B (1985), 250–254.

[64] K. Symanzik. "Continuum limit and improved action in lattice theories. 1. Principles and phi**4 theory". *Nucl. Phys.* B226 (1983), 187–204.

[65] K. Symanzik. "Continuum limit and improved action in lattice theories. 2. O(N) nonlinear sigma model in perturbation theory". *Nucl. Phys.* B226 (1983), 205–227.

[66] J. B. Kogut and L. Susskind. "Hamiltonian formulation of Wilson's lattice gauge theories". *Phys. Rev.* D11 (1975), 395–408.

[67] C. Gattringer and C. B. Lang. "Quantum chromodynamics on the lattice". *Lect. Notes Phys.* 788 (2010), 1–343.

[68] B. Sheikholeslami and R. Wohlert. "Improved continuum limit lattice action for QCD with Wilson fermions". *Nucl. Phys.* B259 (1985), 572.

[69] P. Hasenfratz and F. Karsch. "Chemical potential on the lattice". *Phys. Lett.* 125B (1983), 308–310.

[70] A. Roberge and N. Weiss. "Gauge theories with imaginary chemical potential and the phases of QCD". *Nucl. Phys.* B275 (1986), 734–745.

[71] C. Czaban, F. Cuteri, O. Philipsen, C. Pinke, et al. "Roberge-Weiss transition in $N_{\mathrm{f}} = 2$ QCD with Wilson fermions and $N_\tau = 6$". *Phys. Rev.* D93 (2016), 054507.

[72] P. de Forcrand and O. Philipsen. "Constraining the QCD phase diagram by tricritical lines at imaginary chemical potential". *Phys. Rev. Lett.* 105 (2010), 152001.

[73] C. Bonati, M. D'Elia, M. Mariti, M. Mesiti, et al. "Curvature of the chiral pseudocritical line in QCD: Continuum extrapolated results". *Phys. Rev.* D92 (2015), 054503.

[74] R. Bellwied, S. Borsanyi, Z. Fodor, J. Gunther, et al. "The QCD phase diagram from analytic continuation". *Phys. Lett.* B751 (2015), 559–564.

[75] P. Cea, L. Cosmai, and A. Papa. "Critical line of 2+1 flavor QCD: Toward the continuum limit". *Phys. Rev.* D93 (2016), 014507.

[76] J. N. Guenther, R. Bellwied, S. Borsanyi, Z. Fodor, et al. "The QCD equation of state at finite density from analytical continuation". *Proceedings, 26th International Conference on Ultra-relativistic Nucleus-Nucleus Collisions (QM 2017). Nucl. Phys.* A967, (2017), 720–723.

[77] M. D'Elia, G. Gagliardi, and F. Sanfilippo. "Higher order quark number fluctuations via imaginary chemical potentials in $N_f = 2 + 1$ QCD". *Phys. Rev.* D95 (2017), 094503.

[78] C. Bernard, T. Burch, E. B. Gregory, D. Toussaint, et al. "QCD thermodynamics with three flavors of improved staggered quarks". *Phys. Rev.* D71 (2005), 034504.

[79] A. Bazavov, T. Bhattacharya, C. E. DeTar, H. T. Ding, et al. "Fluctuations and correlations of net baryon number, electric charge, and strangeness: A comparison of lattice QCD results with the hadron resonance gas model". *Phys. Rev.* D86 (2012), 034509.

[80] R. Bellwied, S. Borsanyi, Z. Fodor, S. D. Katz, et al. "Fluctuations and correlations in high temperature QCD". *Phys. Rev.* D92 (2015), 114505.

[81] C. Morningstar and M. J. Peardon. "Analytic smearing of SU(3) link variables in lattice QCD". *Phys. Rev.* D69 (2004), 054501.

[82] C. T. H. Davies, C. McNeile, K. Y. Wong, E. Follana, et al. "Precise Charm to Strange Mass Ratio and Light Quark Masses from Full Lattice QCD". *Phys. Rev. Lett.* 104 (2010), 132003.

[83] S. Aoki, Y. Aoki, C. Bernard, T. Blum, et al. "Review of lattice results concerning low-energy particle physics". *Eur. Phys. J.* C74 (2014), 2890.

[84] J. L. Rosner and S. Stone. "Leptonic Decays of Charged Pseudoscalar Mesons - 2013" (2013). arXiv: 1309.1924.

[85] C. Bonati, M. D'Elia, F. Negro, F. Sanfilippo, et al. "Curvature of the pseudocritical line in QCD: Taylor expansion matches analytic continuation". *Phys. Rev.* D98 (2018), 054510.

[86] N. Haque, J. O. Andersen, M. G. Mustafa, M. Strickland, et al. "Three-loop pressure and susceptibility at finite temperature and density from hard-thermal-loop perturbation theory". *Phys. Rev.* D89 (2014), 061701.

[87] N. Haque, A. Bandyopadhyay, J. O. Andersen, M. G. Mustafa, et al. "Three-loop HTLpt thermodynamics at finite temperature and chemical potential". *JHEP* 05 (2014), 027.

[88] H. T. Ding, S. Mukherjee, H. Ohno, P. Petreczky, et al. "Diagonal and off-diagonal quark number susceptibilities at high temperatures". *Phys. Rev.* D92 (2015), 074043.

[89] O. DeWolfe, S. S. Gubser, and C. Rosen. "A holographic critical point". *Phys. Rev.* D83 (2011), 086005.

[90] J. D. Bekenstein. "Black holes and entropy". *Phys. Rev.* D7 (1973), 2333–2346.

[91] S. W. Hawking. "Particle creation by black holes". *Commun. Math. Phys.* 43 (1975), 199–220.

[92] S. S. Gubser and A. Nellore. "Mimicking the QCD equation of state with a dual black hole". *Phys. Rev.* D78 (2008), 086007.

[93] R. Rougemont, A. Ficnar, S. Finazzo, and J. Noronha. "Energy loss, equilibration, and thermodynamics of a baryon rich strongly coupled quark-gluon plasma". *JHEP* 04 (2016), 102.

[94] P. Breitenlohner and D. Z. Freedman. "Positive energy in Anti-de-Sitter backgrounds and gauged extended supergravity". *Phys. Lett.* 115B (1982), 197–201.

[95] P. Breitenlohner and D. Z. Freedman. "Stability in gauged extended supergravity". *Annals Phys.* 144 (1982), 249.

[96] L. Mezincescu and P. K. Townsend. "Stability at a local maximum in higher dimensional Anti-de-Sitter space and applications to supergravity". *Annals Phys.* 160 (1985), 406.

[97] S. I. Finazzo, R. Critelli, R. Rougemont, and J. Noronha. "Momentum transport in strongly coupled anisotropic plasmas in the presence of strong magnetic fields". *Phys. Rev.* D94 (2016), 054020.

[98] S. Borsanyi, Z. Fodor, S. D. Katz, S. Krieg, et al. "Fluctuations of conserved charges at finite temperature from lattice QCD". *JHEP* 01 (2012), 138.

[99] I. Portillo. "Locating the QCD critical point using holographic black holes". *Proceedings, Workshop for Young Scientists on the Physics of Ultrarelativistic Nucleus-Nucleus Collisions, (HQ 2018)*. *Proceedings* 10, (2019), 40.

[100] I. Portillo. "Susceptibilities from a black hole engineered EoS with a critical point". *Proceedings, Hot Quarks 2016: Workshop for Young Scientists on the Physics of Ultrarelativistic Nucleus-Nucleus Collisions (HQ2016)*. *J. Phys. Conf. Ser.* 832, (2017), 012041.

[101] I. Portillo. "Baryon susceptibilities from a holographic equation of state". *Proceedings, 26th International Conference on Ultra-relativistic Nucleus-Nucleus Collisions (QM 2017)*. *Nucl. Phys.* A967, (2017), 916–919.

[102] I. Portillo. "QCD Critical point from a black hole engineered EoS". *Proceedings, 5th FAIR NExt generation ScientistS (FAIRNESS 2017)*. *J. Phys. Conf. Ser.* 1024, (2018), 012015.

[103] I. Portillo. "QCD phase diagram with a critical point from holographic black holes". In Preparation as a contribution for the workshop: The Critical Point and Onset of Deconfinement Conference 2018 (CPOD 2018). (2019).

[104] S. Borsanyi, G. Endrodi, Z. Fodor, S. D. Katz, et al. "QCD equation of state at nonzero chemical potential: continuum results with physical quark masses at order μ^2". *JHEP* 08 (2012), 053.

[105] F. Karsch. "Lattice results on QCD at high temperature and non-zero baryon number density". *Proceedings, Heavy-ion collisions from the Coulomb barrier to the quark-gluon plasma*. *Prog. Part. Nucl. Phys.* 62, (2009), 503–511.

[106] P. Braun-Munzinger and J. Stachel. "The quest for the quark-gluon plasma". *Nature* 448 (2007), 302–309.

[107] A. Andronic, P. Braun-Munzinger, and J. Stachel. "Thermal hadron production in relativistic nuclear collisions: The Hadron mass spectrum, the horn, and the QCD phase transition". *Phys. Lett.* B673 (2009), 142–145.

[108] J. Cleymans, H. Oeschler, K. Redlich, and S. Wheaton. "Comparison of chemical freeze-out criteria in heavy-ion collisions". *Phys. Rev.* C73 (2006), 034905.

[109] F. Karsch and K. Redlich. "Probing freeze-out conditions in heavy ion collisions with moments of charge fluctuations". *Phys. Lett.* B695 (2011), 136–142.

[110] S. Gupta, X. Luo, B. Mohanty, H. G. Ritter, et al. "Scale for the phase diagram of Quantum Chromodynamics". *Science* 332 (2011), 1525–1528.

[111] C. S. Fischer, J. Luecker, and C. A. Welzbacher. "Phase structure of three and four flavor QCD". *Phys. Rev.* D90 (2014), 034022.

[112] J. Cleymans, B. Kampfer, M. Kaneta, S. Wheaton, et al. "Centrality dependence of thermal parameters deduced from hadron multiplicities in Au + Au collisions at $\sqrt{s_{NN}}$ = 130-GeV". *Phys. Rev.* C71 (2005), 054901.

[113] F. Becattini, J. Manninen, and M. Gazdzicki. "Energy and system size dependence of chemical freeze-out in relativistic nuclear collisions". *Phys. Rev.* C73 (2006), 044905.

[114] F. Becattini, M. Bleicher, T. Kollegger, T. Schuster, et al. "Hadron Formation in Relativistic Nuclear Collisions and the QCD Phase Diagram". *Phys. Rev. Lett.* 111 (2013), 082302.

[115] J. Stachel, A. Andronic, P. Braun-Munzinger, and K. Redlich. "Confronting LHC data with the statistical hadronization model". *Proceedings, 14th International Conference on Strangeness in Quark Matter (SQM 2013)*. *J. Phys. Conf. Ser.* 509, (2014), 012019.

[116] A. Andronic. "An overview of the experimental study of quark-gluon matter in high-energy nucleus-nucleus collisions". *Proceedings, 26th International Symposium on Lepton Photon Interactions at High Energy (LP13)*. *Int. J. Mod. Phys.* A29, (2014), 1430047.

[117] E. S. Fraga, L. F. Palhares, and P. Sorensen. "Finite-size scaling as a tool in the search for the QCD critical point in heavy ion data". *Phys. Rev.* C84 (2011), 011903.

[118] G. Agakishiev, O. Arnold, A. Balanda, D. Belver, et al. "Statistical model analysis of hadron yields in proton-nucleus and heavy-ion collisions at SIS 18 energiesStatistical hadronization model analysis of hadron yields in p + Nb and Ar + KCl at SIS18 energies". *Eur. Phys. J.* A52 (2016), 178.

[119] A. Bazavov, H. T. Ding, P. Hegde, O. Kaczmarek, et al. "Freeze-out Conditions in Heavy Ion Collisions from QCD Thermodynamics". *Phys. Rev. Lett.* 109 (2012), 192302.

[120] S. Borsanyi, Z. Fodor, S. D. Katz, S. Krieg, et al. "Freeze-out parameters: lattice meets experiment". *Phys. Rev. Lett.* 111 (2013), 062005.

[121] J. E. Bernhard, J. S. Moreland, S. A. Bass, J. Liu, et al. "Applying Bayesian parameter estimation to relativistic heavy-ion collisions: simultaneous characterization of the initial state and quark-gluon plasma medium". *Phys. Rev.* C94 (2016), 024907.

[122] F. Karsch. "Recent lattice results on finite temperature and density QCD. Part I." *Proceedings, 4th International Workshop on Critical point and onset of deconfinement (CPOD07)*. *PoS* CPOD07, (2007), 026.